



Calhoun: The NPS Institutional Archive
DSpace Repository

Theses and Dissertations

1. Thesis and Dissertation Collection, all items

2010-03

Fine-scale variability in temperature, salinity,
and pH in the upper-ocean and the effects on
acoustic transmission loss in the Western
Arctic Ocean

Col, Stephen M.D.

Monterey, California. Naval Postgraduate School

<http://hdl.handle.net/10945/5385>

This publication is a work of the U.S. Government as defined in Title 17, United States Code, Section 101. Copyright protection is not available for this work in the United States.

Downloaded from NPS Archive: Calhoun



Calhoun is the Naval Postgraduate School's public access digital repository for research materials and institutional publications created by the NPS community. Calhoun is named for Professor of Mathematics Guy K. Calhoun, NPS's first appointed -- and published -- scholarly author.

Dudley Knox Library / Naval Postgraduate School
411 Dyer Road / 1 University Circle
Monterey, California USA 93943

<http://www.nps.edu/library>



NAVAL POSTGRADUATE SCHOOL

MONTEREY, CALIFORNIA

THESIS

**FINE-SCALE VARIABILITY IN TEMPERATURE,
SALINITY, AND pH IN THE UPPER-OCEAN AND THE
EFFECTS ON ACOUSTIC TRANSMISSION LOSS IN THE
WESTERN ARCTIC OCEAN**

by

Stephen M. D. Col

March 2010

Thesis Advisor:

Co-Advisor:

Tim Stanton

Daphne Kapolka

Approved for public release; distribution is unlimited

THIS PAGE INTENTIONALLY LEFT BLANK

REPORT DOCUMENTATION PAGE			<i>Form Approved OMB No. 0704-0188</i>	
Public reporting burden for this collection of information is estimated to average 1 hour per response, including the time for reviewing instruction, searching existing data sources, gathering and maintaining the data needed, and completing and reviewing the collection of information. Send comments regarding this burden estimate or any other aspect of this collection of information, including suggestions for reducing this burden, to Washington headquarters Services, Directorate for Information Operations and Reports, 1215 Jefferson Davis Highway, Suite 1204, Arlington, VA 22202-4302, and to the Office of Management and Budget, Paperwork Reduction Project (0704-0188) Washington DC 20503.				
1. AGENCY USE ONLY (Leave blank)		2. REPORT DATE March 2010	3. REPORT TYPE AND DATES COVERED Master's Thesis	
4. TITLE AND SUBTITLE Fine-Scale Variability in Temperature, Salinity, and pH in the Upper-Ocean and the Effects on Acoustic Transmission Loss in the Western Arctic Ocean.			5. FUNDING NUMBERS	
6. AUTHOR(S) Stephen M. D. Col				
7. PERFORMING ORGANIZATION NAME(S) AND ADDRESS(ES) Naval Postgraduate School Monterey, CA 93943-5000			8. PERFORMING ORGANIZATION REPORT NUMBER	
9. SPONSORING /MONITORING AGENCY NAME(S) AND ADDRESS(ES) N/A			10. SPONSORING/MONITORING AGENCY REPORT NUMBER	
11. SUPPLEMENTARY NOTES The views expressed in this thesis are those of the author and do not reflect the official policy or position of the Department of Defense or the U.S. Government.				
12a. DISTRIBUTION / AVAILABILITY STATEMENT Approved for public release; distribution is unlimited			12b. DISTRIBUTION CODE	
13. ABSTRACT (maximum 200 words) <p>Acoustic propagation in the ocean is dependent on the sound speed profile, which is a function of temperature, salinity, and pressure. In the upper ocean, these variables can change quickly as a result of fronts, internal waves, diurnal heating and other mechanisms. Transmission loss (TL) is a function of geometrical spreading, absorption, and scattering. Absorption is a function of temperature, salinity, pressure, and pH. pH variability is typically omitted from TL calculations. This thesis studied the effects of variability in the vertical structure of temperature, salinity and pH on acoustic TL in the Arctic Ocean. These parameters were measured in the Beaufort Sea in March 2009 during ICEX2009 over a period of 15 days.</p> <p>Frequencies considered in this study were 100Hz, 1kHz, and 10kHz. This range of frequencies brackets the boric acid relaxation frequency and is of interest to the U.S. Navy for anti-submarine warfare. Expected absorption losses were estimated by integrating the loss over individual ray paths. Calculations were performed with constant pH as well as by using the measured depth dependent pH. The resulting difference in total absorption losses computed with constant versus variable pH was less than 2dB over a 50km distance. The error in transmission loss calculations due to ignoring pH variability is expected to be very small compared to the uncertainties due to ice scatter-absorption. Therefore, routine measurements of the depth dependent pH levels are not recommended for the purpose of transmission loss calculations under Arctic ice cover.</p>				
14. SUBJECT TERMS Acoustic Propagation, Transmission Loss, Arctic Ocean, Temperature Salinity pH Variability			15. NUMBER OF PAGES 107	
			16. PRICE CODE	
17. SECURITY CLASSIFICATION OF REPORT Unclassified	18. SECURITY CLASSIFICATION OF THIS PAGE Unclassified	19. SECURITY CLASSIFICATION OF ABSTRACT Unclassified	20. LIMITATION OF ABSTRACT UU	

THIS PAGE INTENTIONALLY LEFT BLANK

Approved for public release; distribution is unlimited

**FINE-SCALE VARIABILITY IN TEMPERATURE, SALINITY, AND pH IN THE
UPPER-OCEAN AND THE EFFECTS ON ACOUSTIC TRANSMISSION LOSS
IN THE WESTERN ARCTIC OCEAN**

Stephen M. D. Col
Lieutenant, United States Navy
B.S., University of Nevada, Las Vegas, 2003

Submitted in partial fulfillment of the
requirements for the degree of

MASTER OF SCIENCE IN ENGINEERING ACOUSTICS

from the

**NAVAL POSTGRADUATE SCHOOL
March 2010**

Author: Stephen Col

Approved by: Tim Stanton
Thesis Advisor

Daphne Kapolka
Co-Advisor

Daphne Kapolka
Chair, Engineering Acoustics Academic Committee

THIS PAGE INTENTIONALLY LEFT BLANK

ABSTRACT

Acoustic propagation in the ocean is dependent on the sound speed profile, which is a function of temperature, salinity, and pressure. In the upper ocean, these variables can change quickly as a result of fronts, internal waves, diurnal heating and other mechanisms. Transmission loss (TL) is a function of geometrical spreading, absorption, and scattering. Absorption is a function of temperature, salinity, pressure, and pH. pH variability is typically omitted from TL calculations. This thesis studied the effects of variability in the vertical structure of temperature, salinity and pH on acoustic TL in the Arctic Ocean. These parameters were measured in the Beaufort Sea in March 2009 during ICEX2009 over a period of 15 days.

Frequencies considered in this study were 100Hz, 1kHz, and 10kHz. This range of frequencies brackets the boric acid relaxation frequency and is of interest to the U.S. Navy for anti-submarine warfare. Expected absorption losses were estimated by integrating the loss over individual ray paths. Calculations were performed with constant pH as well as by using the measured depth dependent pH. The resulting difference in total absorption losses computed with constant versus variable pH was less than 2dB over a 50km distance. The error in transmission loss calculations due to ignoring pH variability is expected to be very small compared to the uncertainties due to ice scatter-absorption. Therefore, routine measurements of the depth dependent pH levels are not recommended for the purpose of transmission loss calculations under Arctic ice cover.

THIS PAGE INTENTIONALLY LEFT BLANK

TABLE OF CONTENTS

I.	INTRODUCTION.....	1
A.	MOTIVATION	1
B.	BACKGROUND AND RELATED WORKS.....	1
1.	Sound Speed Profile.....	4
2.	Transmission Loss.....	5
C.	APLIS 2009.....	5
D.	ORGANIZATION OF THESIS	6
II.	BACKGROUND	7
A.	THE ARCTIC	7
1.	Sea Ice	7
2.	Sea Ice-Albedo Feedback	12
3.	Air-Ocean Interactions.....	13
4.	Ocean Acidification.....	14
III.	THEORY	17
A.	ACOUSTIC TRANSMISSION LOSS IN THE OCEAN	17
1.	Absorption	17
a.	<i>Pure Water</i>	18
b.	<i>Magnesium Sulfate</i>	18
c.	<i>Boric Acid</i>	19
2.	Geometrical Spreading	19
3.	Bottom Loss	20
4.	Surface Loss.....	20
a.	<i>Sea Surface Effects</i>	20
b.	<i>Ice Effects</i>	21
B.	SOUND SPEED PROFILE	22
IV.	EXPERIMENTAL SET UP AND DATA COLLECTION.....	25
A.	EQUIPMENT	25
1.	Seabird SBE19plus V2.....	25
B.	DATA COLLECTION	26
1.	Work Area Setup	26
2.	Equilibration	26
3.	Time Series	26
4.	Daily Casts	27
5.	Radial Survey	27
C.	DATA UPLOAD/CONVERSION	27
D.	EQUIPMENT MAINTENANCE	28
E.	GPS LOGGING	28
V.	ANALYTIC METHOD AND DATA ANALYSIS.....	29
A.	DATA PROCESSING	29
1.	Profile Isolation	29

2.	Binning	29
3.	De-spiking Measurements	29
4.	Temperature Structure	30
5.	Salinity Calculation.....	31
6.	pH Structure.....	32
B.	DATA FOR DEEP WATER.....	39
C.	SOUND SPEED PROFILES.....	43
1.	Sound Speed Calculation.....	43
2.	Sound Speed Profile Features	46
D.	RAY MODEL.....	47
1.	Inputs	47
a.	<i>Temperature and Salinity</i>	47
b.	<i>pH</i>	47
2.	Sound Speed Profile Smoothing	48
3.	Ray Traces	48
E.	TRANSMISSION LOSS	52
1.	Spherical Spreading.....	53
2.	Absorption in Seawater	54
3.	Ice Scatter-Absorption Effects.....	63
a.	<i>SCICEX Data Set and Diachok Loss Model</i>	63
b.	<i>TL Results with Ice Scatter-Absorption Included</i>	67
4.	Relative Magnitude of Effects.....	72
F.	RADIAL SURVEY	74
1.	Data	74
2.	Range Dependence.....	74
VI.	CONCLUSIONS AND RECOMMENDATIONS.....	77
A.	SUMMARY OF RESULTS	77
1.	No Ice Effects / Perfectly Reflecting Surface.....	77
2.	Ice Scatter-Absorption Included	78
B.	RECOMMENDATIONS.....	78
1.	pH and SSP	78
2.	Ice Scatter-Absorption.....	80
3.	Investigate Submarine Detection Ranges	80
4.	Model Validation.....	81
	BIBLIOGRAPHY	83
	INITIAL DISTRIBUTION LIST	89

LIST OF FIGURES

Figure 1.	Absorption vs. Frequency (10Hz – 1MHz). T and S (and pH = 7.88) are the means from the Applied Physics Laboratory Ice Station during Ice Exercise 2009 at 10m depth. Absorption values due to reduction of pH 0.3 to 0.5 are shown.	4
Figure 2.	Aerial view of a lead (left) that is freezing over, viewed from the air. Close-up view of a ridge sail (right). Beaufort Sea. March 2009.	8
Figure 3.	The solid light blue line shows 2009/2010 daily sea ice extent up to March 4, 2010. The dashed green indicates 2006/2007 (the record low for the month of January); and the solid gray indicates the average extent from 1979 to 2000. The gray area around the average line shows the two standard deviation range of the data. The red ellipse highlights the much lower sea ice extent in the fall compared to the mean. (National Snow and Ice Data Center 2010)	9
Figure 4.	Arctic September sea ice extent ($\times 10^6 \text{ km}^2$) from observations (thick red line) and 18 IPCC AR4 climate models together with the multi-model ensemble mean (solid black line) and standard deviation (dotted black line). Models with more than one ensemble member are indicated with an asterisk. Inset shows 9-year running means (Stroeve et al. 2007). Note that this figure represents data for September ice extent, two months before what is shown in Figure 3.	10
Figure 5.	The graph above shows daily sea ice extent for summer-fall. The solid light blue line indicates 2009; the dashed green indicates 2007 (the record low); and the solid gray indicates the average extent from 1979 to 2000. The gray area around the average line shows the two standard deviation range of the data. (National Snow and Ice Data Center 2010)	11
Figure 6.	Arctic March sea ice extent ($\times 10^6 \text{ km}^2$) from observations (thick red line) and 18 IPCC AR4 climate models together with the multi-model ensemble mean (solid black line) and standard deviation (dotted black line). Models with more than one ensemble member are indicated with an asterisk. Inset shows 9-year running means (Stroeve et al. 2007).	12
Figure 7.	Graphical representation of data in Table 1. The frequency for the three sets of lines are 10kHz for the top set, 1kHz for the middle set, and 100Hz for the bottom set. In each frequency set, the green lines represent the measured pH values at APLIS 2009. The blue lines represent pH lowered by 0.3 pH. The red lines represent pH lowered by 0.5 pH.	16
Figure 8.	Comparison of sound speed profile equations. The plot on the left uses the listed algorithms for determining sound speed from all the profiles of T and S at APLIS 2009. The plot on the right uses the same data and is zoomed into the region where most data acquisition occurred. Note that profiles were conducted to a maximum depth of 518m. The variability due to algorithm choice in the upper ocean is dominated by the consequences of T and S variability.	24

Figure 9.	Sea-Bird Electronics SBE 19plus V2 with SBE18 pH sensor. As deployed at APLIS 2009.....	25
Figure 10.	Thermocline and halocline depths versus time, in Ordinal days. The green and black lines represent the data after being filtered to indicate thermocline and halocline depth trends.	31
Figure 11.	Temperature and salinity measured at APLIS. Radial survey data is excluded.	32
Figure 12.	pH as indicated. Note that the shape of the structure is very similar for the profiles.	33
Figure 13.	Measured pH at 10 meters vs. time, during the time series at APLIS. This plot demonstrates the effect of equilibrating over hours instead of seconds to minutes.	34
Figure 14.	The red curve is the mean of two profiles from Leif Anderson's Fall 2005 Beaufort Cruise. The light green is the mean of the collapsed APLIS data. ...	36
Figure 15.	Full water column pH profiles. Shallow data is from APLIS 2009, aligned with deep data from Anderson 2005, using the Seawater pH Scale.	37
Figure 16.	Free scale pH profiles used for absorption calculations.	39
Figure 17.	(L) Measured temperature profiles (four to 518m, 198 to 233m average depth) and (R) measured temperature profile extended to 518m with the mean of the deep profiles.	40
Figure 18.	(L) Measured salinity and (R) measured salinity extended with the mean of the deep profiles. These plots are nearly identical, highlighting the low variability of salinity below the upper ocean. The transition regions where the shallow profiles are extended are visible when comparing the areas between 200m and 250m.	41
Figure 19.	(L) Temperature profiles from WOA2001 near APLIS, ITP 11, ITP 21, and the mean of the deep profiles obtained at APLIS. (R) Salinity profiles from the same sources.	42
Figure 20.	Full water column T and S profiles used to calculating sound speed and absorption.	43
Figure 21.	CML sound speed profile (SSP) in black compared to SSPs calculated by three other equation sets. The subplot on the left shows the SSPs calculated from the mean T and S. The subplot on the right shows all of the SSPs, for all of the equation sets, generated from all the T and S profiles.	45
Figure 22.	CML sound speed profile (SSP) in black compared to SSPs calculated by three other equation sets. The subplot on the left shows the SSPs calculated from the mean T and S. The subplot on the right shows the all of the SSPs, for all of the equation sets, generated from all the T and S profiles zoomed in to the upper 250m.	46
Figure 23.	Sound speed profile that was used for the following ray traces.	49
Figure 24.	Set of ray traces for APLIS profile #3, source depth of 150m, and frequency of 1kHz. Note the density of rays in the sound channel.	49

Figure 25.	Set of ray traces for APLIS profile #3, source depth of 100m, and frequency of 1kHz. Note that there are fewer rays trapped in the sound channel, and a higher density of rays interacting with the surface.	50
Figure 26.	Set of ray traces for APLIS profile #3, source depth of 50m, and frequency of 1kHz. Note that there are no rays confined to the sound channel and the large number of surface interactions.	51
Figure 27.	Number of reflections from the ice surface, as a function of frequency for the three source depths. Note how the negative launch angles tend to have one less reflection than the corresponding positive launch angles.	52
Figure 28.	For one profile, plots of path length (blue) and spherical TL (green) for source depth of 50m (left), 100m (center), and 150m (right).	54
Figure 29.	Absorption Profiles. Color curves include measured parameters. Black curves consider pH=7.98, a single value for all depths.	55
Figure 30.	Transmission loss vs. Launch Angle. Source depth = 50m.	57
Figure 31.	Transmission loss vs. Launch Angle. Source depth = 100m.	58
Figure 32.	Transmission loss vs. Launch Angle. Source depth = 150m.	59
Figure 33.	Histograms illustrating the spread of TL, for a perfectly reflecting surface, with Source Depth = 50m. These correspond to the plots of Figure 30.	61
Figure 34.	Histograms illustrating the spread of TL, for a perfectly reflecting surface, with Source Depth = 100m. These correspond to the plots of Figure 31.	62
Figure 35.	Histograms illustrating the spread of TL, for a perfectly reflecting surface, with Source Depth = 150m. These correspond to the plots of Figure 32.	62
Figure 36.	Spatial Frequency vs. Keel Draft for SCICEX 1988 data. This figure shows that the spatial frequency is higher for smaller keels, and lower for larger keels.	65
Figure 37.	Comparison of Reflectivity vs. Angle for Diachok's $N=9.5 \text{ km}^{-1}$ and $d=4.3\text{m}$, and the mean ice draft data from SCICEX, $N=11.8 \text{ km}^{-1}$ and $d=8.5\text{m}$	66
Figure 38.	Observations of angles for rays when incident upon the ice. For the top plot, Source Depth = 50m. For the center plot, Source Depth = 100m. For the bottom plot, Source Depth = 150m. Note that the scale on the left is different for the 50m case because of the much higher number of surface reflections.	67
Figure 39.	Transmission Loss vs. Launch Angle with ice scatter-absorption effects included. Source Depth = 50m. The blue curves which are barely visible, contain the same data as in Figure 30. Note the scale on the vertical axis, which shows the huge increase in TL in dB due to ice effects.	68
Figure 40.	Transmission Loss vs. Launch Angle with ice scatter-absorption effects included. Source Depth = 100m. Note the scale on the vertical axis, compared to the previous figure, and the effects of rays getting confined to the sound channel.	69
Figure 41.	Transmission Loss vs. Launch Angle with ice scatter-absorption effects included. Source Depth = 150m.	70

Figure 42.	Histograms illustrating the spread of TL when ice scatter-absorption is included. Source Depth = 50m. These histograms correspond to the plots in Figure 39.	71
Figure 43.	Histograms illustrating the spread of TL when ice scatter-absorption is included. Source Depth = 100m. These histograms correspond to the plots in Figure 40.	71
Figure 44.	Histograms illustrating the spread of TL when ice scatter-absorption is included. Source Depth = 150m. These histograms correspond to the plots in Figure 41.	72
Figure 45.	Sound speed profiles for the radial survey. The light green curve shows the mean of the SSPs from 124 profiles from the 36-hour time series. The black dashed curves show ± 1 standard deviation from the mean. This figure shows that the variability in sound speed profile in a few hours over 47km is greater than the variability in the SSP over 36 hours and drifting 0.1km.	75

LIST OF TABLES

Table 1.	Absorption Coefficients (dB/km) calculated using the Francois-Garrison equation. Case 1 uses the values in Table 2. Case 2 subtracts 0.3 pH from the values in Table 2. Case 3 subtracts 0.5 pH from the values in Table 2. These three cases are demonstrated graphically in Figure 7.....	15
Table 2.	Mean values of T, S, and pH at the given depths. From APLIS 2009.....	15
Table 3.	Temperature and salinity minimum, maximum, mean, and standard deviation for the upper 10m. Also shown are the statistics for the thermocline depth and the halocline depth.	30
Table 4.	Absorption Profile points of interest. Note that the 100Hz and 1kHz curves have an absorption maximum above the sound channel and a local minimum in the channel, while the 10kHz curve has a maximum absorption coefficient below the channel and a local minimum near the surface.	56

THIS PAGE INTENTIONALLY LEFT BLANK

ACKNOWLEDGMENTS

Thank you to my beautiful wife, Jules, for all your support and encouragement from the start, and every step of the way to the finish here. I look forward to more and greater adventures with you and our family.

Thank you to Professor Tim Stanton for the opportunity, instruction, wisdom, and experience that encompassed the research, fieldwork, and data analysis.

Thank you to Professor Daphne Kapolka for your guidance, questioning attitude, and undersea warfare focus.

Thank you to Professor Bill Shaw for all your help getting ready for the Arctic and with the data processing back at NPS.

Thank you to Professor John Colosi and LCDR Ben Jones for your help with the ray model.

Thank you to LT Russ Ingersoll for many a chess game while waiting for authorization to conduct CTD operations.

Thank you to RADM Ray Jones and RADM Rick Williams for providing the opportunity and materiel support for the ICEx trip.

Thank you to RADM Jerry Ellis for your professional experience and guidance as a submariner.

Thank you to the incredible teams from the Arctic Submarine Laboratory and the Applied Physics Laboratory-University of Washington. I hope to one day join you again, perhaps from the submarine side of the exercise.

The buoy deployment was funded under National Science Foundation, Office of Polar Programs “International Polar Year Observation Systems,” grant number ARC-0632041.

The CTD and pH measurement project at the ice camp was funded under Office of Naval Research; grant number N0001409WR20069.

THIS PAGE INTENTIONALLY LEFT BLANK

I. INTRODUCTION

A. MOTIVATION

The Arctic Ocean is an environment that is acoustically difficult to model. Combined effects of growing and shrinking ice, areas of open-ocean, and scarcity of ocean profile data yield significant errors in acoustic modeling. This research studies fine-scale variability in temperature, salinity, and pH in the upper ocean, and their effects on acoustic transmission loss in the Western Arctic Ocean. The volume of sea ice is declining faster than model predictions (Stroeve et al. 2007) and as there are more areas permanently or seasonally free of ice, there will be increased commercial and military operations in the Arctic (Beluga Group and Task Force Climate Change 2009). Enhanced understanding of the operational environment is important at the tactical and the strategic levels. With regard to submarine operations, application of improved environmental sensors and models could lead to increased performance of undersea weapons and higher accuracy in submarine detection ranges. Since the transmission and detection of acoustic energy in the ocean is the primary method for target prosecution and safe under-ice navigation, the United States Navy is keenly interested in effective and efficient use of sonar.

Considering that the sound speed profile changes as a result of tidal, daily, and seasonal effects, as well as longer-scale climatological changes, care must be given when selecting a sound speed profile to use in predictive acoustic models. The primary goal of this work is to investigate the short-term effects of upper ocean variability, especially the pH, on the transmission loss due to absorption between current profiles and annual means.

B. BACKGROUND AND RELATED WORKS

The undersea environment provides many challenges to navigation, communication, and combat. Ocean water quickly attenuates electromagnetic radiation, including radar and visible light. Acoustic energy, however, can propagate for very long ranges (Kinsler et al. 2000). This energy can be passively received and processed, and in

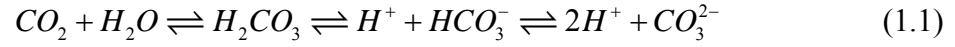
the realm of undersea warfare can be used to detect, track, and classify vessels. Sound can also be used actively and transmitted into the water for communication, to localize an enemy vessel, or it can be reflected from the bottom (or in the Arctic from the ice canopy) to allow for safe submarine navigation. If a given environment and the factors affecting how sound travels in that environment are known, detection ranges may be more accurately predicted.

The Arctic Ocean is a unique environment for submarine operations. A submarine must avoid time-varying physical obstructions like icebergs and ice keels and deal with an acoustically noisy environment due to cracking and shifting ice. It cannot employ radio communications, and it is deprived of the classic submarine safety net of being able to surface and ventilate in an emergency.

As the Arctic sea ice extent and volume decline (Stroeve et al. 2007), the level of interest in and access to the region increases. In September 2009, two commercial ships completed the first voyage from the Pacific Ocean to Europe via the Northeast Passage (or the Northern Sea Route). The voyage from South Korea to Rotterdam, Netherlands was about 4,000 km shorter than the conventional route through the Indian Ocean, Suez Canal, and the Mediterranean. There is increasing interest in extracting the vast untapped natural resources in the arctic seabed and, consequently, effort is going into resolving conflicting claims over Arctic territory. As the amount of traffic and commercial activity in the region increases, there will be an increased military presence as well.

Declining sea ice volume (Rothrock et al. 1999 and Stroeve et al. 2007) provides additional feedback effects for the Arctic ocean-air interactions. Thinner ice forms leads (breaks apart) more easily. Reduced ice cover allows more summertime solar radiation to be absorbed by the water, thus warming the ocean mixed layer, and making it more difficult for ice to refreeze in the following fall season. The resulting increased area of open water significantly increases air-ocean interactions. As atmospheric carbon dioxide (CO₂) levels rise (Bindoff et al. 2007 and Denman et al. 2007), there is a greater CO₂ transfer into the ocean (Bates et al. 2006 and Bindoff et al. 2007). As shown in equation(1.1), when CO₂ dissolves in water, it forms carbonic acid, increasing the concentration of hydrogen ions, which lowers the pH of the ocean (Hester et al. 2008).

The arrows pointing to the left and right show that the processes in this weak acid system can occur to the left and the right, depending on relative concentrations and external stresses (e.g., temperature or pressure).



This lower pH reduces the amount of sound absorbed in the ocean (Fisher and Simmons 1977 and Francois and Garrison 1982b), as shown in Figure 1. This will be discussed further in Chapters II and III.

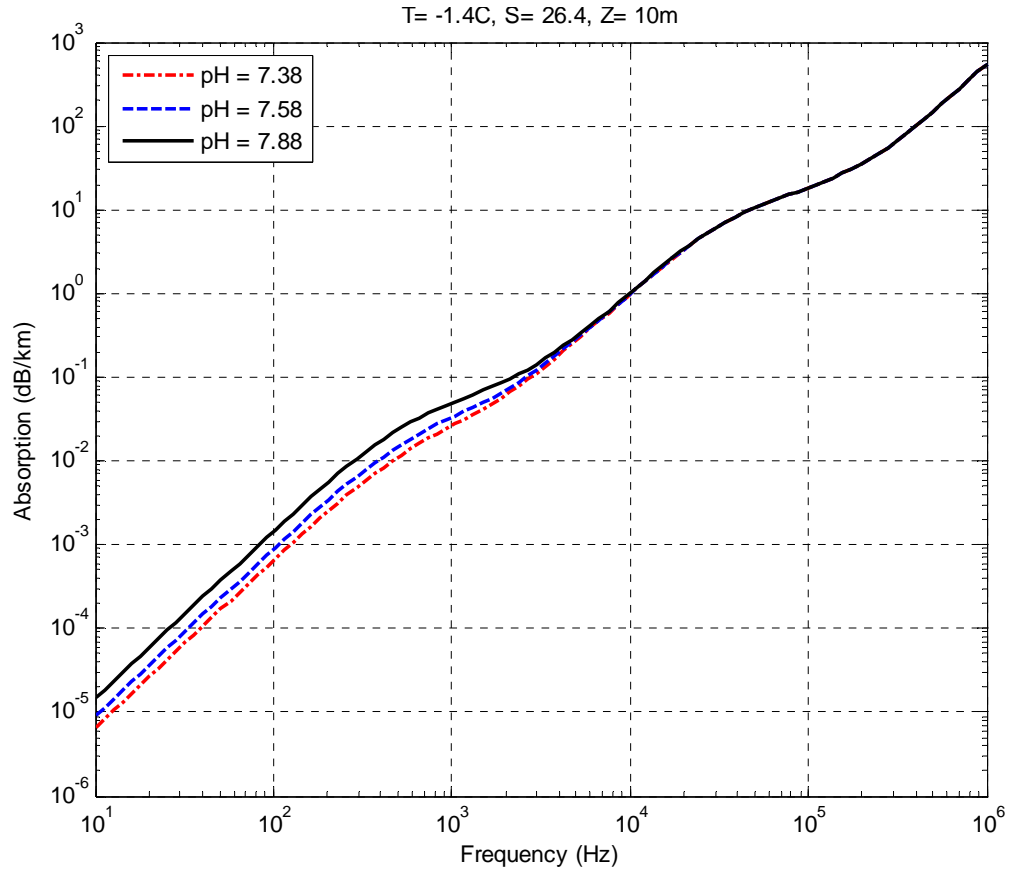


Figure 1. Absorption vs. Frequency (10Hz – 1MHz). T and S (and pH = 7.88) are the means from the Applied Physics Laboratory Ice Station during Ice Exercise 2009 at 10m depth. Absorption values due to reduction of pH 0.3 to 0.5 are shown.

1. Sound Speed Profile

The deep ocean environment is typically slowly changing with range, and so can be considered range-independent or horizontally stratified (Lurton 2002). Acoustic energy travels as a compressional wave. If the wave amplitude and the sound speed do not change significantly over distances comparable to a wavelength, then the propagation of acoustic energy can be modeled as following a ray normal to the wave front (Kinsler et al. 2000), with the ray bending toward areas of lower sound speed. The speed of sound traveling in the ocean depends on the temperature (T), salinity (S), and pressure (P). While there are several methods for calculating sound speed, the Chen-Millero equation (1977), as modified by Millero and Li (1994), is the standard for the Navy (Moskal

2010). It is referred to as CML 1.1 (for Version 1.1 of Chen-Millero-Li). Though latitude has been accounted for previously (Mackenzie 1960), an equation was recently introduced that includes the correction factor for latitude and is compact with a high level of accuracy (Leroy et al. 2008).

2. Transmission Loss

Sound transmitted in the ocean spreads geometrically, leading to lower power per unit area. In an isospeed environment without boundaries, the geometric, or spreading, loss follows an inverse square relationship with distance from the source (Lurton 2002). As a sound wave travels in the water, transmission loss also occurs from a variety of mechanisms including scattering and absorption. Absorption results in the loss of sound energy. It is attributable to several factors that include viscosity, thermal conduction, thermal and chemical relaxation, and interactions with inhomogeneities and boundaries (Kinsler et al. 2000). Scattering also results from interactions with inhomogeneities and boundaries. However, scattered sound energy is not lost, it is simply redirected. These mechanisms will be discussed in detail in Chapter III.

C. APLIS 2009

The Applied Physics Laboratory Ice Station (APLIS) was established on the ice cover in the Beaufort Sea, 350km north of Alaska in March 2009 in support of the U.S. Navy's Ice Exercise (ICEX) 2009. Personnel from the Arctic Submarine Laboratory and University of Washington's Applied Physics Laboratory (APL-UW) established an acoustic tracking range and a support camp. Experiments were performed with LT Russ Ingersoll, also a student at the Naval Postgraduate School (NPS). A working hut with a hole in the floor through the ice allowed access to the ocean. Measurements of ocean temperature (T), salinity (S), and pH were obtained with a CTD (conductivity, temperature and depth profiler) and add-on pH sensor. 202 profiles were obtained over the course of the camp. This spanned 17 days while the ice camp drifted over 100km. A 36-hour time series was conducted at the beginning of the camp with profiles obtained down to 234m every 16 minutes. On most days, six profiles were obtained to 233m, but over two days four profiles were to 518m.

In order to study spatial variability of T, S, and pH, a radial survey was conducted, supported by helicopter. The helicopter flew out from the camp following a line of bearing of 039°, and stopping every 9.4km, where a hole was augured through the ice and two profiles were obtained. As a result, six locations were sampled, including one at APLIS. After the final radial was completed, 47km to the northeast, a final set of CTD casts (essentially a 0th radial) was obtained from the working hut at APLIS. This provided a comparison of upper ocean vertical structure with the greatest spatial difference, but a small temporal difference.

Preliminary processing of the data was conducted at APLIS, for diagnostic purposes. This included retrieving the data from the CTD and generating plots of the temperature, salinity, pH, density, and sound speed profiles. Each day, the sound speed profile was provided to the APLIS Command Hut, which then relayed information to the submarines involved in the exercise.

Detailed processing and analysis was completed at NPS. During the camp, the NPS students assisted a team from the U.S. Naval Academy and deployed two meteorological (ARGOS) buoys. Toward the end of the camp, the students also deployed an Autonomous Ocean Flux Buoy in support of Professor Tim Stanton's Autonomous Ocean Turbulent Flux Buoy Program at NPS, which is supported by the National Science Foundation Office of Polar Programs.

D. ORGANIZATION OF THESIS

This thesis will introduce how sound travels in the Arctic Ocean, discussing factors influencing the sound speed profile and factors influencing the attenuation of acoustical energy. There is much interest in the Arctic waters and in the complex air-ocean interactions of the region. Chapter II will review current background research on Arctic oceanography, and the theory underlying acoustic propagation and transmission loss in the ocean will be discussed in Chapter III. Chapter IV will detail the experimental set up and data collection method. In Chapter V profiles of temperature, salinity, and pH of the Arctic Ocean measured during ICEX 2009 and their sound speed structure will be presented. Chapter VI will present conclusions from the research and recommendations for application and future study.

II. BACKGROUND

A. THE ARCTIC

The Arctic Ocean is a unique operating environment. Many regions of deep water have a sound speed profile that is downward refracting near the surface and upward refracting at deep depths, creating a thick channel where sound can be trapped and propagate long distances. In the Arctic, the sound speed profile is primarily upward refracting, and so sea ice reflections are expected to be important. During the fieldwork conducted in the Beaufort Sea in March 2009, there was a thin (100m deep) sound channel centered near 150m, which could allow extended propagation ranges.

1. Sea Ice

When seawater freezes, it becomes first-year sea ice. Icebergs are glacial ice that have broken off into the ocean and are not considered sea ice. In the Arctic Ocean, some sea ice melts during the summer, but much of it persists until the next winter, when it is considered perennial or multi-year ice. In the Southern Ocean, around Antarctica, almost all of the ice is “seasonal ice,” meaning that it melts and reforms annually (National Snow and Ice Data Center 2010). The only significant source of ice formation in the Arctic summers is the thickening of a “false-bottom”, a layer of ice beneath an under-ice melt pond (Notz et al. 2003). Several factors influence the thickness of the ice, including the temperature and salinity of the ocean mixed layer seawater, the amount of snow cover on the ice, the wind speed, and the air temperature.

Sea ice that is not “landfast” is moved in the ocean, driven primarily by wind, but also by ocean currents. While this wind forcing applies a stress to the top of the ice, the ocean exerts a drag on the underside of the ice. When diverging forces acting on an ice floe exceed the tensile strength of the ice, it fractures and an open body of water is formed, called a lead, that can range in size from centimeters to kilometers (Fricke 1993). A lead photographed from a helicopter is shown in Figure 2. Winter leads are an important source of atmosphere-ocean coupling (McPhee and Stanton 1996), as the rest of the ice cover largely prevents any other interactions.



Figure 2. Aerial view of a lead (left) that is freezing over, viewed from the air. Close-up view of a ridge sail (right). Beaufort Sea. March 2009.

If two ice floes are forced together, their interaction is dependent on several factors. Thin ice sheets may undergo ‘rafting,’ where one sheet is pushed below the other, and the thickness of the ice where this process occurs is effectively doubled (Lemke et al. 2007). Another mechanism of convergence occurs when the ice from either floe breaks up along the line where they meet. As this process continues, some blocks are forced up and some forced down, forming the sail and keel of a pressure ridge. There are several manifestations of ridges, but the ratio of sail height to keel depth ranges from 1/3 to 8 with an average of 4.0 ± 0.5 . The ratio of keel draft to ridge width averages 1/3 (Diachok 1976). Regardless of the shape and draft, they are features that a submarine wants to avoid. Navy submarines utilize upward-looking sonar to ensure safe maneuvering when transiting under the ice. The U.S. Navy’s Arctic Submarine Laboratory (ASL) has archived ice draft observations since the USS NAUTILUS (SSN 571) first transited the Arctic Ocean in 1958 (Submarine Force Museum 2009).

Using the submarine data, Rothrock determined that the mean ice draft in the Beaufort Sea was 2.1m (meters) from 1958–1976, and 1.2m during the 1990s. The mean ice draft trend for measurements from 1993, 1996, and 1997 showed a decrease of 0.14m/yr in the Beaufort Sea (Rothrock et al. 1999).

In addition to the ice thinning, the sea ice extent is also declining. Measured by satellite and adding up areas with at least 15% sea ice concentration, the sea ice extent

has decreased (9.12 ± 1.54)% per decade from 1979–2006, and it has decreased (17.91 ± 5.98)% per decade from 1995–2006 (Stroeve et al. 2007). Recent levels from the National Snow and Ice Data Center (2010) are shown in Figure 3. Model predictions and data for September are shown in Figure 4. Those for March are shown in Figure 6. March generally has the greatest ice extent and thickness, being at the end of the Arctic winter, whereas September toward the end of the Arctic summer (melt season) has the smallest annual ice extent and thickness.

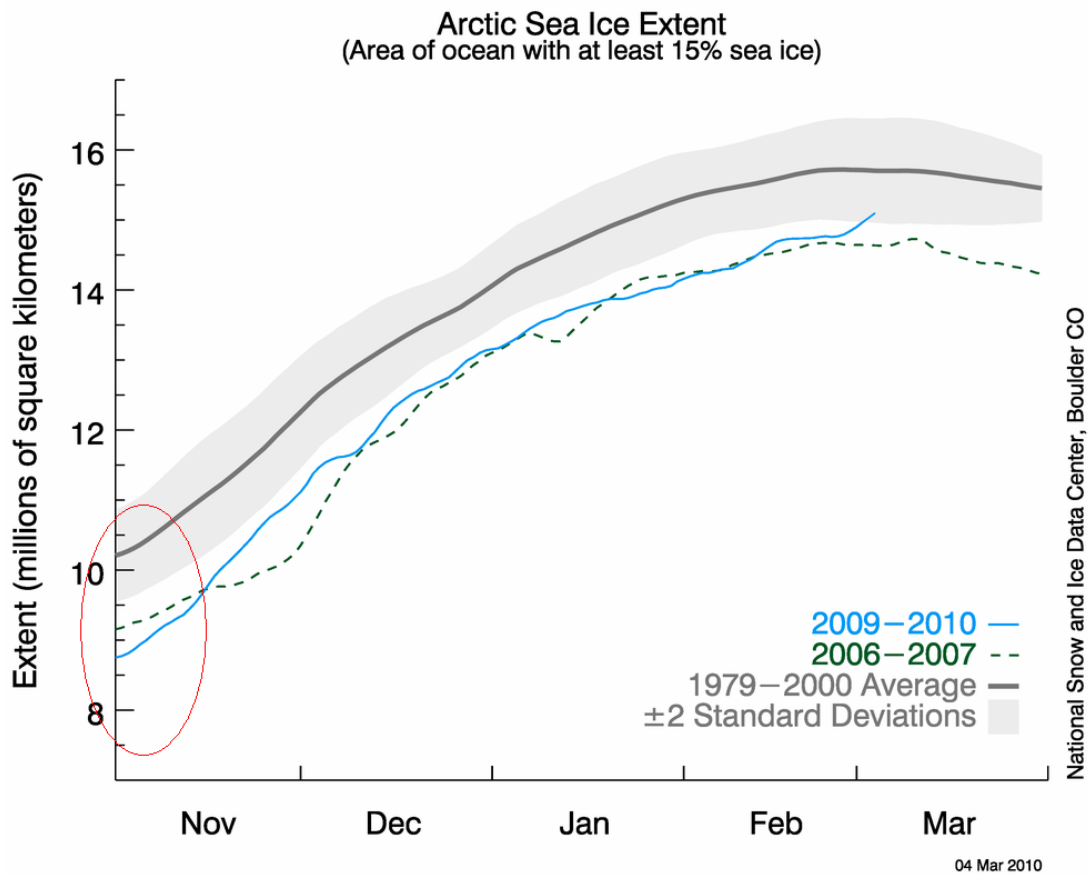


Figure 3. The solid light blue line shows 2009/2010 daily sea ice extent up to March 4, 2010. The dashed green indicates 2006/2007 (the record low for the month of January); and the solid gray indicates the average extent from 1979 to 2000. The gray area around the average line shows the two standard deviation range of the data. The red ellipse highlights the much lower sea ice extent in the fall compared to the mean. (National Snow and Ice Data Center 2010)

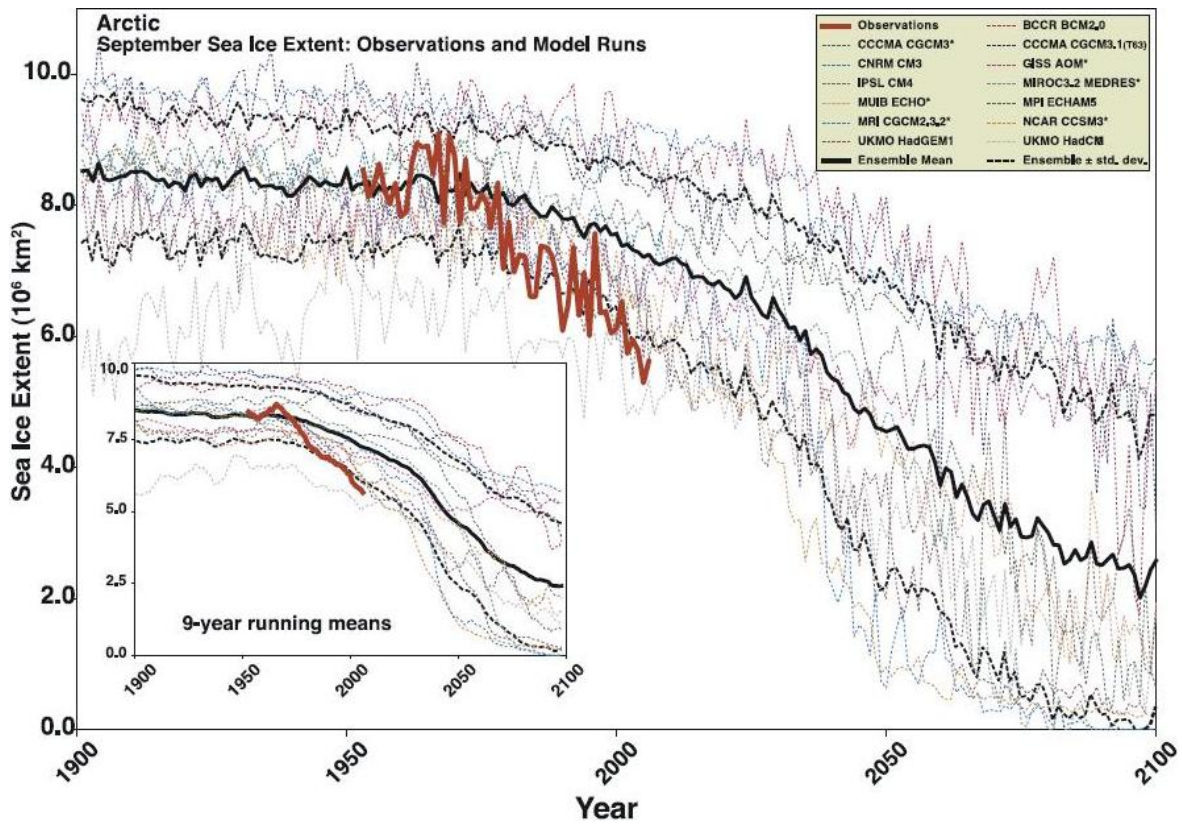


Figure 4. Arctic September sea ice extent ($\times 10^6 \text{ km}^2$) from observations (thick red line) and 18 IPCC AR4 climate models together with the multi-model ensemble mean (solid black line) and standard deviation (dotted black line). Models with more than one ensemble member are indicated with an asterisk. Inset shows 9-year running means (Stroeve et al. 2007). Note that this figure represents data for September ice extent, two months before what is shown in Figure 3.

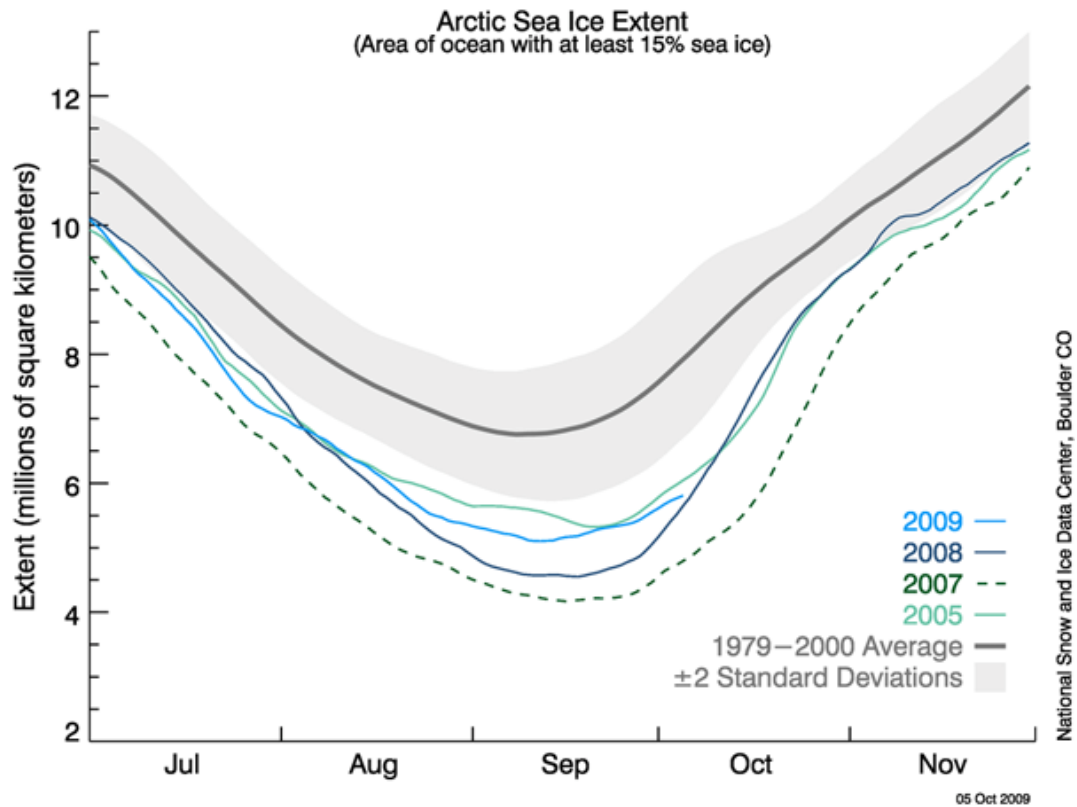


Figure 5. The graph above shows daily sea ice extent for summer-fall. The solid light blue line indicates 2009; the dashed green indicates 2007 (the record low); and the solid gray indicates the average extent from 1979 to 2000. The gray area around the average line shows the two standard deviation range of the data. (National Snow and Ice Data Center 2010)

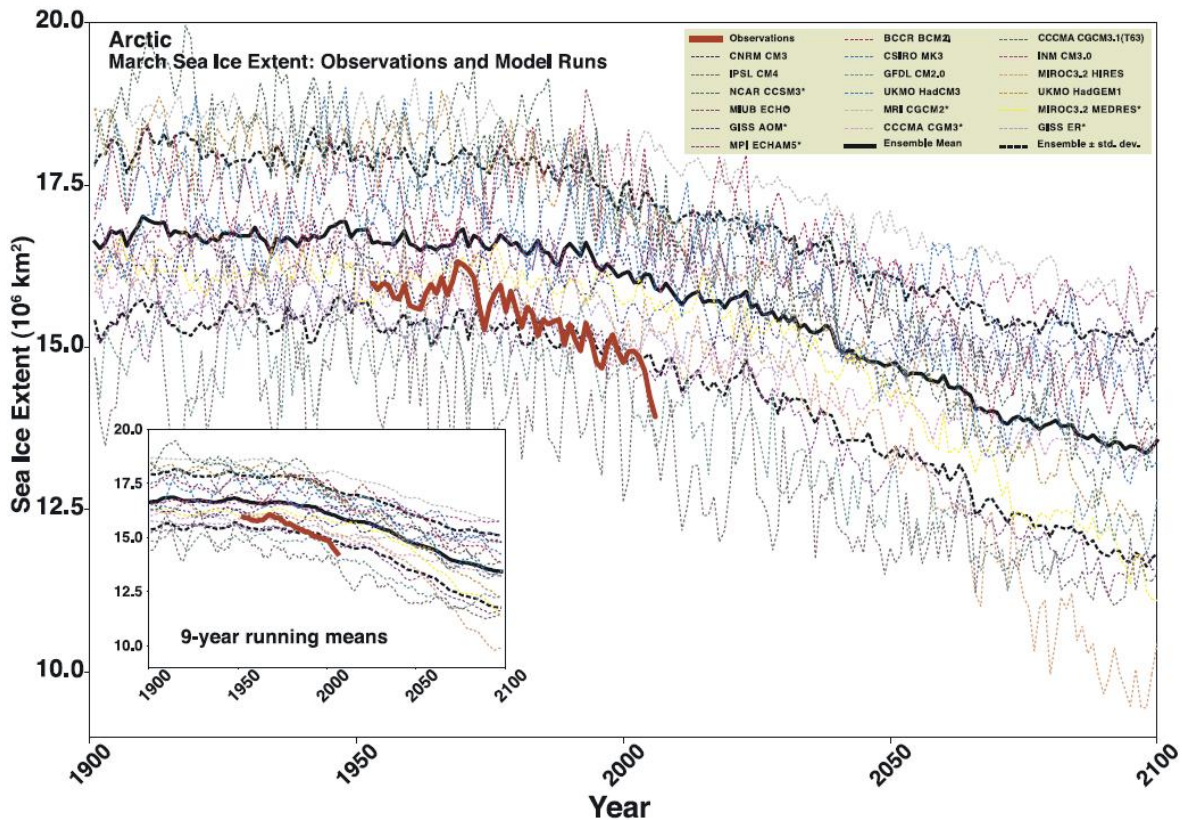


Figure 6. Arctic March sea ice extent ($\times 10^6 \text{ km}^2$) from observations (thick red line) and 18 IPCC AR4 climate models together with the multi-model ensemble mean (solid black line) and standard deviation (dotted black line). Models with more than one ensemble member are indicated with an asterisk. Inset shows 9-year running means (Stroeve et al. 2007).

2. Sea Ice-Albedo Feedback

The ocean absorbs sunlight more readily than ice does while snow reflects light better than ice or open water so consequently the measure of surface reflectivity, or albedo, is an important factor in sea ice growth and decline. The albedo is the fraction of incident solar radiation that is reflected by a surface (Hanson 1961). A good reflector has a high albedo, and vice versa. The albedo of open water, measured in the Beaufort and Chukchi Seas in summer 1958 was 0.04 ± 0.02 . Areas that were 80-90% ice covered had an albedo of 0.40 ± 0.13 (Hanson 1961). As the sea ice extent decreases, there is less ice to reflect solar radiation away from the Earth's surface, resulting in lower mean albedo. This allows more sunlight to be absorbed by the earth-atmosphere system, contributing to a temperature increase (Curry et al. 1995). This can make it more difficult to form sea

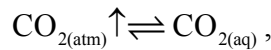
ice, and consequently lowers the regional albedo. This is a positive feedback effect, and so the converse is also true - as temperature decreases, more ice can form, increasing the area albedo, and reflecting more solar radiation.

3. Air-Ocean Interactions

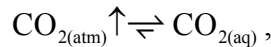
When the partial pressure of CO₂ in the ocean and the atmosphere are the same, the rate of CO₂ being taken up by the ocean equals the rate of the CO₂ coming out of solution, and the system is in equilibrium. The following equation shows atmospheric and aqueous (ocean) CO₂ at equilibrium, where there is a relatively equal exchange to the left and to the right.



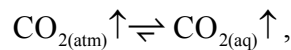
The surface waters of the Canada Basin are undersaturated with respect to CO₂ in the atmosphere, and therefore have a great capacity to take up CO₂ from the air (Semiletov et al. 2009). When the partial pressure of CO₂ ($p\text{CO}_2$) in the air increases (denoted by the up-arrow for atmospheric CO₂) and is greater than that of the water,



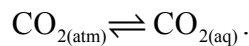
the equilibrium function stresses toward right (denoted by the longer right arrow, and the shorter left-arrow),



resulting in the water taking up and dissolving more CO₂ from the atmosphere,



and eventually, a new equilibrium condition is reached



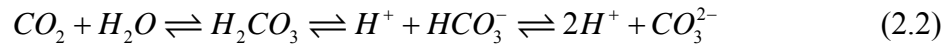
The Revelle factor describes how $p\text{CO}_2$ in the ocean changes given a change in dissolved inorganic carbon (DIC). The Revelle factor is directly proportional to the ratio of DIC to alkalinity, and is inversely proportional to the capacity for the ocean to absorb anthropogenic CO₂ in the atmosphere (Sabine et al. 2004). The waters in the western

Arctic Ocean have an unusually high capacity to absorb CO₂. This is reflected in the very low Revelle Factor (~3.5-6.5) for the surface waters of the Canada Basin, while tropical and subtropical waters have Revelle factors generally considered low (8-10), and subpolar and temperate waters have high Revelle Factors (11-14) (Bates et al. 2006). The ability for the waters of the Canada Basin to take up so much CO₂ is influenced by the high alkalinity runoff from the Mackenzie River and from sea ice melt (Bates et al. 2009).

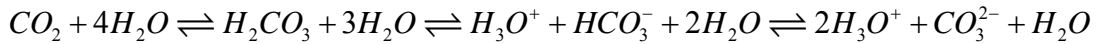
Even when there is a large ocean area covered by sea ice, there can still be an air-ocean exchange of CO₂ through leads and fractures (Bates et al. 2006 and Semiletov et al. 2004). A circulation of CO₂ can be facilitated by density differences near brine channels. The water from a brine channel has a higher salinity and density than the surrounding water. Though the residence time of surface waters in the Canada Basin is estimated to be about 15 years, these channels provide a source for CO₂ to leave the upper ocean (Bates et al. 2006) by entrainment in the sinking denser water.

4. Ocean Acidification

The equilibrium equation for carbon dioxide in water is



or



The second equation specifies that there is excess water in all stages of the equation. When CO₂ dissolves in water, it forms carbonic acid (H_2CO_3), bicarbonate (HCO_3^-), and carbonate (CO_3^{2-}), and releases hydrogen ions and hydronium (H^+ and H_3O^+), which lower the water's pH (Hester et al. 2008). This lower pH reduces the amount of sound absorbed in the ocean (Fisher and Simmons 1977 and Francois and Garrison 1982b).

In addition to increased CO₂ levels, fossil fuel burning contributes increased sulfur and nitrogen that cause ocean acidification as well (Hester et al. 2008), but the effect is small (Doney et al. 2007). In the next 50-100 years, pH is projected to decrease by pH 0.3-0.5 (Bates et al. 2009), and in the next 300 years by pH 0.7 (Caldeira and Wickett 2003). A simplified version of the full Francois-Garrison absorption equation

(Francois and Garrison 1982b) by Ainslie and McColm (1998) shows how pH factors into the absorption of sound in seawater.

$$\alpha = 0.106 \frac{f_1 f^2}{f_1^2 + f^2} e^{\frac{(pH-8)}{0.56}} + 0.52 \left(1 + \frac{T}{43}\right) \left(\frac{S}{35}\right) \frac{f_2 f^2}{f_2^2 + f^2} e^{\frac{-z}{6}} + 4.9 \times 10^{-4} f^2 e^{-\left(\frac{T}{27} + \frac{z}{17}\right)} \quad (2.3)$$

In equation (3.2), α is the absorption coefficient (dB/km), f_1 is the relaxation frequency of boric acid (0.769kHz for $T=-0.256$ °C and $S=34.67$), f_2 is the relaxation frequency for magnesium sulfate (41.372 kHz for $T=-0.256$ °C), and z is depth in km.

		Case 1			Case 2			Case 3		
	f	0.1 kHz	1 kHz	10 kHz	0.1 kHz	1 kHz	10 kHz	0.1 kHz	1 kHz	10 kHz
z(m)	1	0.00144	0.04946	1.02269	0.00088	0.03314	0.99994	0.00065	0.02624	0.99032
	30	0.00145	0.05032	1.02746	0.00089	0.03365	1.00410	0.00065	0.02660	0.99423
	70	0.00149	0.05742	1.16074	0.00092	0.03832	1.13249	0.00068	0.03025	1.12055
	180	0.00089	0.03840	1.21621	0.00057	0.02763	1.20015	0.00044	0.02307	1.19337
	450	0.00114	0.05152	1.17101	0.00071	0.03490	1.14416	0.00053	0.02787	1.13281
	1000	0.00114	0.04985	1.11174	0.00071	0.03370	1.08621	0.00053	0.02687	1.07542
	3500	0.00112	0.04660	0.77979	0.00069	0.03034	0.75425	0.00050	0.02347	0.74346

Table 1. Absorption Coefficients (dB/km) calculated using the Francois-Garrison equation. Case 1 uses the values in Table 2. Case 2 subtracts 0.3 pH from the values in Table 2. Case 3 subtracts 0.5 pH from the values in Table 2. These three cases are demonstrated graphically in Figure 7.

z(m)	T(C)	S	pH
1	-1.43	26.33	7.88
30	-1.34	26.62	7.89
70	-0.89	30.72	7.95
180	-1.53	32.99	7.63
450	+0.74	34.83	7.86
1000	-0.05	34.91	7.85
3500	-0.28	34.95	7.87

Table 2. Mean values of T, S, and pH at the given depths. From APLIS 2009.

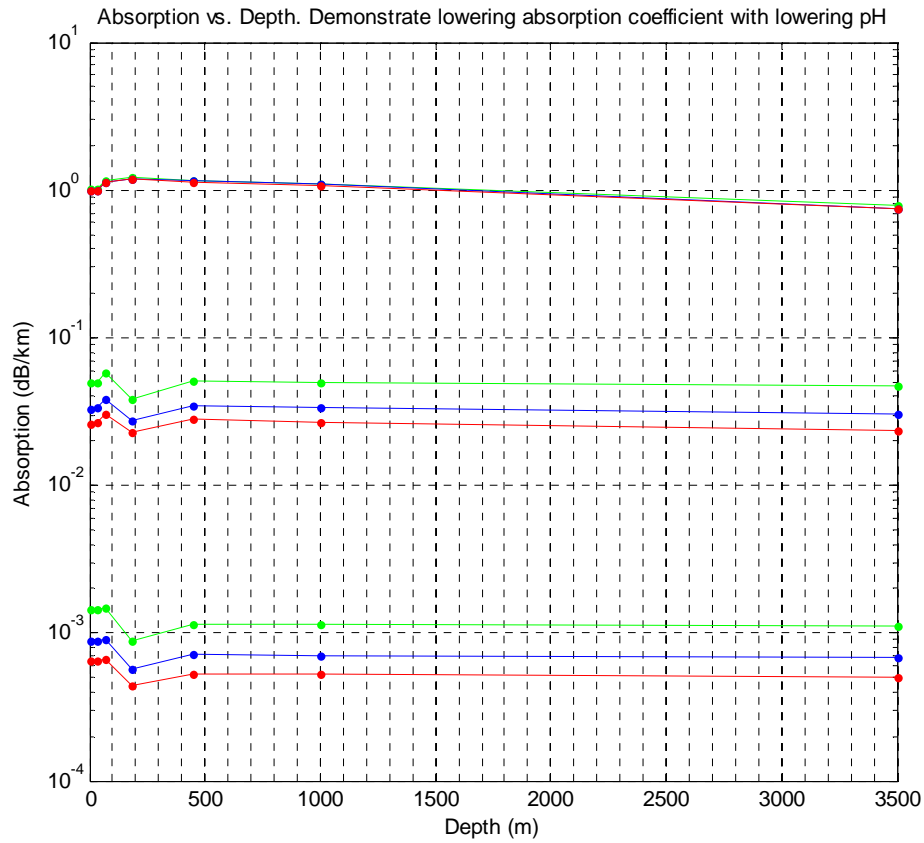


Figure 7. Graphical representation of data in Table 1. The frequency for the three sets of lines are 10kHz for the top set, 1kHz for the middle set, and 100Hz for the bottom set. In each frequency set, the green lines represent the measured pH values at APLIS 2009. The blue lines represent pH lowered by 0.3 pH. The red lines represent pH lowered by 0.5 pH.

III. THEORY

A. ACOUSTIC TRANSMISSION LOSS IN THE OCEAN

Acoustic Transmission Loss (TL), is defined e.g., (Kinsler et al. 2000) as shown in equation(3.1). This shows the relationship between $P(r)$, the pressure amplitude at a range r from a sound source, and $P(1)$, the pressure amplitude at 1m from the source. Transmission loss terms are often grouped into categories of absorption, geometrical spreading, and scattering effects, as shown in equation(3.2).

$$TL = 10 \log \left(\frac{I(1)}{I(r)} \right) = 20 \log \left(\frac{P(1)}{P(r)} \right) \quad (3.1)$$

$$TL = TL_{absorption} + TL_{geo} + TL_{bottom} + TL_{surface} \quad (3.2)$$

1. Absorption

Many factors affect the absorption of acoustic energy in seawater, including thermal conduction and thermal relaxation (Kinsler et al. 2000), the primary mechanisms are viscous absorption (significant above 100kHz), and chemical relaxation due to ocean salts, mainly magnesium sulfate and boric acid (Ainslie and McColm 1998 and Francois and Garrison 1982b). The Francois-Garrison equation for total absorption is given in equation (3.3). Above hundreds of kilohertz, the pure water effect dominates. The magnesium sulfate effect dominates in the region from a few kilohertz to hundreds of kilohertz. Below a few kilohertz, the primary effect is the chemical relaxation of boric acid (Kinsler et al. 2000).

$$\alpha = \frac{A_1 P_1 f_1 f^2}{f^2 + f_1^2} + \frac{A_2 P_2 f_2 f^2}{f^2 + f_2^2} + A_3 P_3 f^2 \quad (3.3)$$

In equation(3.3), the subscript '1' are for boric acid, '2' is for magnesium sulfate, and '3' is for pure water. In this equation, A_x is a coefficient that, for boric acid depends on temperature (T, °C), salinity (S, ‰), pH, and depth (D, m). (Salinity used to be measured by determining the mass (kg) of salt per kg of seawater (given as parts per thousand (ppt,‰), assuming that the composition of sea salt is constant. Later it was determined by a conductivity ratio and listed as ‰, but it had problems with ambiguities due to ionic

ratio variations. The introduction of the Practical Salinity Scale of 1978 calculates salinity as a unitless conductivity ratio to a standard KCl solution (Siedler and Peters 1986). The numerical difference between practical salinity and ppt is small (Sea-Bird Electronics 2010). Equation(3.3) is implemented with practical salinity. For magnesium sulfate, A_x depends on T, S, and depth; and for pure water depends on T only. P_x is the pressure dependency, f_x is the relaxation frequency, and f is the frequency of sound that is of interest. In equation (3.3), the subscript ‘1’ is for boric acid, ‘2’ is for magnesium sulfate, and ‘3’ is for pure water. The boric acid, magnesium sulfate, and pure water dependencies are detailed in the following sections.

a. Pure Water

The amount of sound absorption in pure water is a function of the temperature, pressure, and the frequency of the sound. In general, as the temperature goes up, the absorption goes down. Increasing depth has a similar effect, where deeper depths have lower absorption values (Francois and Garrison 1982a). Higher frequencies have exponentially higher absorption (Francois and Garrison 1982a and Kinsler et al. 2000).

For temperatures less than or equal to 20 °C, the pure water contribution to the absorption shown in (3.3) is

$$A_3 = 4.937 \times 10^{-4} - 2.59 \times 10^{-5} T + 9.11 \times 10^{-7} T^2 - 1.50 \times 10^{-8} T^3 \left(\frac{dB}{km \cdot kHz^2} \right)$$

$$P_3 = 1 - 3.83 \times 10^{-5} D + 4.9 \times 10^{-10} D^2. \quad (3.4)$$

b. Magnesium Sulfate

The sound speed at a given point is a function of temperature, salinity, and depth, and the absorption of sound due to magnesium sulfate ($MgSO_4$) is a function of T, S, depth, and sound speed (Francois and Garrison 1982a). The contribution of a chemical relaxation that involves magnesium and carbonic acid (Mellen et al. 1979) is small and is considered to be included in first two terms of equation (3.3). The equations (3.5) show the $MgSO_4$ contribution to the total absorption.

$$\begin{aligned}
A_2 &= 21.44 \frac{S}{c} (1 + 0.025T) \left(\frac{dB}{km \cdot kHz} \right) \\
P_2 &= 1 - 1.37 \times 10^{-4} D + 6.2 \times 10^{-9} D^2 \\
f_2 &= \frac{8.17 \times 10^{(8 - \frac{1990}{\theta})}}{1 + 0.0018(S - 35)} \quad (kHz)
\end{aligned} \tag{3.5}$$

In equations (3.5) and (3.6), c is the speed of sound (m/s), and $\theta = 273 + T$ is absolute temperature in Kelvin.

c. Boric Acid

The effect that the relaxation of boric acid has on sound absorption is interesting in that it is dependent on the pH of the water in addition to the temperature, salinity, depth, and sound speed (Fisher and Simmons 1977 and Francois and Garrison 1982b). As pH goes up, the absorption increases, and this relationship is exponential (Kinsler et al. 2000 and Francois and Garrison 1982b). This is shown in equation .

$$\begin{aligned}
A_1 &= \frac{8.86}{c} \times 10^{(0.78 pH - 5)} \left(\frac{dB}{km \cdot kHz} \right) \\
P_1 &= 1 \\
f_1 &= 2.8 \sqrt{\frac{S}{35}} 10^{(4 - \frac{1245}{\theta})} \quad (kHz)
\end{aligned} \tag{3.6}$$

2. Geometrical Spreading

An accurate prediction of geometrical transmission loss using ray theory requires a model that sums up the contribution of sound energy from source to receiver along all possible paths by keeping track of the spreading of each path's ray bundles. Unfortunately, although such models are available, none was found that could handle the variable pH effect on absorption. Furthermore, since the focus of this work was mainly on the question of whether pH was important to measure, the decision was made to look at the effect of pH on the absorption losses for each path individually and to assume spherical spreading for the geometric loss. This approach yields a rough guess of the geometrical transmission loss along each path that is independent of pH. Therefore, the effect of absorption due to pH is preserved along these paths.

If sound energy radiates away from a source spherically, the surface area of the wave front increases proportional to the growing surface area of a sphere, as a function of the radius squared. It follows that its pressure amplitude decreases accordingly, and so the TL due to spherical spreading can be written $TL_{spherical} = 20 \log r$ (Kinsler et al. 2000).

This thesis is focused on propagation ranges on the order of 50 km. Due to the strong upward refracting environment, sound rays that leave a source at steep launch angles (greater than 17°) incur additional losses from interactions with the bottom and are assumed to have a negligible contribution to the signal at long ranges (Stotts, S. A., R. A. Koch, and N. R. Bedford 1994) (see also the next section).

3. Bottom Loss

Depending on the bottom structure and composition, acoustic energy can be reflected, scattered, and absorbed. The bathymetry in the Beaufort Sea where APLIS 2009 was established was very flat and roughly 3500m deep (Jakobsson et al. 2008). The bottom type in this area is fine silt and mud (Hunkins et al. 1970). Launch rays were considered ($\pm 15^\circ$) that do not interact with the bottom, since steep angle rays that interact with the bottom undergo additional losses and will not have significant influence on long-range observations (Stotts et al. 1994), and so $TL_{bottom} = 0$.

4. Surface Loss.

a. Sea Surface Effects

The sea surface is a pressure-release boundary, and so sound which is incident upon it is reflected with a phase shift of π . The roughness of the sea surface is a function of the sea state, which is driven by wind. Wave action can entrain bubbles, which, for acoustic frequencies above those on the order of 10kHz the primary source of backscattering (Dahl, P. H., J. W. Choi, and H. C. Graber 2008). There also tends to be more biologic activity near the surface, which can serve to scatter incident acoustic energy. During the course of the data collection, March 2009 in the Beaufort Sea, the open-water fraction was very low, and so the sea surface effects were assumed to be small, and dominated by the ice effects.

b. Ice Effects

Acoustic energy is scattered by interactions with under ice features. Two primary types of features are ice edges and ridges (Fricke 1993). Ice edges occur at the boundaries of leads and polynyas (regions of no ice surrounded by ice coverage (Roth 2003)). If an acoustic wave's angle of incidence on the ice is great enough, it can get transmitted into the ice, travel through the ice, and get reflected off of the air-ice interface. Work in this area was done using geophones buried in the ice to measure sound coupled from the ocean. It was shown that for long range propagation, the rays that penetrate the ice are not important when the source and receiver are both in the water (Stotts et al. 1994). In order for an acoustic ray to penetrate into the ice, it needs to have a steep angle of incidence. This results from the much larger speed of sound in ice, compared to the speed of sound in the seawater below the ice. This difference in sound speed leads to a large difference in the indices of refraction.

Consider an acoustic ray that is incident from the water to the ice, where the ice has sound speed $c_2 = 3,200$ m/s, (Kinsler et al. 2000), and the water has $c_1 = 1,430$ m/s. Then the index of refraction $n = c_1/c_2$. The minimum (critical) θ_c required, for a ray to propagate in the ice is $\theta_c = \cos^{-1}(n) = 63.5^\circ$. Judging from this, all of the rays within an angle of $\pm 15^\circ$ are reflected back into the water and do not penetrate the ice.

The scatter-absorption contribution to the transmission loss due to interactions with the ice is calculated from $TL_{ice} = -10 \log R$, and Diachok's 1976 equation (3.7), which gives the energy reflectivity R . R is the ratio of energy that gets reflected cleanly in the initial travel direction. The acoustic ray is assumed to be otherwise perfectly reflected from the ice. For this equation, ridges are assumed to be half cylinders, with length much greater than width, with average keel depth d , and spatial frequency N . x is the correction for the eccentricity of an ellipsoid ice ridge form. This is assumed to be 1.0 since Diachok assumes a ridge is half of a right circular cylinder.

$$R = \left(\frac{1 - \frac{xNd}{\theta_1}}{1 + \frac{xNd}{\theta_1}} \right)^2 \quad (3.7)$$

This theoretical equation proposed for frequencies such that $kd > 1$, where k is the wavenumber: $k = 2\pi/\lambda$. For the ice drafts and frequencies studied, $kd > 1$, and so this ice scatter-absorption model is independent of further considerations of frequency.

B. SOUND SPEED PROFILE

Sound travels through a medium as a compressional wave in a series of compressions and rarefactions. The sound speed profile is often considered to be radially homogeneous and range-independent. Even so, inhomogeneities in temperature and density change how a sound ray refracts as it propagates. This study considers vertical structure as measured by CTD in the upper ocean and concatenated with deeper data sources to develop sound speed profiles for the full water column. It will not, however, consider range-dependence of the sound speed profile because over the 50km range surveyed, the variability in SSP due to spatial separation was not significantly different from the variability due to the ice sheet drifting or the time separation between profiles.

Similarly, differing media can have quite different sound speeds. For example, the speed of sound in air at 0°C is 331.5m/s, in molecular hydrogen at 0°C; it is 1,269.5m/s. In steel, the speed is nominally 6,100m/s, but only 3,200m/s in ice (Kinsler et al. 2000). Near the surface in the Beaufort Sea, the annual average seawater sound speed is 1,434m/s, and 1,507.5m/s near the bottom at 3,500m. These sound speeds were calculated from World Ocean Atlas 2001 salinity data (Boyer et al. 2002) and temperature data (Stephens et al. 2002). The speed of sound in the ocean has been measured extensively. There is little ambiguity about the measured sound speed for a set of given conditions. There is, however, much debate about how to develop a mathematical equation to describe how the speed of sound in the ocean varies as a function of temperature, salinity, and pressure (which is related to depth and latitude) (Mackenzie 1960, Wilson 1960, Del Grasso and Mader 1972, Del Grasso 1974, Chen and Millero 1977, and Leroy et al. 2008).

The Navy's Oceanographic and Atmospheric Master Library first accepted Wilson's 1960 equation as the Navy Standard. When the Navy's mission focus shifted to more littoral, "brown water" areas, many sound speed equations were tested. The

approved standard sound speed algorithm for the United States Navy is the Chen and Millero equations from 1977, as modified by Millero and Li in 1994. Recently, however, there were issues. The algorithm, implemented as CML 1.0, would give erroneous SSP results when users attempted to calculate sound speed profiles in regions like the Red Sea. This was because there were instances when the salinity (>40) was higher than the limits in the program. The previous limits were: temperature (0 to 40) °C, salinity (5 to 40) , and pressure (0 to 1,000 bar) (Krynén 2010). The limits were expanded and the modified algorithm, CML 1.1, was approved January 26, 2010 as the new Navy Standard Sound Speed Algorithm (Moskal 2010). The revised limits are: temperature (-3 to 40) °C, salinity (0 to 45) , and pressure (0 to 1,100) bar (Naval Oceanographic Office 2009). A comparison of SSPs generated by several equations is shown in Figure 8. Given the profiles obtained at APLIS 2009, the difference between algorithms is insignificant. The maximum difference is at 3500m, when there is a 0.009% difference between CML 1.1 and Mackenzie, 1960, as shown in Figure 8. In the upper ocean, the variability in SSP due to selection of equation set is dominated by variability due to unique T and S profiles.

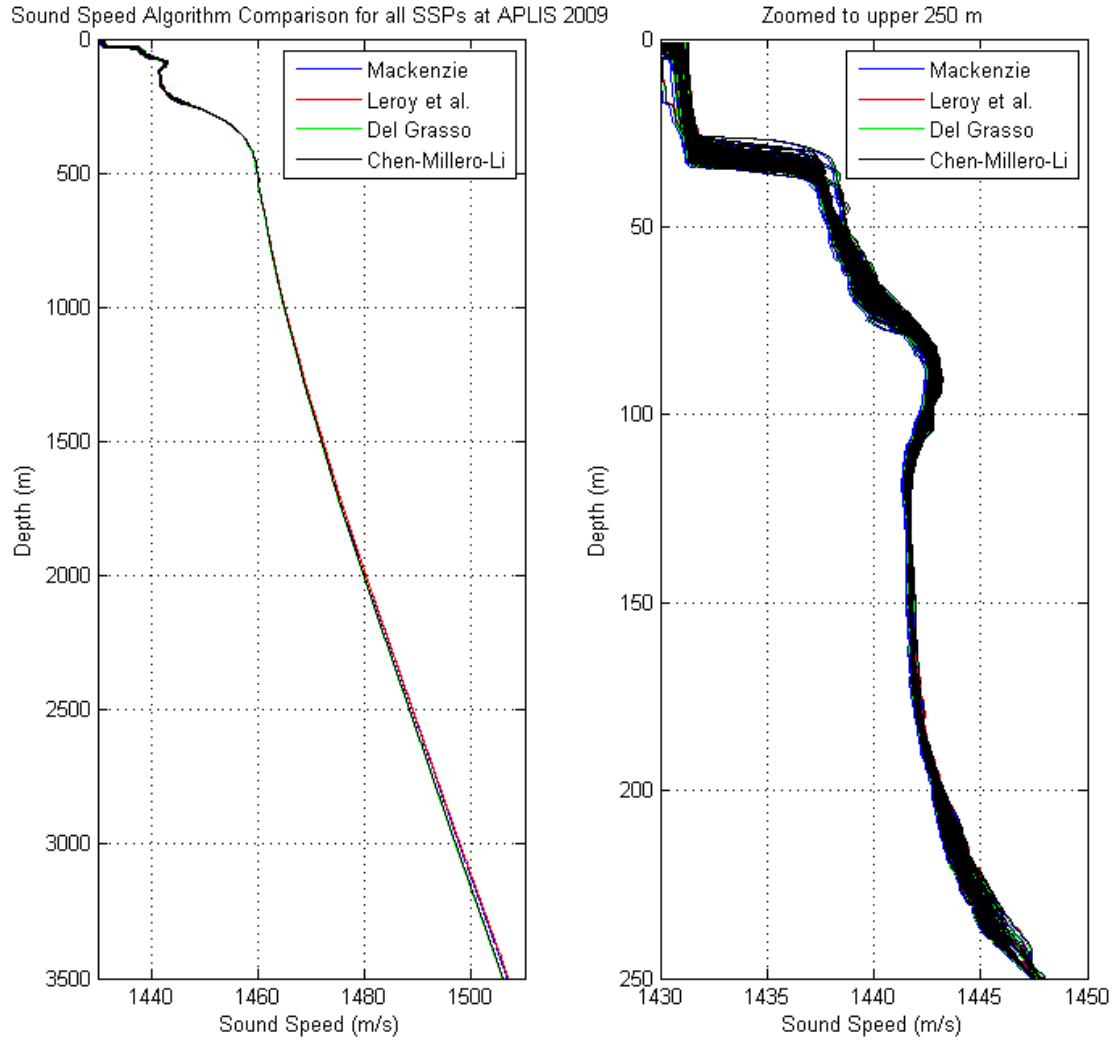


Figure 8. Comparison of sound speed profile equations. The plot on the left uses the listed algorithms for determining sound speed from all the profiles of T and S at APLIS 2009. The plot on the right uses the same data and is zoomed into the region where most data acquisition occurred. Note that profiles were conducted to a maximum depth of 518m. The variability due to algorithm choice in the upper ocean is dominated by the consequences of T and S variability.

IV. EXPERIMENTAL SET UP AND DATA COLLECTION

A. EQUIPMENT

1. Seabird SBE19plus V2



Figure 9. Sea-Bird Electronics SBE 19plus V2 with SBE18 pH sensor. As deployed at APLIS 2009.

This conductivity-temperature-depth profiler (CTD) employed a SBE 5M Mini Submersible Pump which maintained a constant flow through the conductivity cell and temperature sensor regardless of CTD motion. It minimized salt spiking arising from mismatched time responses between the temperature sensor and conductivity cell. The resulting fast response along with a slow vertical travel time of 0.5m/s provided enhanced resolution of the vertical structure. Sampling at 4Hz, eight measurements were logged every meter. In the Arctic environment, it was very important to protect the glass conductivity cell from damage and freezing. If water freezes onto a conductivity cell, the measurements are inaccurate. It was also important to ensure that the water was clear prior to lowering the CTD into the water to prevent debris from entering the instruments. When the CTD was not in use, it was suspended in the hut, where the temperature was maintained near 22°C.

As an add-on to the CTD, a SBE 18 pH sensor was used to study the structure and variability in the pH of the upper ocean. This sensor uses a pressure-balanced glass-electrode Ag/AgCl-reference pH probe. For most of the profiling, it was attached to the side of the CTD housing, as shown at the bottom of Figure 9. In this configuration, the diameter of the CTD was 0.23m. The largest hole that could be drilled with the portable auger was 0.1524m, so for the helicopter-assisted radial casts, the sensor was

repositioned and attached to the bottom end of the CTD housing. This repositioning lowered the pH sensor 0.5m, and the resulting CTD diameter was about 0.15m.

The intent had been to profile to 300m, but upon testing the winch and pulley apparatus with a 7kg test weight (CTD as used was 8.3kg), it became evident that instead of 305m of line there was only about 250m of line. It was decided to profile to 233m to allow a safety buffer of line on the spool. A Shimano Dendou-Maru deep-sea fishing reel was used as the winch, with a very thin Spectra/Nylon 100 lb-test line going through a small pulley system.

B. DATA COLLECTION

1. Work Area Setup

Most of the CTD operations were performed from a working/sleeping hut assembled by the APL-UW APLIS team. The hut was constructed on 1.28m of ice, and placed over a 0.46m hydro-hole that was melted through the ice sheet.

2. Equilibration

Initially, the CTD was allowed to equilibrate for eight minutes at 1m but it was later determined that it could be more effective to lower the CTD to 7.5m for 15 minutes for equilibration. The reason for lowering the CTD further for equilibration was that the hydro-hole was maintained open by two heat tapes on opposite sides of the hole, extending to the bottom of the ice. In addition, the surface was kept from freezing by a fan circulating warm air from the top of the hut to the surface of the hole. Lowering the CTD to 7.5m allowed the sensors to equilibrate away from the warmer, fresher water in the hole. It was subsequently noted that there was little change in the parameters after five minutes, and the final equilibration routine was established as 7.5m for five minutes.

3. Time Series

To study the tidal and diurnal variability in T, S, and pH, a 36-hour time series was conducted. During the time series, 124 profiles were obtained to an average depth of 233m, lowering the CTD every 14.5 minutes. While continuous profiling for the entire time would have been desirable, the pulley wheel often seized and required periodic maintenance and lubrication.

4. Daily Casts

After the time-series, six CTD profiles to 233m were obtained each day, one profile or down-cast for the descent, and one profile or up-cast for the ascent. The sound speed profiles were calculated and transmitted to the participating submarines each day so that they could more accurately predict acoustic propagation in the ocean. Twice the water was profiled to 518m making use of a heavy-duty winch assembly borrowed from APL-UW.

5. Radial Survey

In order to study the spatial variability of the water properties and therefore the spatial variability and range dependence of the sound speed profile, a survey away from the ice camp was conducted. Using a helicopter for transportation, two profiles were obtained at each of five locations. The average spacing was 9.4km, and the line of bearing from the camp was 039°. Including two profiles conducted back at the camp (the 0th radial stop), twelve profiles were obtained in all.

Three of the down-casts from field surveys were erroneous due to a suspected ice clog on the intake of the conductivity cell. The temperature and salinity readings returned to normal halfway down, but because of this problem, these three profiles were subsequently discarded and replaced with the corresponding up-casts. The up-casts and down-casts were very similar.

C. DATA UPLOAD/CONVERSION

After uploading the data from the CTD, it was converted from .hex format with SBE Data Processing, Version 7.17a (Sea-Bird Electronics 2008). The temperature (T) is output as degrees Celsius according to the International Temperature Scale of 1990 (ITS-90). The conductivity is output in mS/cm (milliSiemen/centimeter). The pressure is converted and output as depth in meters of seawater. pH is calculated from the voltage of the pH sensor and the temperature. Salinity was then calculated by the equations from the Practical Salinity Scale of 1978 (PSS-78) and is expressed as a unitless conductivity ratio (Fofonoff and Millard 1983).

D. EQUIPMENT MAINTENANCE

After profiling, the entire CTD was rinsed with fresh water. The conductivity cell was then flushed with 0.1-0.2% Triton X-100 solution, deionized (DI) water or fresh water, and drained. Prior to use, the conductivity cell was filled with Triton for one hour and then drained. Triton (Octyl Phenol Ethoxylate) is a mild non-ionic surfactant (Sea-Bird Electronics 2008). Flushing of the conductivity cell prior to and after profiling was accomplished in accordance with manufacturer's procedures. When the CTD was not being used, the inlet to the conductivity cell and the outlet of the SBE 5M Mini Submersible Pump were connected with a length of Tygon tubing to prevent airborne contaminants from entering the conductivity cell.

When not in use, the pH probe was kept clean and wet in its buffer solution saturated with potassium chloride (KCl). This soaker fluid is acidic (pH 4) and is designed to keep the electrode free of marine fouling. The internal electrolyte contains antibacterial inhibitors and is non-organic to support use in the ocean (Sea-Bird Electronics 2010).

The pH sensor was calibrated daily using buffer solutions of pH 10, 7, and 4. Prior to calibration, the sensor was soaked in DI water for 30 minutes. This soaking allowed the charge balance around the sensor to stabilize and was performed in accordance with the Sea-Bird Electronics calibration procedures.

E. GPS LOGGING

The position of the profiles was logged for the start of each cast. GPS position was logged continuously throughout the course of APLIS 2009. For this, an external antenna was mounted to the top of the working hut and connected to a computer that logged the position at 1Hz. A handheld GPS receiver logged the positions of the radial casts.

V. ANALYTIC METHOD AND DATA ANALYSIS

A. DATA PROCESSING

The MATLAB functions referenced below were developed by Stanton's Ocean Turbulence Group (OTG) at the Naval Postgraduate School (Stanton 2003).

1. Profile Isolation

Usually, there were many profiles together in one data file since data collection commenced upon activation of the magnetic reed switch, which supplied power to the CTD. Many profiles were conducted before removing the CTD from the water and securing power. After the CTD data was converted from hexadecimal to ascii format using the Sea-Bird Data Processing program, the profiles were separated out for comparison. The periods during equilibration, between profiles, and before securing the CTD were removed from the profiles. These data were saved for later reference, being useful for studying sensor equilibration behavior and sensor stability. They were, however, not applicable when comparing individual profiles.

2. Binning

The profile data were consolidated into one-meter bins to facilitate processing and comparison. To do this, the OTG MATLAB function *ctd_bin.m* was used. It averaged the values between $z-0.5\text{m}$ to $z+0.5\text{m}$ to be the value for that profile at z meters. Profiling at 0.5m/s gave approximately eight measurements to average for each binned meter. *ctd_bin.m* also separated out individual profiles (making a down-up set into a downward profile and an upward profile). In order to isolate the turning points between a down and up profile, a third order low-pass Butterworth filter was temporarily applied to the depth vector. This allowed the actual profiles to be separated from pressure fluctuations due to sway or uneven motion due to operation of the winch.

3. De-spiking Measurements

An OTG MATLAB function *despike.m* was used to de-spike conductivity. The most probable cause of spiking is biota being swept into the suction of the conductivity cell. It removed spikes exceeding a threshold value (40 mS/cm) by interpolating between the adjacent points.

4. Temperature Structure

The temperature in the mixed layer, the upper 30m, was very uniform. In the upper ten meters, the minimum temperature was -1.451°C , the maximum was -1.402°C , with a mean of -1.430°C and standard deviation of 0.010°C . This is expected, because it is very close to the freezing temperature of the seawater at the salinity measured in the mixed layer. The salinities ranged from a minimum of 25.753 to a maximum of 26.751, with a mean of 26.360 and standard deviation of 0.103. These values are displayed in Table 3. Statistics for the thermocline and halocline, depth of greatest temperature and salinity change, respectively, are also shown in Table 3. A plot of the thermocline and halocline data is shown in Figure 10. Ten of the measurements on day 88 were performed as part of the radial surveys, five stops at 9.4km increments from APLIS. Measured temperature structure is shown in Figure 11.

	min	max	μ	σ
temperature ($^{\circ}\text{C}$), upper 10m	-1.451	-1.402	-1.431	0.006
salinity, upper 10m	25.753	26.751	26.360	0.103
thermocline depth (m)	29	36	32.190	1.300
halocline depth (m)	29	36	32.174	1.082

Table 3. Temperature and salinity minimum, maximum, mean, and standard deviation for the upper 10m. Also shown are the statistics for the thermocline depth and the halocline depth.

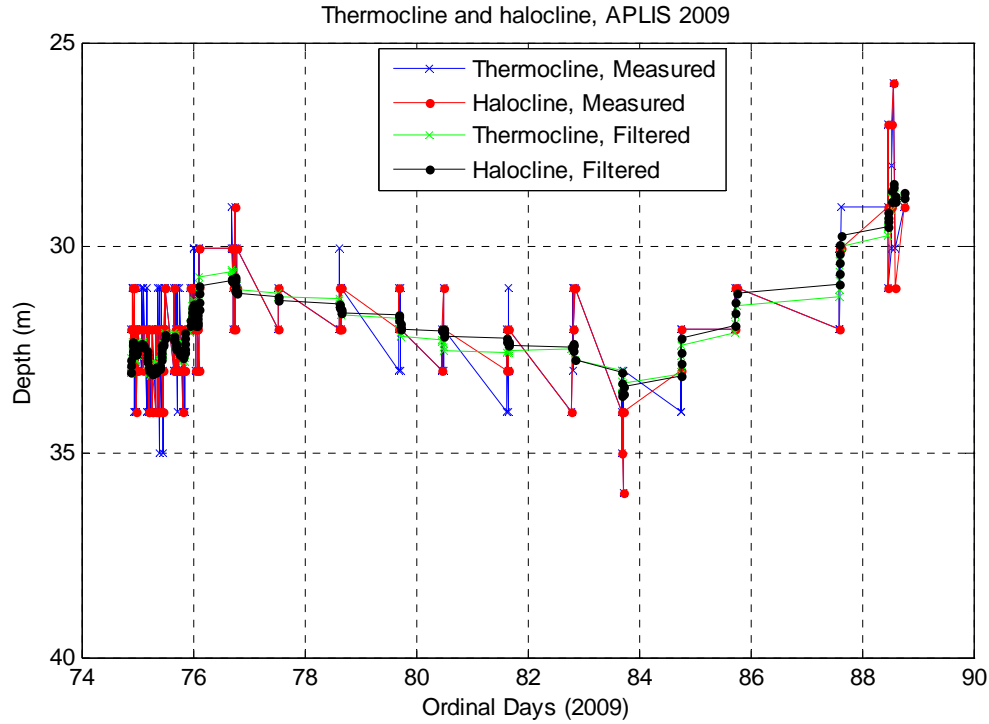


Figure 10. Thermocline and halocline depths versus time, in Ordinal days. The green and black lines represent the data after being filtered to indicate thermocline and halocline depth trends.

5. Salinity Calculation

Salinity was calculated using the MATLAB function *salinity.m*. This function uses the Practical Salinity Scale of 1978 equations from Fofonoff and Millard, 1983 in the UNESCO papers. This program uses temperature ($^{\circ}\text{C}$, ITS-90), conductivity (mS/cm), and depth (as decibars) to generate unitless salinity from the ratio of measured conductivity to reference conductivity. The reference is the conductivity of standard seawater of practical salinity 35, $T=15^{\circ}\text{C}$, and atmospheric pressure. By definition, it is equal to the conductivity of a reference solution of potassium chloride (KCl) at the same temperature and pressure (Fofonoff and Millard 1983). The salinity structure measured at APLIS is shown in Figure 11.

The structure of the salinity profile shows the mixed layer extending to about 32m depth. The bulge at 100m is the center of the upper halocline layer (UHL), and is primarily of Pacific Ocean origin (Bates et al. 2009). The slightly concave-up section

from about 150m to 230m is the lower halocline layer (LHL), made up of waters originating from the Atlantic Ocean but modified during transit (Bates et al. 2009). The salinity profile changes very little in the rest of the water column. Bates describes two additional layers of Atlantic origin, the Atlantic Water Layer, and the Arctic Ocean Deep Water, but salinity is very near 35 for both.

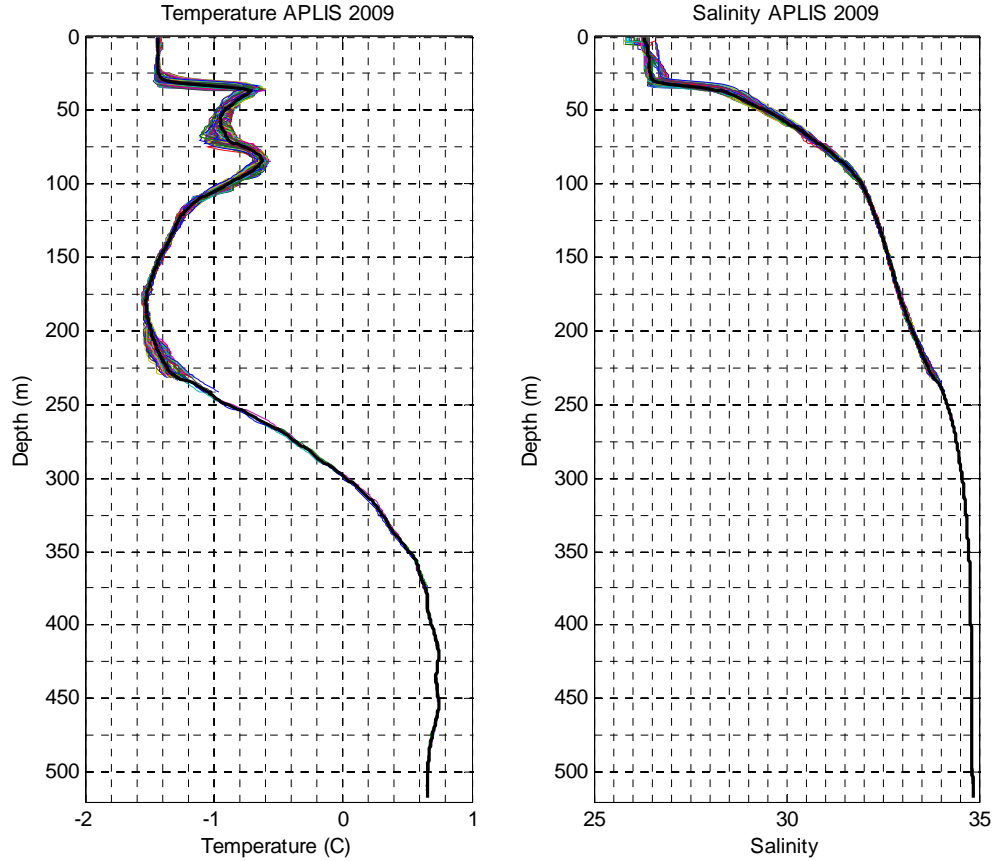


Figure 11. Temperature and salinity measured at APLIS. Radial survey data is excluded.

6. pH Structure

In order to measure pH, the voltage was measured across the glass electrode of a Seabird Electronics SBE-18 pH sensor. This output voltage and the measured temperature were used by Sea-Bird's SeaSoft Data Processing Software to calculate pH. Equation (5.1) shows how the pH value is calculated. V_{out} is the output voltage of the sensor (0-5 volts), T is the measured temperature (K), *slope* and *offset* are calibration coefficients.

$$pH = 7 + \left(\frac{V_{out} - offset}{1.98416 \times 10^{-4} * T * slope} \right) \quad (5.1)$$

When calibrated at the manufacturer in February 2009, the values were $slope = 4.3350$ and $offset = 2.5277$, when the temperature was 20.8°C . The sensor was calibrated daily at temperatures that ranged from 19.3°C to 25.4°C .

During the experiments, the pH sensor had an unexpected temporal drift following power-on and subsequent change from room temperature to the -1.4°C seawater, as shown in Figure 12. The indicated pH would generally rise as the time in the water increased. When the CTD was removed from the water and powered off (for data upload and equipment maintenance), and then lowered again into the water, the measured pH was lower.

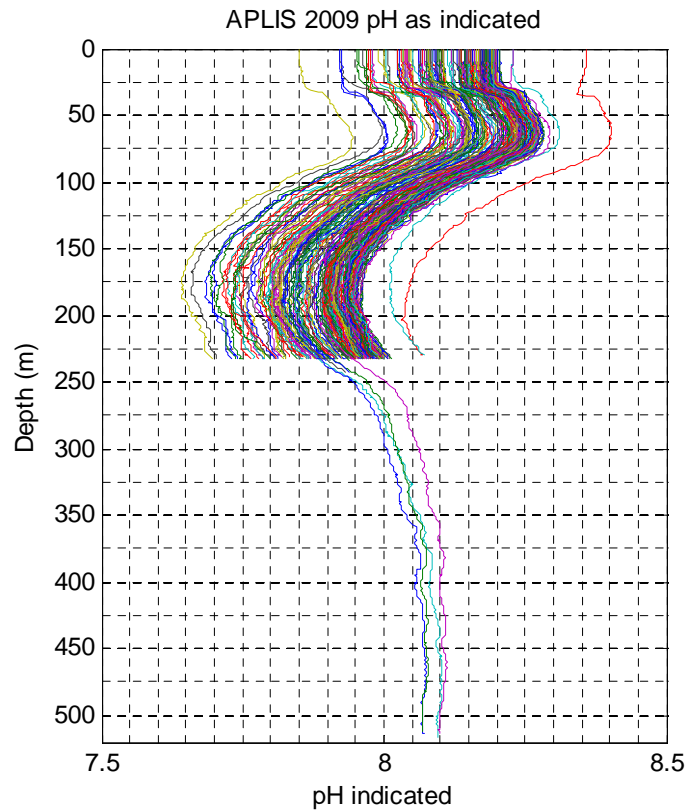


Figure 12. pH as indicated. Note that the shape of the structure is very similar for the profiles.

This drift occurred despite allowing the CTD to remain in the water for an average of eight minutes during equilibration. Following a step change in pH, the SBE 18 is designed to respond to 63% of the final pH value within one second. Subsequent discussions with technical staff at Sea-Bird Electronics showed that a similar effect had been seen in the lab. Taking the sensor from room temperature to a 1°C test bath during thermal shock tests, the manufacturer noted that it often takes up to 15 minutes for the pH sensor to reach 99% of the final value. The pH sensor used for this research, however, seemed to be equilibrating over the course of hours. This behavior, as observed in the time series at the beginning of APLIS, is shown in Figure 13.

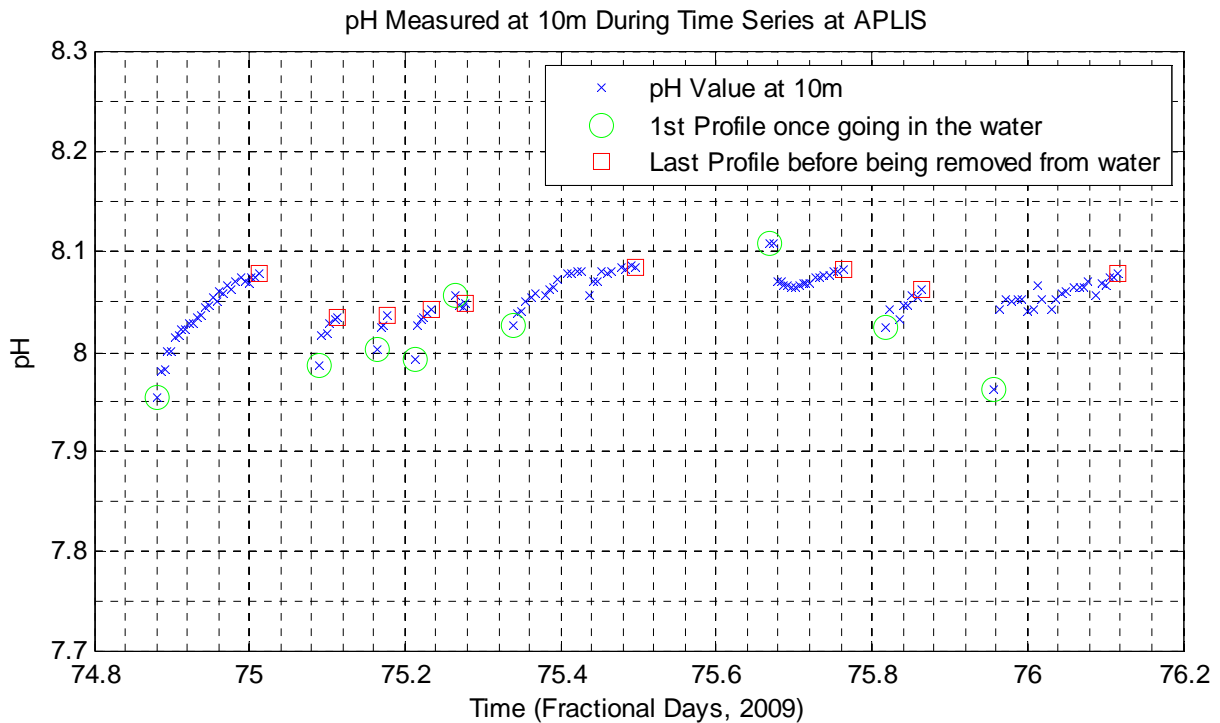


Figure 13. Measured pH at 10 meters vs. time, during the time series at APLIS. This plot demonstrates the effect of equilibrating over hours instead of seconds to minutes.

Each day the pH sensor was calibrated to a set of buffer solutions of pH 10, pH 7, and pH 4 at room temperature. The indicated pH was consistently higher than the pH 7 and pH 10 buffers, and lower than the pH 4 buffer. With respect to the pH 7 buffer, the sensor indicated high each time by about $\Delta pH = 0.1187$.

The time-dependent behavior was not observed during the calibrations; instead, the indicated pH rapidly approached the buffer value. It was noted that the temporal drift could have been a result of the large difference between the temperature of the air in the hut and the temperature of the seawater. The matter is being pursued with the manufacturer, but it could have been an issue with ionic balance between the buffers (which have a deionized water base, and a correspondingly low ionic strength) and the seawater (which has a high ionic strength) (see Zeebe, R. E. and D. A. Wolf-Gladrow 2001). It could have also been an issue with the ionic balance between the pH 4 potassium chloride soaker solution that the pH sensor stayed in when not in use, and the seawater. It could have also been a combination of the two.

To help resolve the slow turn-on drift in the pH sensor, Leif Anderson, a polar ocean chemist from the University of Gothenburg, was consulted. It was determined that it would be safest to match the pH data at the depth of least environmental variability. This was the depth of minimum temperature, 181m. This approach is shown in Figure 14. Also, in this figure are pH measurements obtained by Anderson from a cruise through the same region of the Beaufort Sea in Fall 2005. These measurements were conducted by obtaining water samples at discrete depths and conducting chemical analyses to determine the pH.

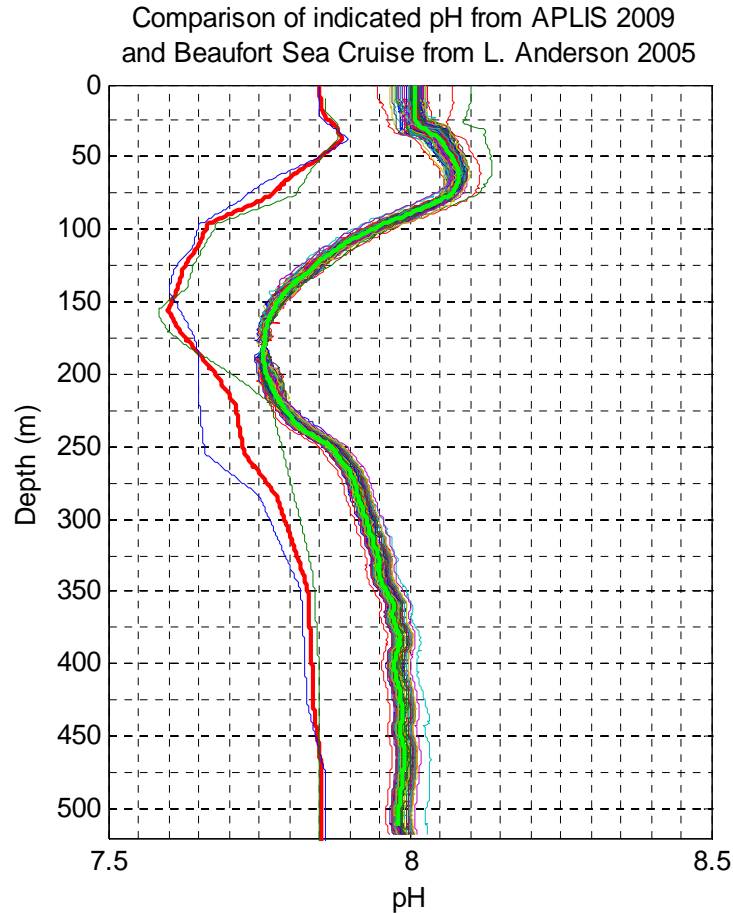


Figure 14. The red curve is the mean of two profiles from Leif Anderson's Fall 2005 Beaufort Cruise. The light green is the mean of the collapsed APLIS data.

Since the majority of pH profiles were conducted to 233m, the mean of the 4 deeper casts was aligned with the end of the shallower profiles to extend each profile to 518m. Due to low diffusivity and slow vertical transport, CO_2 variability is largely confined to the upper hundreds of meters (Bates et al. 2006) and is largely invariant at depth (Anderson 2005). Because pH values for the full water column were needed to facilitate absorption calculations along the ray path, a decision was made to utilize Anderson's pH data. This was accomplished by maintaining the measured pH structure from APLIS and translating the profiles so that the mean of the measured pH profiles aligned with the mean of the Anderson's data. The transition points were then smoothed using a rectangular convolution filter. The resultant pH profiles are shown in Figure 15.

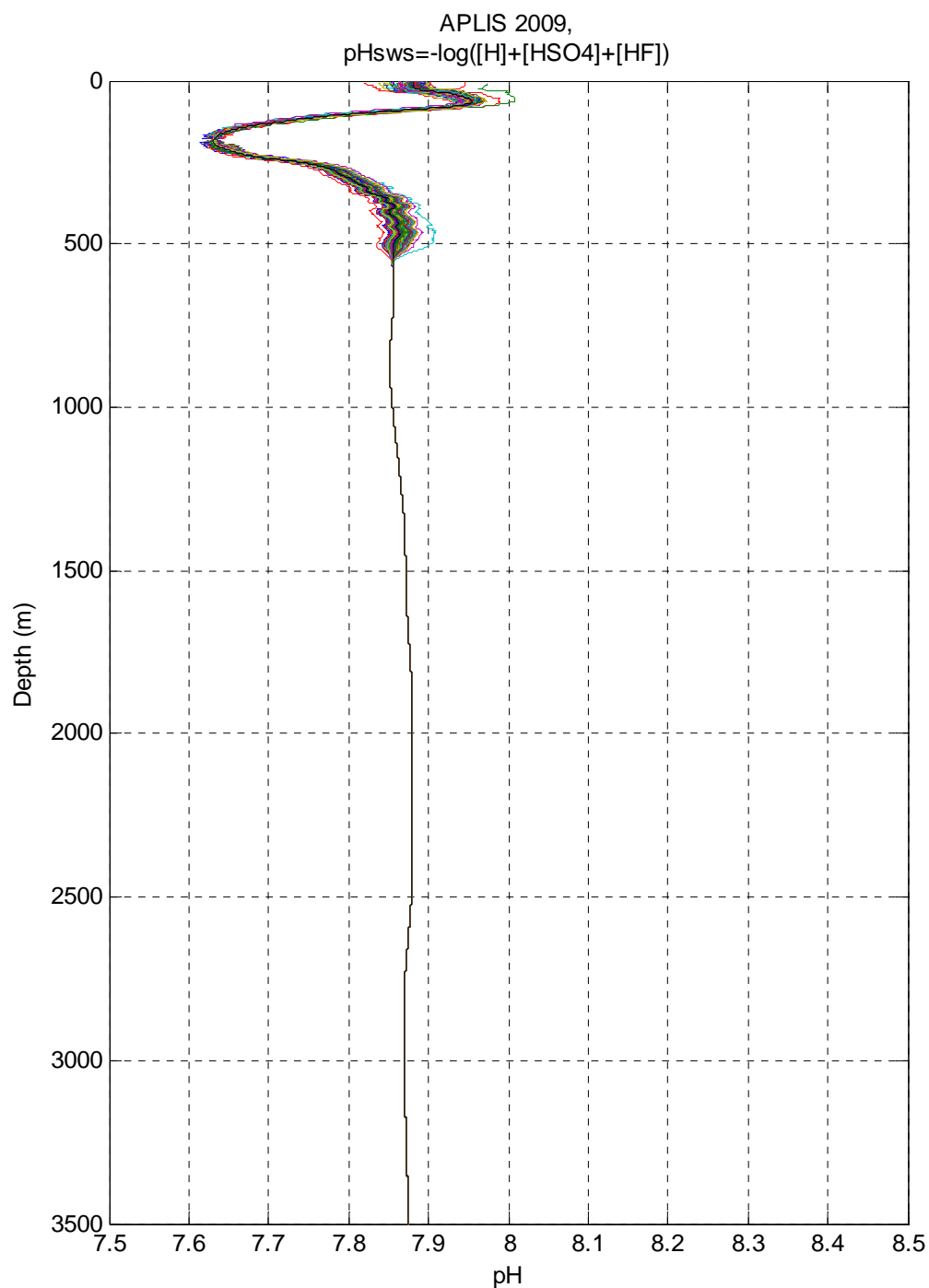


Figure 15. Full water column pH profiles. Shallow data is from APLIS 2009, aligned with deep data from Anderson 2005, using the Seawater pH Scale.

There were also other choices regarding the pH scale and its temperature-correction. One convention is to adjust pH measurements based on temperature such that

a neutral solution will be measured pH 7 at 25 °C. The convention used by Anderson was to temperature-correct pH to 15°C. Regarding pH scale, there are different scales used in chemical oceanography depending on the focus of the study (Bates 1975). The scale used by Anderson was the seawater scale, where the pH (denoted pH_{SWS}) includes the concentration of hydrogen sulfate ions and fluoride ions, as well as hydrogen ions, as shown in equation(5.2). $[H^+]_F$ is the concentration of “free” hydrogen ions (which includes hydrate complexes like H_3O^+ , where a hydrogen ion combined with a water molecule to form hydronium); $[HSO_4^-]$ is the concentration of sulfate ions; and $[HF]$ is the concentration of fluoride ions. The fluoride effect is small since the concentration of fluoride ions is much lower than that of the sulfate ions (Zeebe and Wolf-Gladrow 2001).

$$pH_{SWS} = -\log([H^+]_F + [HSO_4^-] + [HF]) = -\log[H^+]_{SWS} \quad (5.2)$$

If the pH data were left aligned with the deep Arctic Ocean pH from Anderson to deal with the temporal drift, then the APLIS data would end up being temperature corrected to 15 °C and using the seawater pH scale. In the field of acoustics, however, the free pH scale is used ($pH = pH_F$), which accounts for the concentration of hydrogen ions alone, as shown in equation (5.3) (Zeebe and Wolf-Gladrow 2001).

$$pH_F = -\log[H^+]_F \quad (5.3)$$

Because of this difference in scales, it was necessary to attempt to convert the pH to the free scale. pH is a complex measurement variable that depends on the relative concentrations of numerous constituents of an acid-base system. There is not a straightforward conversion that can be applied. There is, however, a relation that shows that the difference between ($pH_F - pH_{SWS}$) is about 0.12 units at T=25 °C, and S=35. Applying this difference, $\Delta pH = 0.12$ was added to the pH profile shown in Figure 15. The final pH profiles used for absorption calculations are shown in Figure 16.

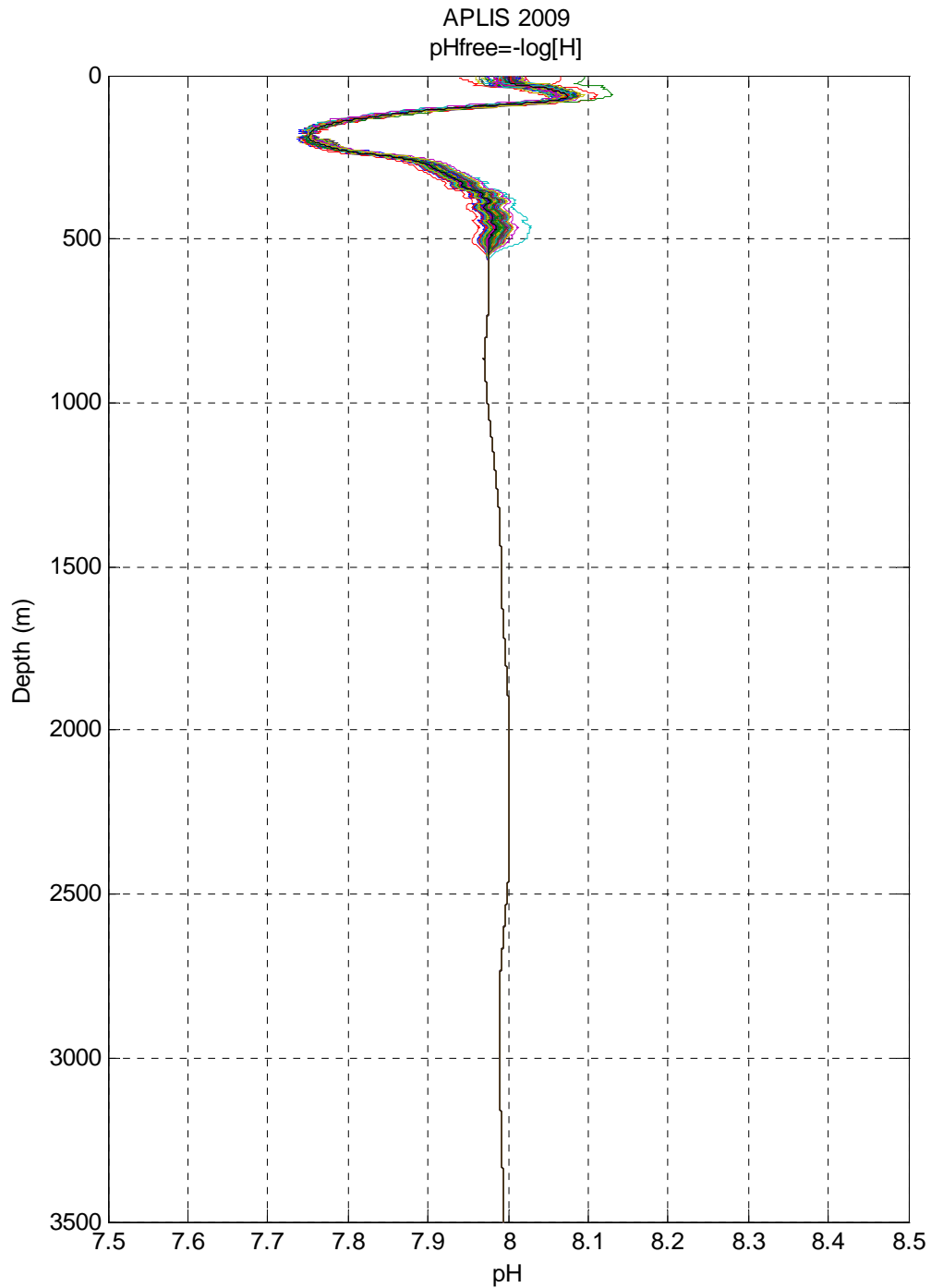


Figure 16. Free scale pH profiles used for absorption calculations.

B. DATA FOR DEEP WATER

In order to use the ray tracing method for acoustic propagation, the sound speed profile for the entire water column must be known, and this is determined from the full

water column temperature and salinity profiles. As discussed in the previous section, the majority of data collected at APLIS was to a depth of 233m with four deeper profiles to 518m. In order to extend the depth of profiles at the camp through the whole water column, the mean of the four deep profiles was concatenated with and aligned to the lower 15m of the shallow profiles. The measured and extended profiles for temperature are shown in Figure 17. Similarly, the corresponding plots for salinity are shown in Figure 18.

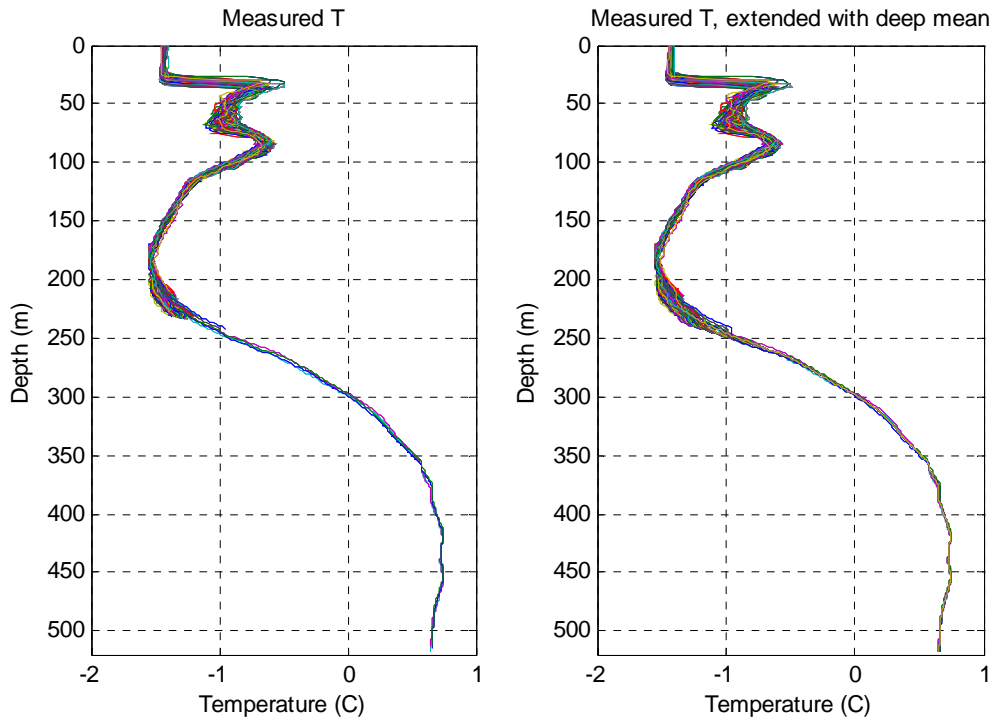


Figure 17. (L) Measured temperature profiles (four to 518m, 198 to 233m average depth) and (R) measured temperature profile extended to 518m with the mean of the deep profiles.

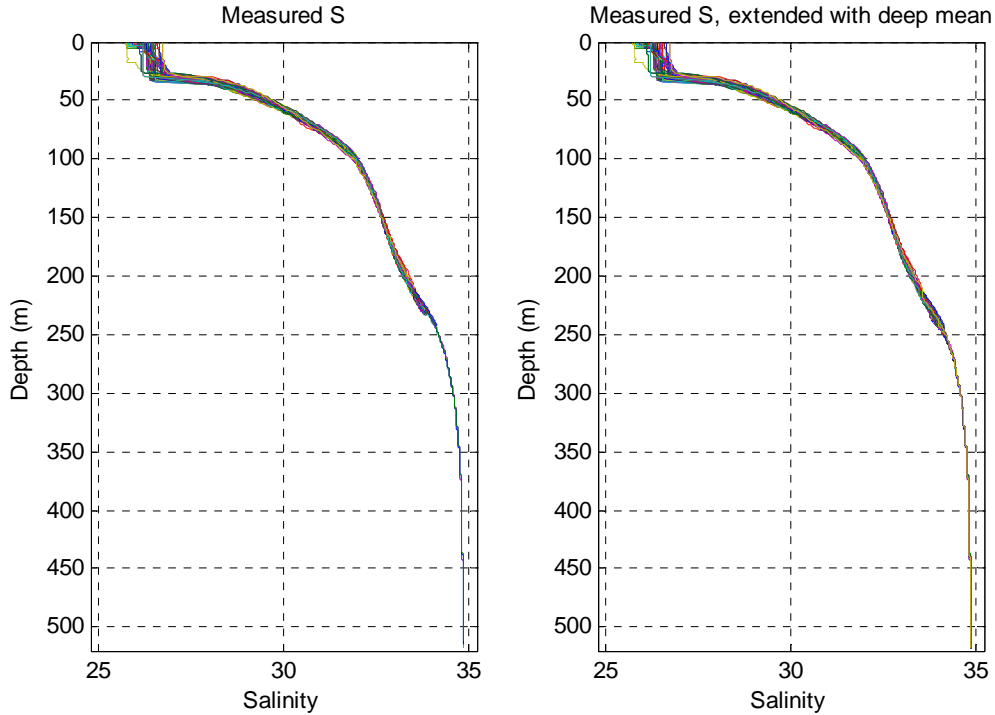


Figure 18. (L) Measured salinity and (R) measured salinity extended with the mean of the deep profiles. These plots are nearly identical, highlighting the low variability of salinity below the upper ocean. The transition regions where the shallow profiles are extended are visible when comparing the areas between 200m and 250m.

The next step for extending the depth of the T and S profiles was to incorporate data collected at about the same time from an Ice-Tethered Profiler (ITP) that was located near APLIS. The Ice-Tethered Profiler data were collected and made available by the Ice-Tethered Profiler Program based at the Woods Hole Oceanographic Institution (<http://www.whoi.edu/itp>). Two profilers were active near APLIS. ITP 21 was located 454km bearing 028°, and ITP 11 was located 496km bearing 057°. The data from ITP 21 was more similar to the deep casts from APLIS suggesting a more similar water mass. Each day the ITP profiled to 760m and measured T and S. Because of this similarity between APLIS and ITP data, the mean of the daily ITP 21 data from 500m to 760m was added to the bottom of the extended APLIS data, assuming that the mean was a good representation of T and S in this depth range over this time. The ITP data is provided with 2m bin spacing. It was linearly interpolated to obtain 1m bin widths.

For data in the rest of the water column, a data set was selected from the World Ocean Atlas (WOA) of 2001. This data set was provided by the National Oceanographic Data Center (National Oceanographic Data Center 2007). The WOA profiles provide data at 33 standard depth levels and were linearly interpolated to obtain one-meter bin widths. The WOA database has data for half-degree increments of latitude and longitude. Selecting the closest location in the database to APLIS (33km North), full water column profiles for T and S were obtained. The profiles were an annual average, and the values from 760m to 3500m were added below the ITP 21 data. Comparison of the WOA, ITP 11, ITP 21, and the mean of the deep profiles from APLIS are shown in Figure 19.

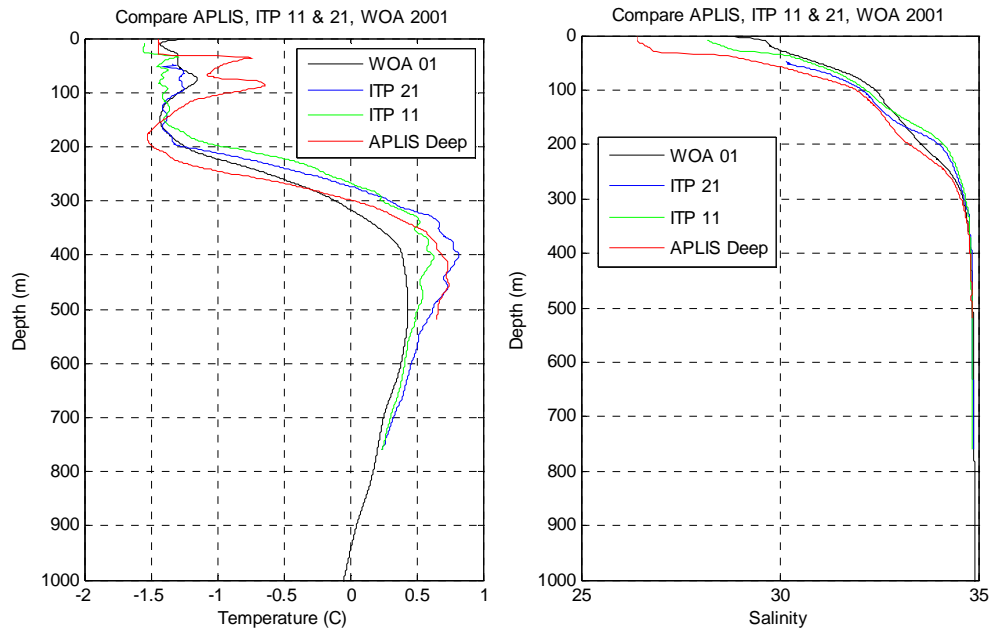


Figure 19. (L) Temperature profiles from WOA2001 near APLIS, ITP 11, ITP 21, and the mean of the deep profiles obtained at APLIS. (R) Salinity profiles from the same sources.

Combining these data sources allowed for the estimation of full water column profiles for temperature and salinity, while capturing the measured variability in the upper ocean. It was assumed that for the times studied the variability of T and S below 760m was negligible, and the annual average at this location was a good representation of the deep ocean T and S. The full water column profiles used for ray path and absorption calculations are shown in Figure 20.

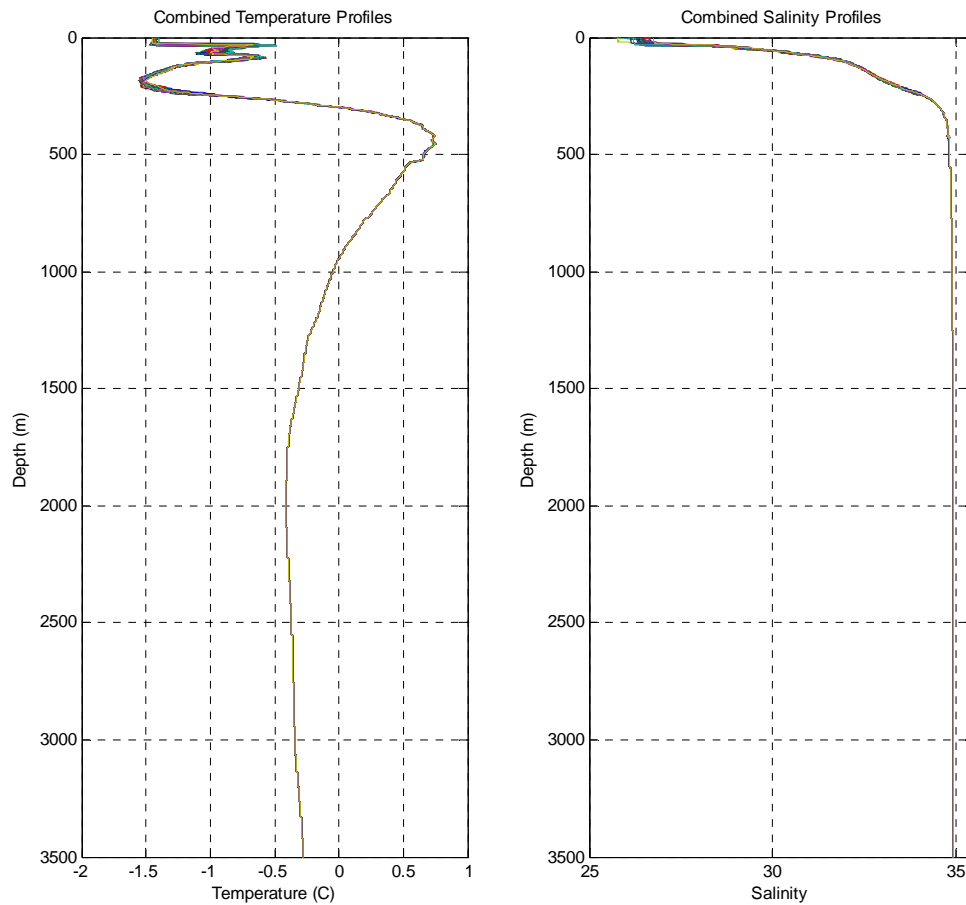


Figure 20. Full water column T and S profiles used to calculating sound speed and absorption.

C. SOUND SPEED PROFILES

1. Sound Speed Calculation

Using the inputs of temperature, salinity, and depth, from the full water column profiles allowed the calculation of sound speed profiles for the full water column, as shown in Figure 20. The Woods Hole Oceanographic Institute Acoustic Group's MATLAB Oceanography Utilities function *soundspeed.m* was used to calculate the sound speed profiles. It can implement several sound speed equation sets. The algorithm used for ray tracing and absorption calculations was CML 1.0, the equations by Chen and Millero in 1977, as modified by Millero and Li in 1994. This algorithm is the U.S. Navy

Standard Sound Speed Algorithm and was used for this study. It was selected due to best performance in extensive testing and comparison with other algorithms. The current, effective January 26, 2010, Navy Standard is CML 1.1, which is the same equation set, but with expanded limits for the T, S, and D inputs (Moskal 2010). A comparison of sound speed profiles calculated by Mackenzie, 1960; Leroy et al. 2008; Del Grasso, 1974; and Chen-Millero-Li, 1994 is shown in Figure 21. The plot on the left was generated using the mean profiles for temperature and salinity from APLIS 2009. The plot on the right used all of the temperature and salinity profiles to calculate SSPs for all of the equation sets. It is important to note that while some data was obtained to 518m, 98% of the profiles were to a mean depth of 233m. This figure illustrates that there is little spread in the shallow water. While the profiles diverge below 1000m, there is less than 1.2m/s (0.08%) difference at 3500m. The same data, zoomed in to the upper 250m, is shown in Figure 22. This illustrates that given the T and S profiles obtained at APLIS 2009, the spread in the SSP in the upper ocean due to the selected algorithm is dominated by the spread in the SSP due to variability in the T and S profiles.

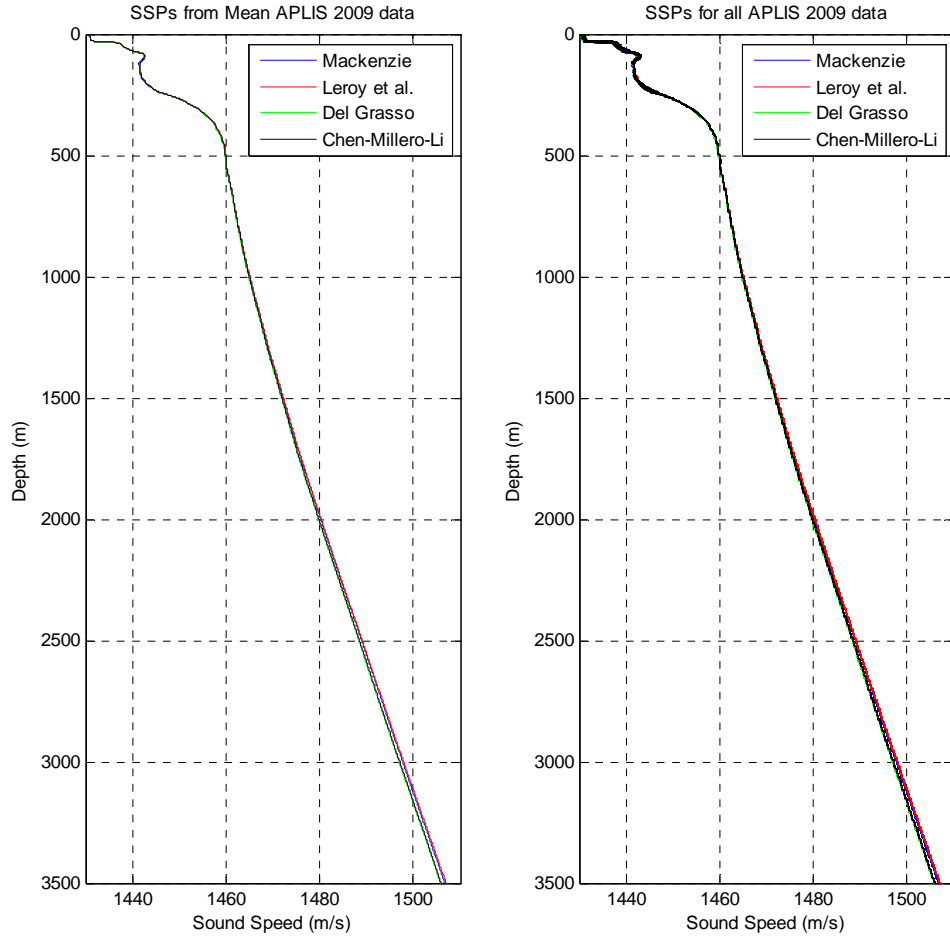


Figure 21. CML sound speed profile (SSP) in black compared to SSPs calculated by three other equation sets. The subplot on the left shows the SSPs calculated from the mean T and S. The subplot on the right shows all of the SSPs, for all of the equation sets, generated from all the T and S profiles.

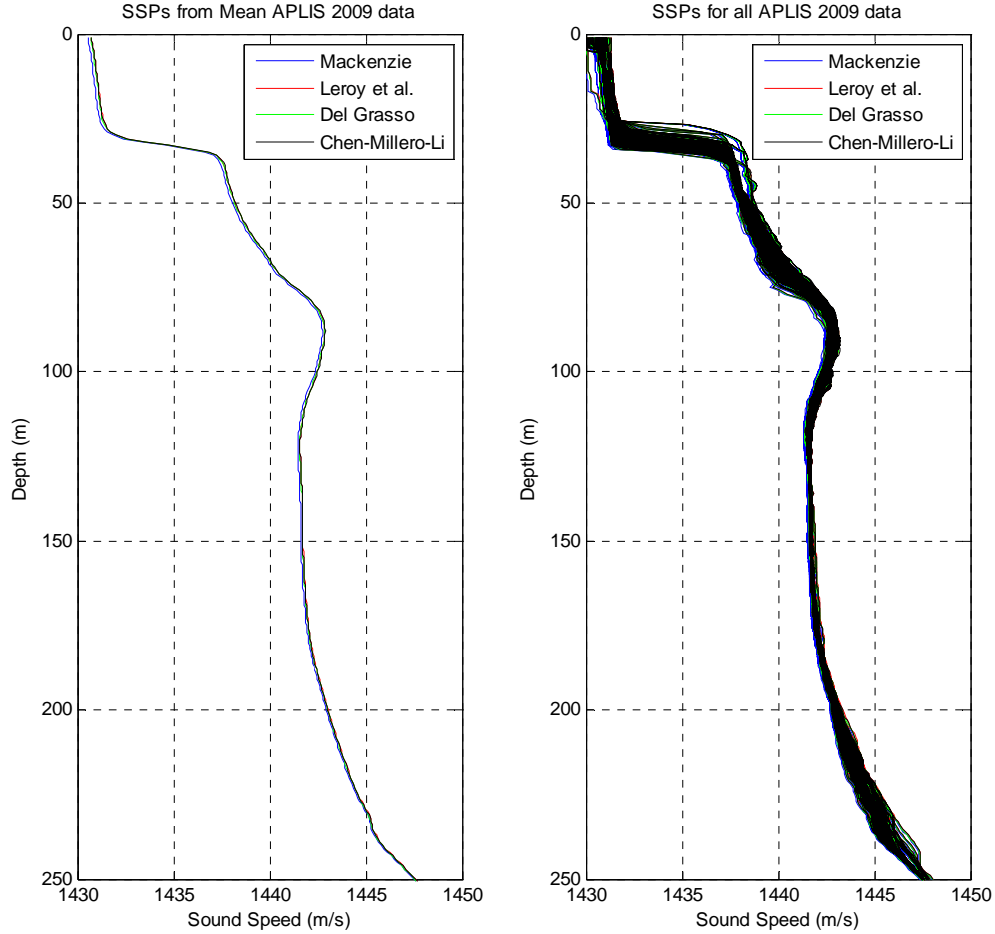


Figure 22. CML sound speed profile (SSP) in black compared to SSPs calculated by three other equation sets. The subplot on the left shows the SSPs calculated from the mean T and S. The subplot on the right shows the all of the SSPs, for all of the equation sets, generated from all the T and S profiles zoomed in to the upper 250m.

2. Sound Speed Profile Features

These figures highlight the strongly upward-refracting environment common to the Arctic Ocean and the fact that the environment is most strongly upward-refracting in the upper 400m. They also show the 100m deep sound channel centered at 150m. Using the mean SSP, the channel extended from 89m to 195m. The value of sound speed at the top of the channel is 1442.77m/s, and the sound speed minimum was 1441.61m/s at 123m. This channel was a key factor for ray propagation, particularly for cases when the sound source was located at 150m.

D. RAY MODEL

The ray model used was based on an Eigenray model developed by Prof. John Colosi and modified by Ben Jones from the Naval Postgraduate School. It assumes a perfectly reflecting surface and uses the image method to model ray surface reflections. In order to sample the possible eigenrays, sixty launch angles were selected for the model runs, from -15° to $+15^\circ$. Three source depths (50m, 100m, and 150m) were evaluated in order to study the effects of source depth location with respect to the sound speed channel and other structure in the upper ocean. For a given launch angle and source depth, the model determined the sound speed and sound speed gradient at that point. It then used the ordinary differential equation solver MATLAB function *ode45.m* to solve the eikonal equation, calculating the sound speed gradient and ray trajectory to determine the ray path in 5m intervals to a maximum range of 50km. The ray path consists of a depth for each horizontal range step of 5m, and then the Pythagorean Theorem determines the actual path length in that range step.

1. Inputs

a. Temperature and Salinity

The ray tracing was conducted for each profile of T and S. For each set of T and S profiles, the sound speed profile was determined using *soundspeed.m* as described in the previous section. The T and S profiles were also used for the calculation of absorption as will be discussed in the next section.

b. pH

The ray tracing is not dependent on pH. pH was included for its contribution to absorption and transmission loss, which was implemented as described above. pH structure is generally not considered in absorption calculations. When absorption is calculated with constant pH, a single value is used for the whole water column.

In order to study the effects of pH structure, as well as the effects of lowering pH due to CO₂ uptake, a pH effect switch was included in the transmission loss

portion of the ray model. To determine the effects of the pH structure, the model ran once for each case with pH assumed to be constant, and once with the measured pH profile for the whole water column.

2. Sound Speed Profile Smoothing

Since the profiles were processed with 1m bin widths, there were instances where the temperature and salinity profiles produced sharp corners in the sound speed profile. When these corners were too sharp, the differential equation solver broke down. Whether a profile would support processing with *ode45.m* was dependent on the source depth also. Fewer profiles ran into difficulties with a source at 150m. In order to have most of the profiles yield solutions while still preserving the structure and uniqueness of the profiles, the SSPs were low-pass filtered using a second order symmetric Butterworth digital filter using an OTG MATLAB routine *lpfilt.m*. This served to filter the SSP with cutoff frequency 0.1 m^{-1} , yielding a vertical resolution of 20m, and allowing 95% of the cases to yield ray traces.

3. Ray Traces

A sample sound speed profile is shown in Figure 23. A set of ray traces for this SSP is shown in Figure 24. For this figure, the source is at 150m, near the axis of the sound channel. This highlights the large number of interactions with the surface (ice), and shows no bottom interactions. The eight (of 60) rays with the narrowest launch angles (-1.78° to $+1.78^\circ$) remained trapped in the sound channel and had no interactions with the surface. For the same SSP, a set of ray traces with the source located at 100m, in the sound channel but near the sound speed maximum, is shown in Figure 25. The sound speed maximum for this profile actually occurs at 87m. In this case, only the four narrowest launch angle rays (-0.76° to $+0.76^\circ$) were trapped in the sound channel. For the same conditions, but with the source located above the sound channel at 50m, the ray traces are shown in Figure 26. This figure shows the much higher number of shallow-angle surface interactions. In this case, none of the rays was trapped in the sound channel.

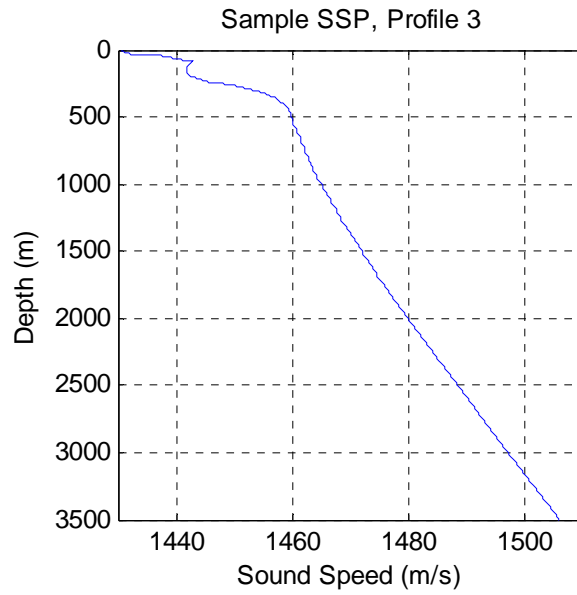


Figure 23. Sound speed profile that was used for the following ray traces.

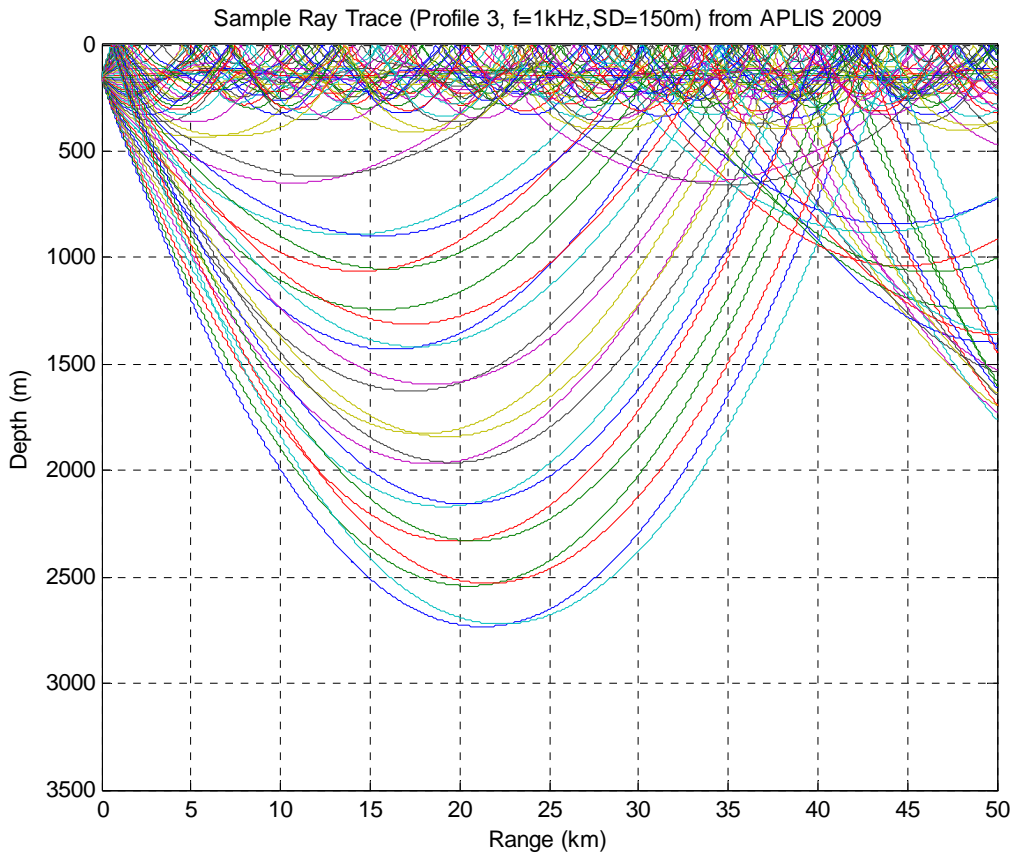


Figure 24. Set of ray traces for APLIS profile #3, source depth of 150m, and frequency of 1kHz. Note the density of rays in the sound channel.

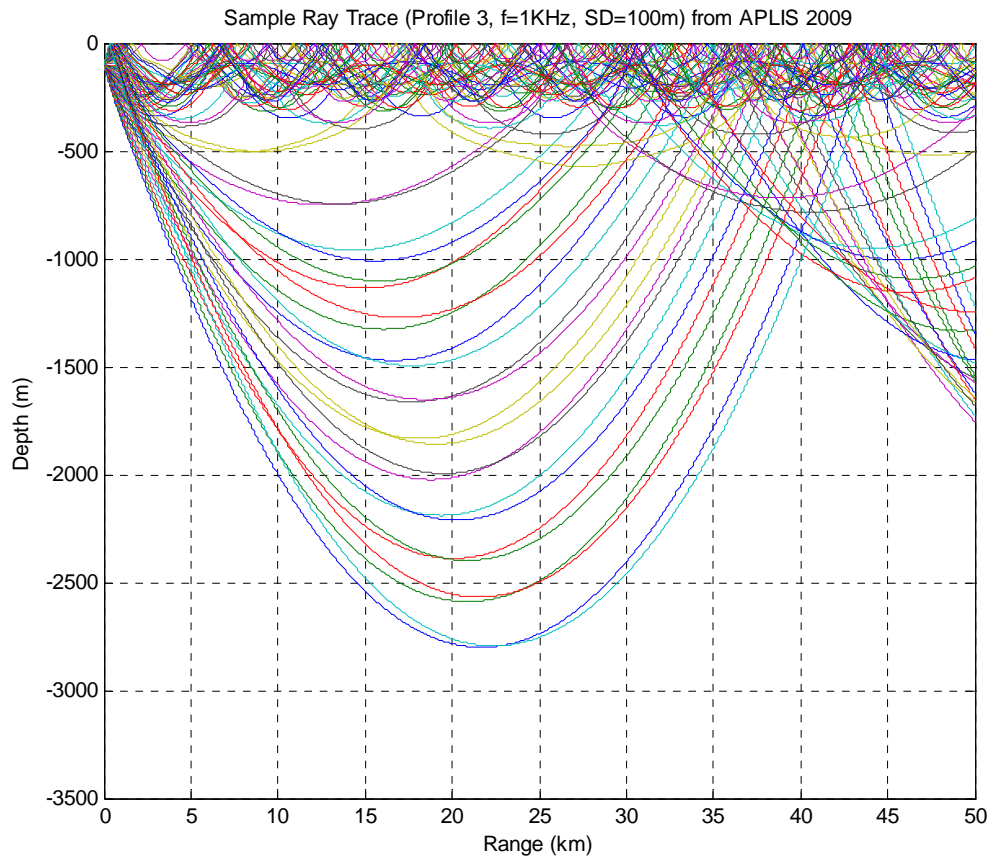


Figure 25. Set of ray traces for APLIS profile #3, source depth of 100m, and frequency of 1kHz. Note that there are fewer rays trapped in the sound channel, and a higher density of rays interacting with the surface.

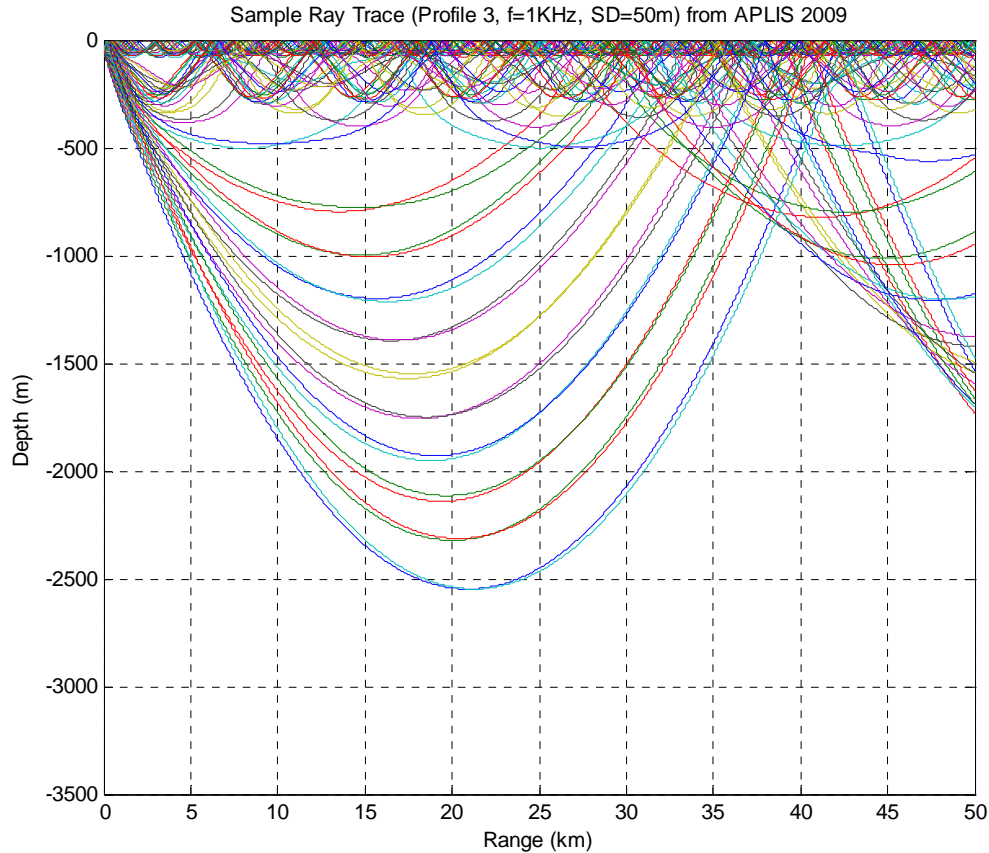


Figure 26. Set of ray traces for APLIS profile #3, source depth of 50m, and frequency of 1kHz. Note that there are no rays confined to the sound channel and the large number of surface interactions.

The rays launched from 50m, above the sound channel, have the largest number of interactions with the surface. They have an average of twice as many surface reflections compared to rays launched from 100m or 150m. This will factor significantly into the structure of the ice scatter-absorption contribution to transmission loss, which is discussed in the next section. The number of surface reflections versus launch angle, for each source depth, is shown in Figure 27. and shows the significance of the position with respect to the sound channel. A comparison of the difference in structure for very shallow angles is very interesting. The rays launched from 50m are not caught in the sound channel and have up to twice as many surface reflections, whereas some rays launched from 100m never exit the sound channel. An even greater number of rays launched from 150m remain trapped in the channel over the 50km range of study, and never interact with the surface.

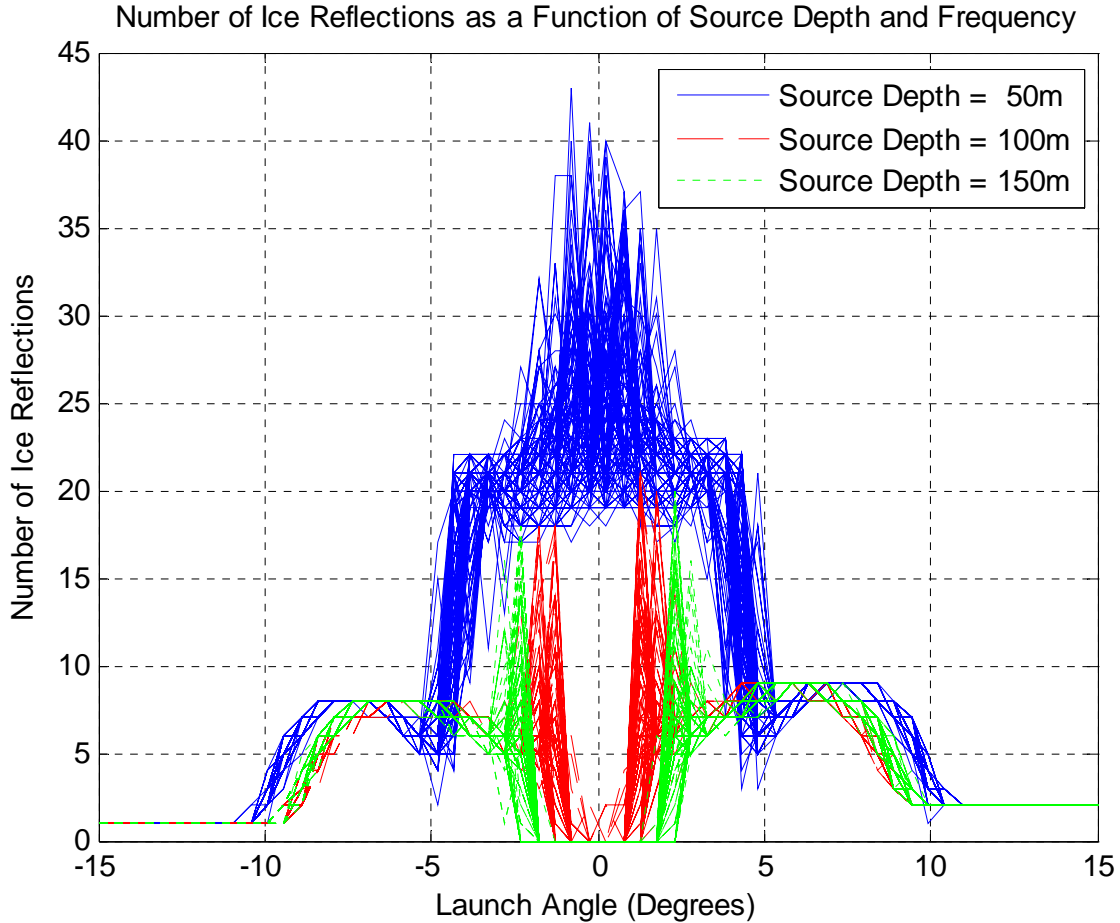


Figure 27. Number of reflections from the ice surface, as a function of frequency for the three source depths. Note how the negative launch angles tend to have one less reflection than the corresponding positive launch angles.

E. TRANSMISSION LOSS

Using ray theory allowed for a comparison of the relative magnitudes of transmission loss factors by keeping the effects of different contributors separate. This is an approximation for convenience because the focus of this thesis is the effects of environmental variability. This model determines the TL for a given path and is not a specific source-to-receiver transmission loss calculation that would include all possible paths and the consideration of the coherent vs. incoherent contributions to acoustic intensity.

A function was added to the ray model, which calculates the Francois-Garrison absorption coefficient at each step along the ray path (with the current profile-dependent

and depth-dependent values of T, S, and pH), then multiplies this coefficient by each corresponding step path length to give a TL due to absorption for that step. All the step absorption values are then summed to give a value for the absorption contribution to TL for that ray. Similarly, the geometrical spreading was calculated using the integral path length of each ray. The number of surface reflections was determined for each ray, and the ice scatter-absorption effect was calculated using a dB-loss-per-ice-reflection model from Diachok, 1976.

1. Spherical Spreading

The temperature and salinity profiles drive the sound speed profile. The gradient of the sound speed profile determines the curvature of the acoustic rays. The path length differences resulting from the structure of the sound speed profile lead to an angular dependence in the transmission loss. This path length difference and the associated TL are shown in Figure 28. There is also a dependence on the source depth location. The position of the sound source, with respect to the sound speed profile structure, influences how long the ray path will be, as shown in Figure 28. Note, that for the source at 50m, there is a relatively stable TL at narrow angles. This is because rays launched at very narrow angles follow similar paths. For comparison, the center plot shows data for a source depth of 100m. The depression in the center results from the rays with very narrow launch angles ($<0.8^\circ$) that are trapped in the sound channel and have shorter path lengths, never undergoing surface reflections, and correspondingly have lower TL_{geo} . This phenomenon is seen to a greater degree in the 150m source depth plot on the right. Since the source is located near the center of the sound channel, rays with launch angle twice as large ($<1.8^\circ$) as the 100m case are trapped in the sound channel. This will be important in the next section when comparing the 10kHz absorption curves at 150m. These angular confinements agree with Snell's Law, equation(5.4), requirements. c_z is the sound speed and θ_z is the angle of the ray trajectory, with respect to the horizontal, at depth z .

$$\frac{c_1}{\cos \theta_1} = \frac{c_2}{\cos \theta_2} \quad (5.4)$$

From Snell's Law and the mean sound speed profile from APLIS, rays launched from 100m at angles $<1.2^\circ$ will be trapped, and rays launched from 150m at angles $<2.2^\circ$ will be trapped in the sound channel.

Also interesting in this figure is the positive/negative launch angle effect. Rays launched with a positive angle tend to follow a path similar to the corresponding negative angle, but have an additional path length from traveling to the surface and back to the source depth. This is illustrated by the points on the left side of the curves being slightly lower than the corresponding points on the right of the curves in Figure 28. Similarly, the left-right difference due to the positive launch angles having one extra surface interaction was also seen in Figure 27.

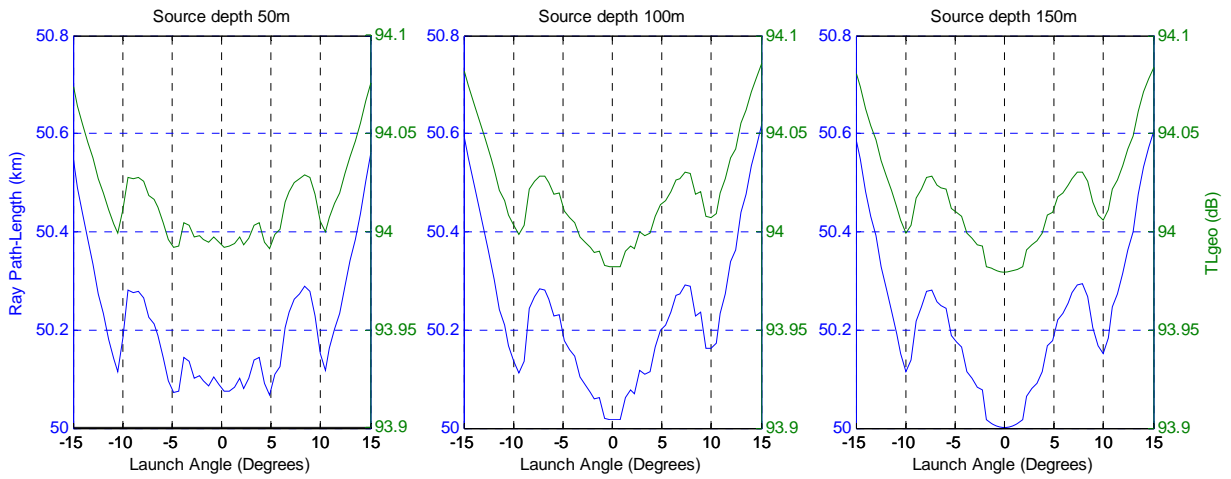


Figure 28. For one profile, plots of path length (blue) and spherical TL (green) for source depth of 50m (left), 100m (center), and 150m (right).

2. Absorption in Seawater

The absorption of acoustic energy in seawater is a function of T, S, pH, pressure, and frequency. The absorption profiles for the three frequencies studied are shown in Figure 29. This plot was created using the Francois-Garrison absorption equation (3.3), using mean T, S, and pH profiles. The mean T profile was obtained by averaging the T at each depth, for all the profiles from APLIS. The mean profiles for S and pH were calculated in the same way. The colored curves include the mean profiles as discussed. The black curves were developed using the mean T and S profiles, but with a single pH

value independent of depth. This value, $\text{pH}=7.98$, is the mean of all the pH data, for all depths. Since pH is typically not considered as a function of depth, this plot illustrates the differences in the absorption coefficient when pH is taken to be a single value (black curves), and when the measured pH is used (which has noticeable depth-dependence; color curves).

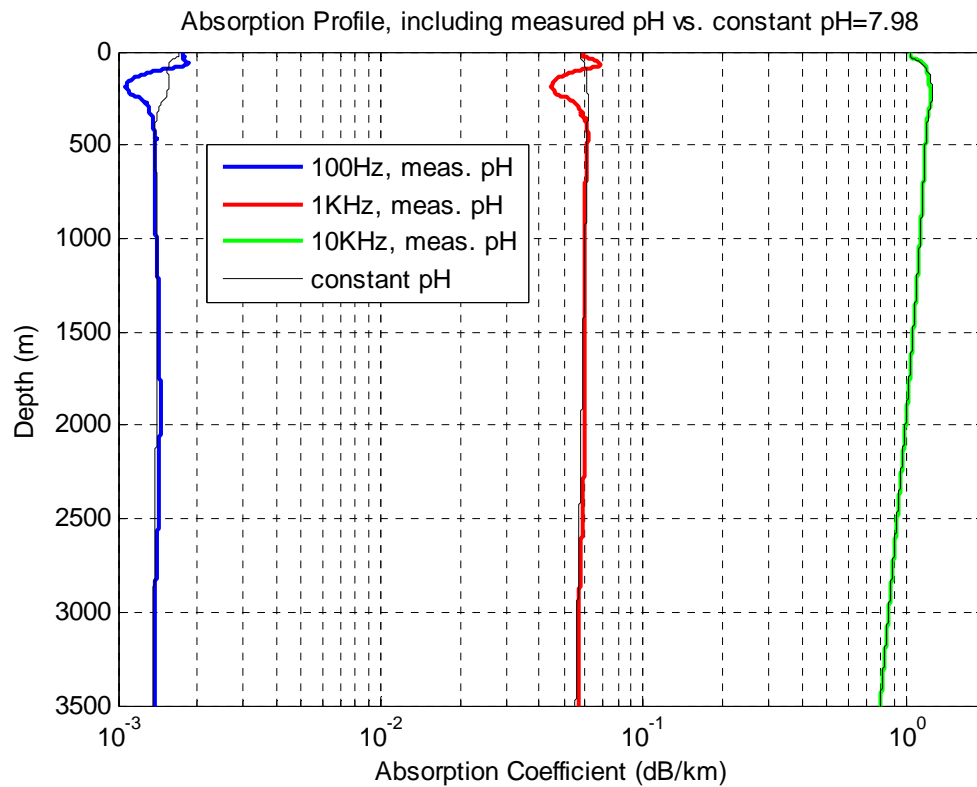


Figure 29. Absorption Profiles. Color curves include measured parameters. Black curves consider $\text{pH}=7.98$, a single value for all depths.

This figure is interesting because it shows how the relative effects of the T, S, pH and frequency influence the absorption as a function of depth. Locations of interest on these curves are summarized in Table 4.

		Constant pH			Measured pH		
		100Hz	1KHz	10KHz	100Hz	1KHz	10KHz
Depth (m)	Absorption Maximum	1	264	231	59	64	248
	Absorption Minimum (upper 500m)	455	3	3	189	185	3
	Absorption Minimum	3500	3500	3500	3500	3500	3500

Table 4. Absorption Profile points of interest. Note that the 100Hz and 1kHz curves have an absorption maximum above the sound channel and a local minimum in the channel, while the 10kHz curve has a maximum absorption coefficient below the channel and a local minimum near the surface.

The effects of pH structure are illustrated in the next six figures. The surface is assumed to be perfectly reflecting. Note that geometrical spreading accounts for about 94dB in these plots. The upper row represents model runs with a single pH value, independent of depth. The lower row includes the structure in the measured pH profiles. The columns represent source frequencies: the one on the left for 100Hz, the center column for 1kHz, and the column on the right for 10kHz. Note the scales on the left of each plot and that the overall magnitude difference is small when considering the effects of pH structure. The thin black curve is the mean of the TL data in each plot, and the dashed black line is ± 1 standard deviation from the mean. This description applies to Figure 30. through Figure 32. The transmission loss versus launch angle, for all the profiles at APLIS (i.e. excluding the radial survey), are shown for rays launched from 50m in Figure 30. Similar plots for source depth of 100m and 150m are shown in Figure 31 and 32.

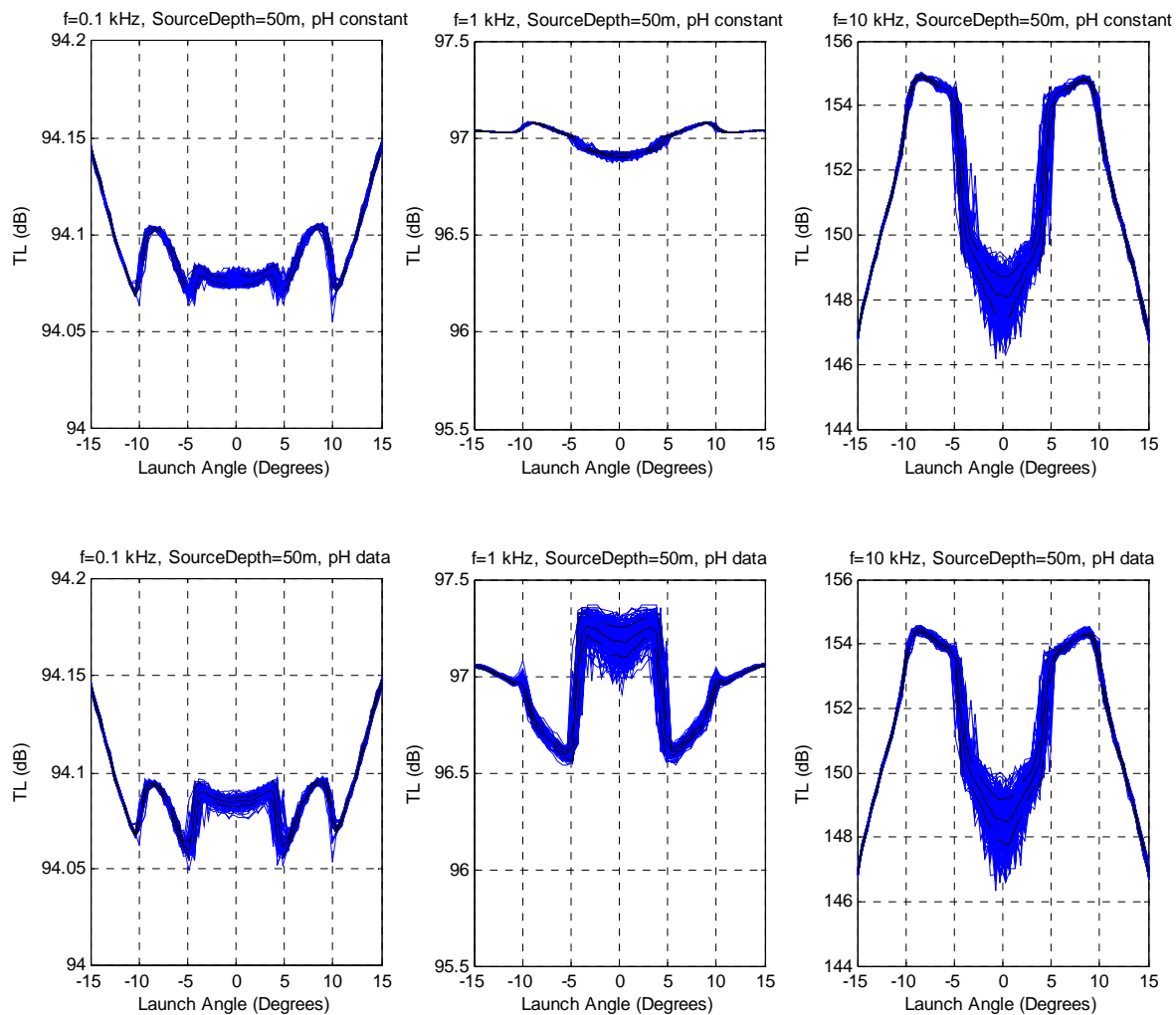


Figure 30. Transmission loss vs. Launch Angle. Source depth = 50m.

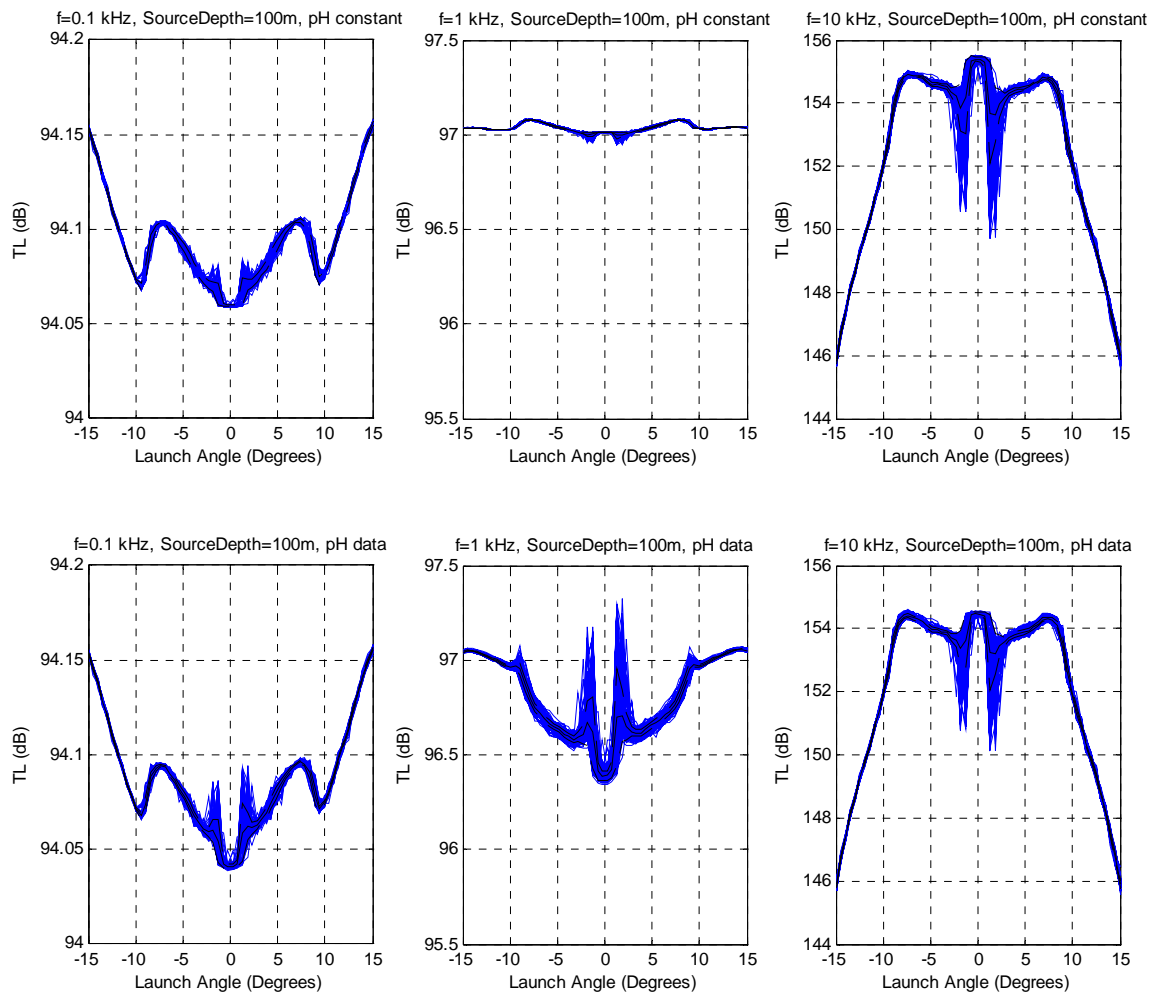


Figure 31. Transmission loss vs. Launch Angle. Source depth = 100m.

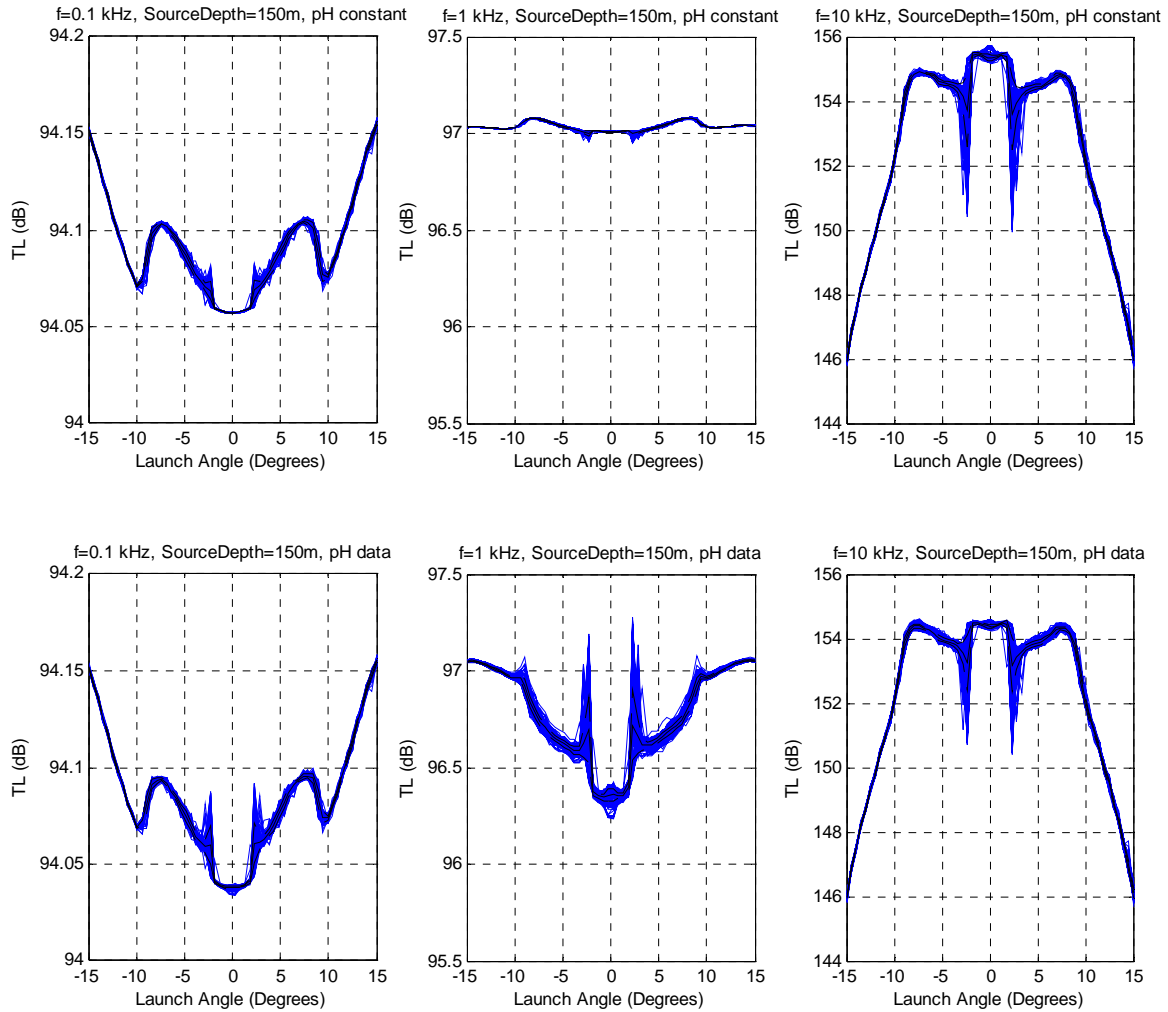


Figure 32. Transmission loss vs. Launch Angle. Source depth = 150m.

The top-left and top-middle plots of the TL vs. Angle plots are very similar to the corresponding plots showing the contribution of spherical spreading in Figure 28. Comparing the 50m source depth plots of Figure 30. to that of Figure 28. the 100Hz plot is about 1.07 dB higher, and the 1kHz plot is about 3 dB higher as a result of absorption. The 10kHz plot on the top-right of Figure 30 is significantly different from the TL due to spherical spreading. This results partially from the increased absorption at higher frequency. At medium (5° - 10°) launch angles; there is higher absorption due to more time spent in areas with a larger absorption coefficient, as shown in Figure 29. The narrow launch angles give more time close to the surface, where there is the absorption minimum for 10kHz. There is significant variability in the TL for narrow angles at this frequency

resulting from the structure of the absorption profile and the higher magnitude of the absorption coefficients at higher frequency. Also at 10kHz, the steep angles have the longest ray paths, but are near the lowest TL because they also spend more time in deeper waters where the absorption coefficients are again low. There is a similar structure noticeable in the 1kHz plot (in the top row, considering a single value for pH), but with a significantly lower amplitude, resulting from the lower TL at lower frequency. This effect would be opposite for 100Hz, since the pH constant absorption profile has a maximum at the surface, but this is negligible because the absorption is so small at low frequency.

These absorption profile effects are accentuated for Figures 31 and 32, when the sound source is located within the sound channel where the pH profile has more variability. This is illustrated by comparing the 50m source depth in Figure 30 with the 100m source depth in Figure 31. Again, the wider range of launch angles being trapped in the sound channel is shown for the 150m source depth plots of Figure 32. The absorption profile for 10kHz has a larger contribution to TL when the rays are near the sound channel, located near the maximum absorption coefficient at 248m in Figure 29. There is the opposite effect for the 100Hz and 1kHz plots, since they have minimum absorption coefficients near the sound channel axis, and the reduced TL for narrow angles is evident in the bottom-left and bottom-center plots in Figures 31 and 32.

In order to see more clearly the increased spread in the absorption component of TL as a result of pH profile structure, histograms were created which count the number of occurrences of a TL of a given magnitude. These are shown in Figures 33–35, for each source depth, frequency and pH case. These figures also illustrate the increased spread of absorption that the measured pH structure has on the different frequencies. The relative spread is much larger at 1kHz than the other frequencies, and that the effect at 100Hz is greater than that at 10kHz. At 10kHz, the most noticeable change is that the peak near 155 dB is lowered by about 1 dB when the measured pH profile is included, but the spread is similar.

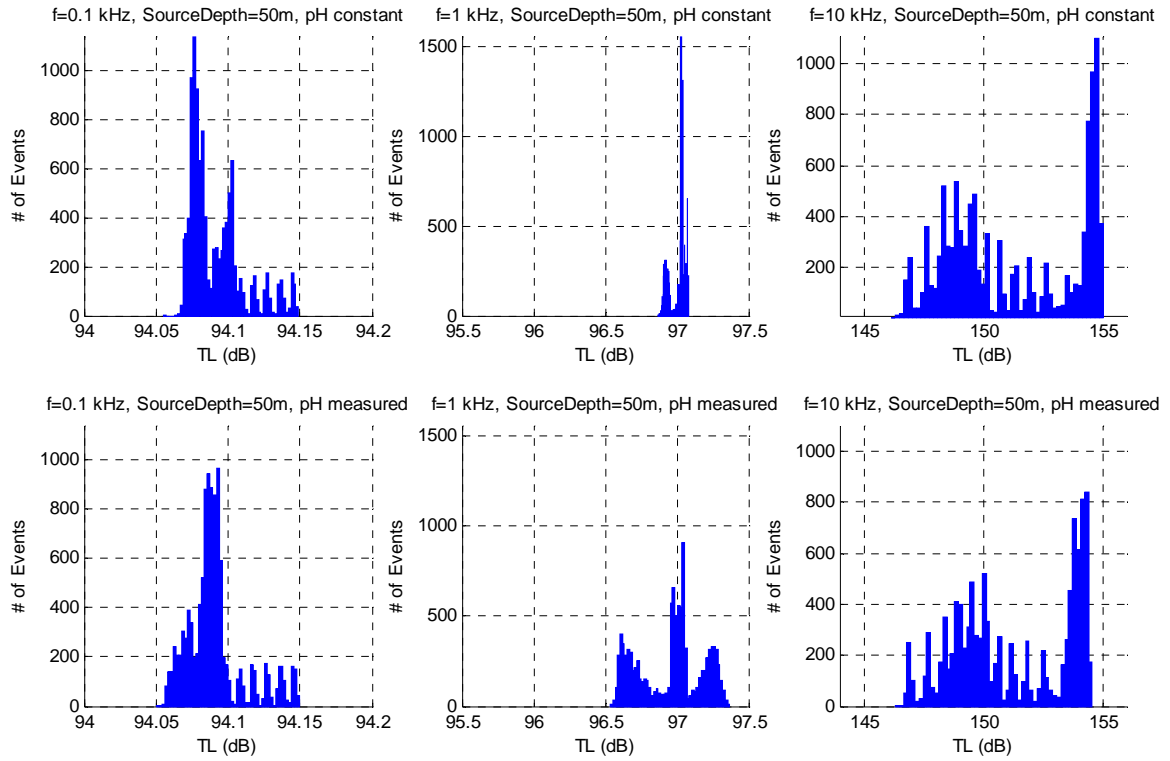


Figure 33. Histograms illustrating the spread of TL, for a perfectly reflecting surface, with Source Depth = 50m. These correspond to the plots of Figure 30.

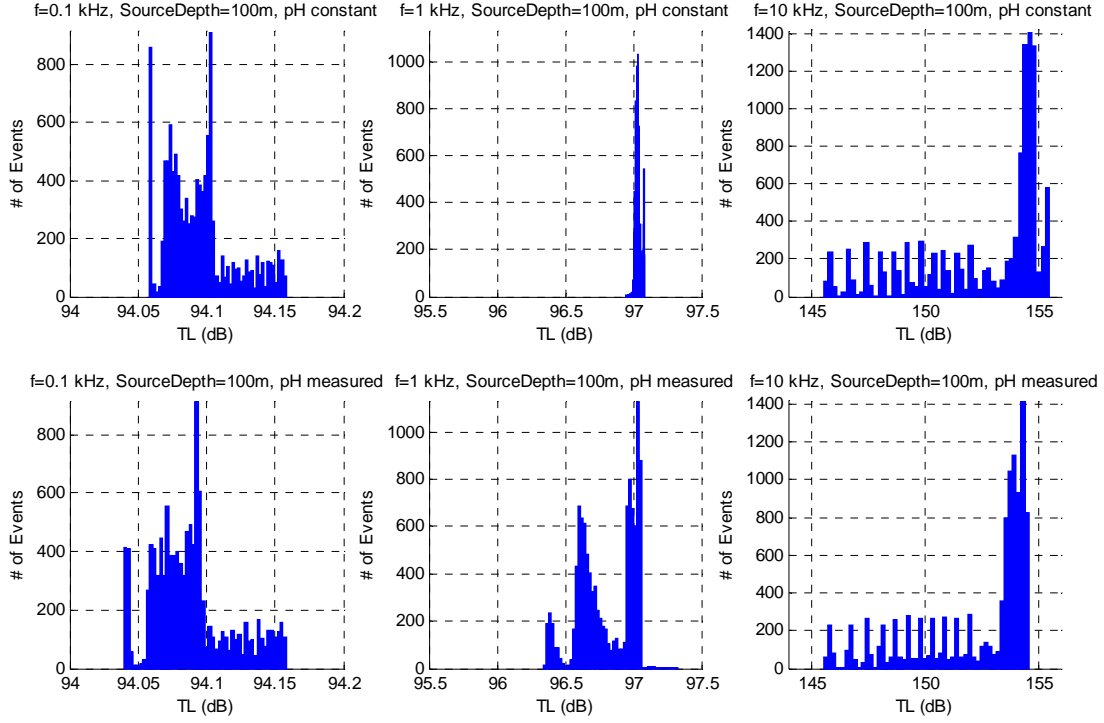


Figure 34. Histograms illustrating the spread of TL, for a perfectly reflecting surface, with Source Depth = 100m. These correspond to the plots of Figure 31.

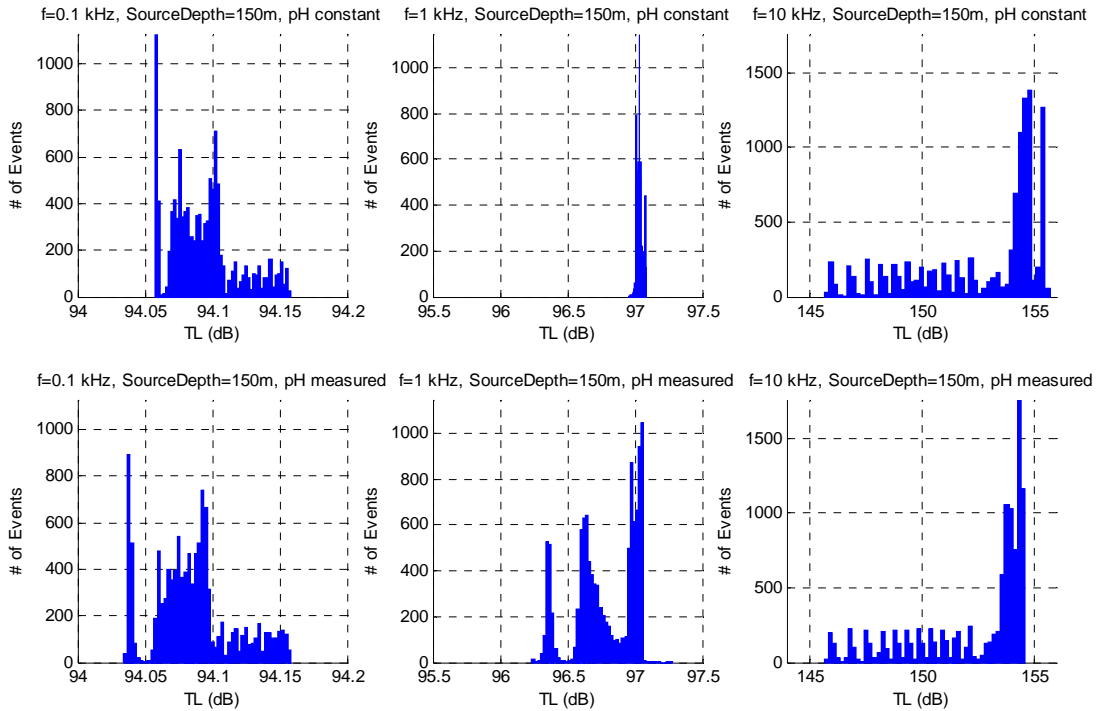


Figure 35. Histograms illustrating the spread of TL, for a perfectly reflecting surface, with Source Depth = 150m. These correspond to the plots of Figure 32.

The difference is small between the magnitude of absorption with measured pH and the absorption with a single pH value. While some spread between a profile with structure and a profile without structure was noticeable in the 100Hz and 10kHz cases, the largest relative change was seen in the 1kHz cases. The magnitude of the change is from about 0.1 dB spread for the single pH case to 0.7-0.8 dB for the measured pH case. One contribution to the spread, particularly at narrow angles is a large pH “channel” that is centered at 181m, and is about 160m deep. This leads to reduced absorption for rays traveling through this channel but is most apparent for narrow launch angle rays from source depths in the pH channel (100m and 150m). It is important to note that these cases still assume a perfectly reflecting surface. Scatter-absorption effects of the ice are investigated in the next section.

The largest relative change due to the pH structure occurs in the 1kHz plots, which is expected due to the relaxation frequency of boric acid being near 1kHz (dependent on T and S), and the absorption is sensitive to changes in T, S, and pH (from equation (3.6)). Note that in all these plots, spherical spreading accounts for about 94dB of transmission loss. Note also the scale for each of the plots. The scale for the 100Hz plots covers 0.2dB, while the 1kHz plots cover 2.0dB, and the 10kHz plots cover 12dB. This is a result of the exponential frequency dependence of absorption in seawater seen in equation(3.3).

3. Ice Scatter-Absorption Effects

a. SCICEX Data Set and Diachok Loss Model

Using data on keel depths and spatial distributions from a Science Ice Exercise (SCICEX) submarine cruise conducted in the Western Arctic Ocean in 1988 (NSIDC 1998), and equation (3.7) for dB lost per bounce from the ice (Diachok 1976), transmission loss due to ice scatter-absorption was calculated. It contained 407 measurements of keel draft and the distance to the next keel. This distance was inverted to develop a spatial frequency. The SCICEX data set defines a keel as having a draft equal to or exceeding 5m. As a result of the thinning of Arctic sea ice and the defining of a keel as drafting greater than 5m, this dataset from 1988 was expected to yield ice drafts

that are deeper than average for 2009. Since thinner ice can ridge more easily, the spatial distribution could be lower than average. It was assumed that these combined effects would mitigate each other and lead to order of magnitude accuracy. As stated in Chapter III, the Diachok high-frequency model used is independent of the specific frequency, provided that the product of the wavenumber and the mean keel draft is greater than unity, $kd > 1$, which is the case for all frequencies when using the SCICEX dataset.

Each time a ray was to interact with the ice, a matched set of keel draft (d) and spatial frequency (N) was selected at random from the measured distribution, the incident angle was determined, and the reflectivity was calculated following equation(3.7). It was important to calculate N and d from the same random draw since the spatial frequency of ridges is related to the draft, specifically that larger ridges tend to have larger distances between them, as shown in Figure 36. As an example, reflectivity as a function of incident angle is plotted for keel spatial frequency $N=9.5\text{km}^{-1}$ and keel draft $d=4.3\text{m}$ in Figure 37. Also shown in this figure is the SCICEX reflectivity curve calculated from the mean keel draft ($d=8.5\text{m}$), and the mean spatial frequency of keels with draft between 8m and 9m. This resulted in $N=11.8\text{km}^{-1}$. Figure 37 shows that the data set from SCICEX results in greater loss per ice reflection than Diachok's example parameters. It is also evident from equation(3.7) and this figure that large reflection losses are generated near 6° .

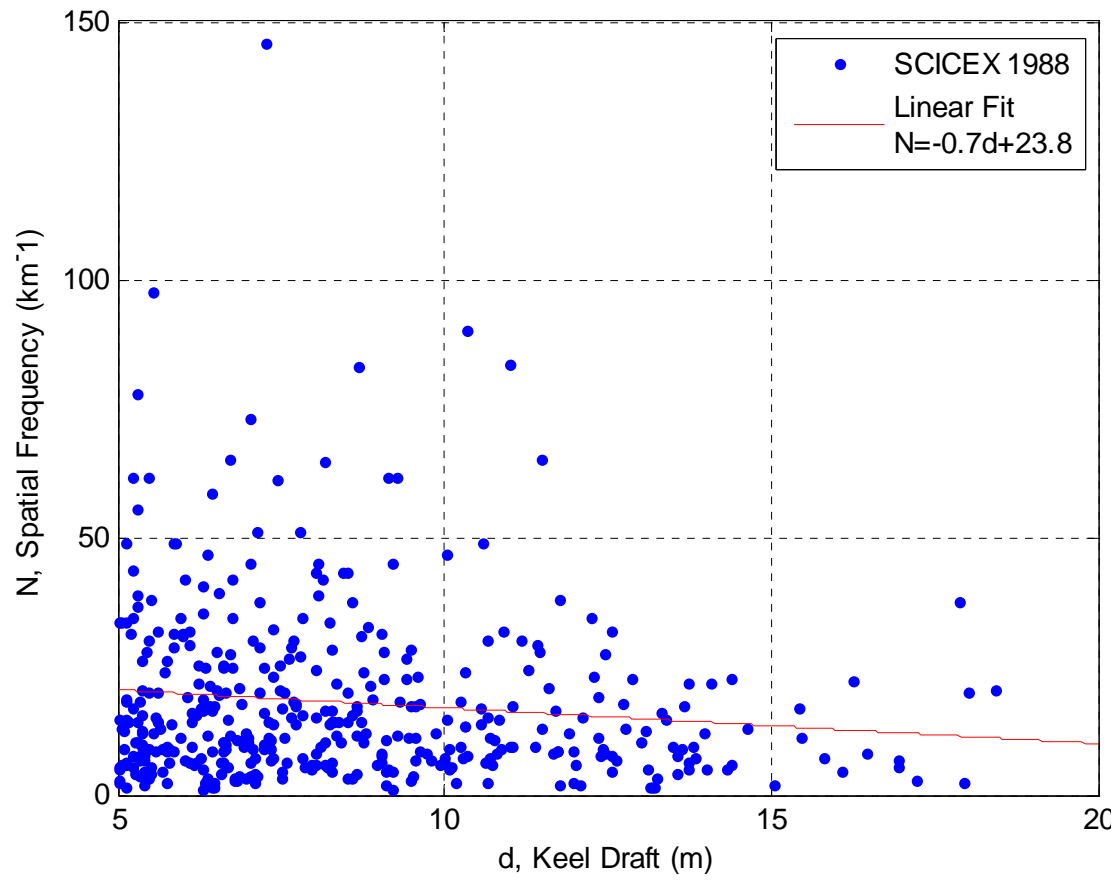


Figure 36. Spatial Frequency vs. Keel Draft for SCICEX 1988 data. This figure shows that the spatial frequency is higher for smaller keels, and lower for larger keels.

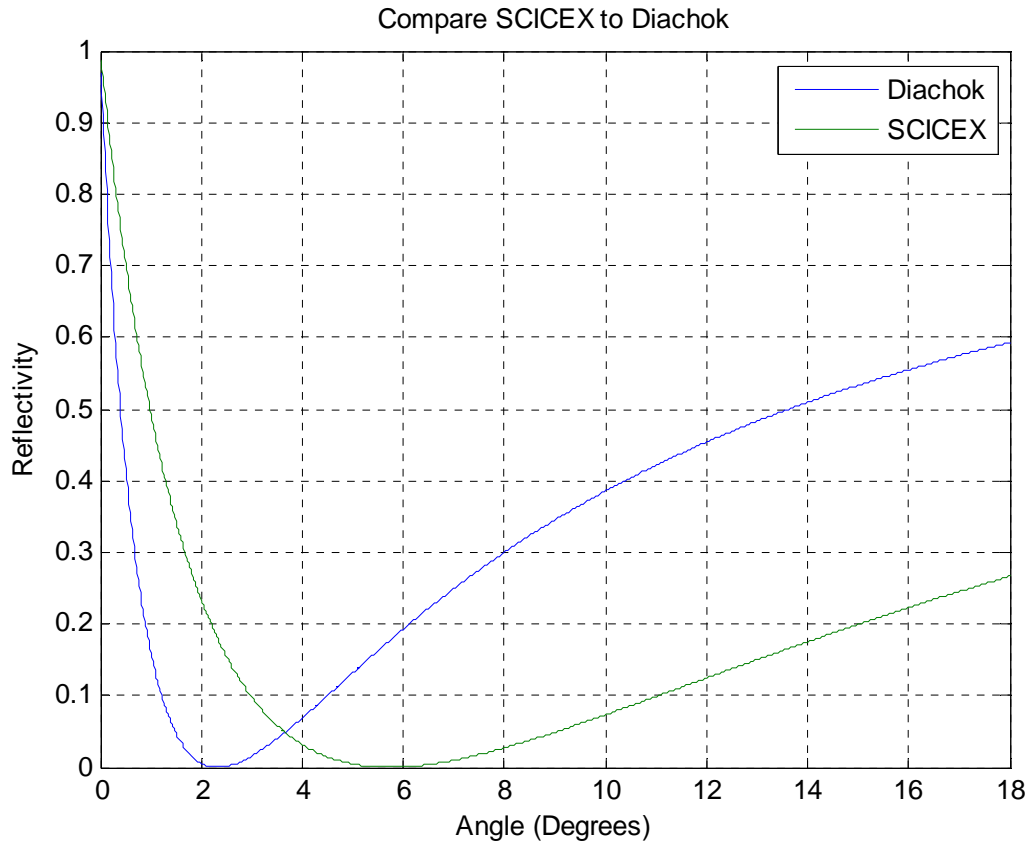


Figure 37. Comparison of Reflectivity vs. Angle for Diachok's $N=9.5 \text{ km}^{-1}$ and $d=4.3\text{m}$, and the mean ice draft data from SCICEX, $N=11.8 \text{ km}^{-1}$ and $d=8.5\text{m}$.

Incident angles that were observed in this study from the source depths and sound speed profiles are shown in Figure 38. The majority of incident angles have very low reflectivity and correspond to high TL due to ice scatter-absorption. These low incident angles result from narrow launch angles. The observations in Figure 38 agree well with Snell's Law, which, for the mean SSP from APLIS dictates a possible range of incident angles from 6° - 16° for 50m source depth, and about 7° - 17° for 100m and 150m source depths.

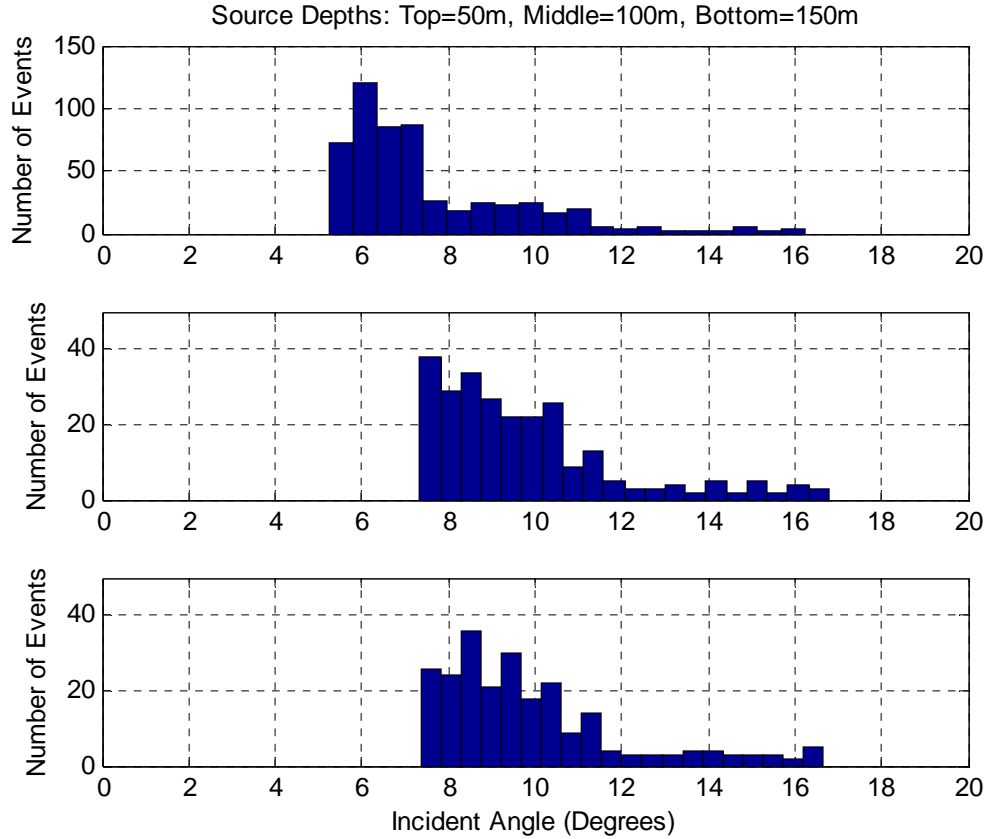


Figure 38. Observations of angles for rays when incident upon the ice. For the top plot, Source Depth = 50m. For the center plot, Source Depth = 100m. For the bottom plot, Source Depth = 150m. Note that the scale on the left is different for the 50m case because of the much higher number of surface reflections.

b. TL Results with Ice Scatter-Absorption Included

The following six TL vs. Launch Angle figures have the same format as the previous six. Each figure represents rays launched from one source depth. The left-hand column is for a frequency of 100Hz, the center column is for a frequency of 1kHz, and the right-hand column is for a frequency of 10kHz. The top row considers pH to be constant, and the bottom row uses the measured pH profiles when calculating absorption. The heavy black curve is the mean of the TL when ice effects are considered, and the heavy dashed black curves are ± 1 standard deviation from the mean. The red curves show the total TL, being the sum contributions of spherical spreading, absorption, and ice scatter-absorption. The blue curves contain the same data as the corresponding figures

when the surface was assumed to be perfectly reflecting (Figures 30-32). The effects of the interactions with the ice now dwarf the blue curves.

These TL vs. Angle plots and the histograms that follow are also useful to see that the ice effect does not follow a Gaussian distribution. This was as expected, based on the way the SCICEX data set defined a keel as a draft exceeding 5m.

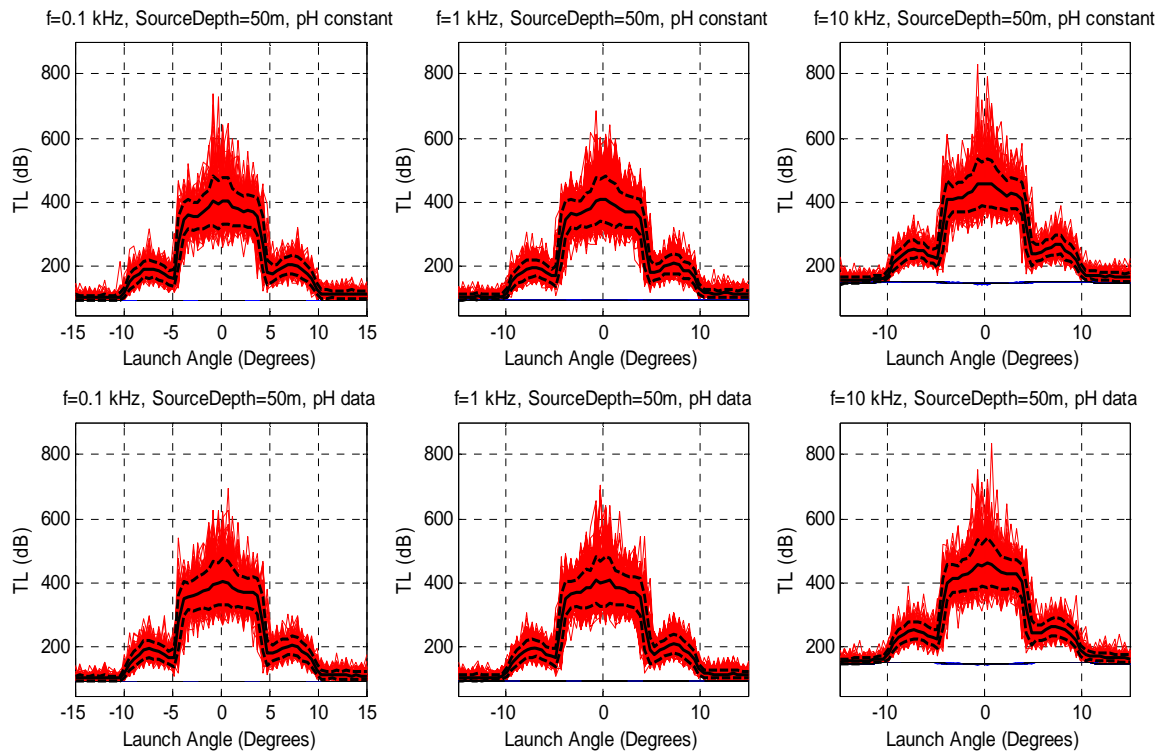


Figure 39. Transmission Loss vs. Launch Angle with ice scatter-absorption effects included. Source Depth = 50m. The blue curves which are barely visible, contain the same data as in Figure 30. Note the scale on the vertical axis, which shows the huge increase in TL in dB due to ice effects.

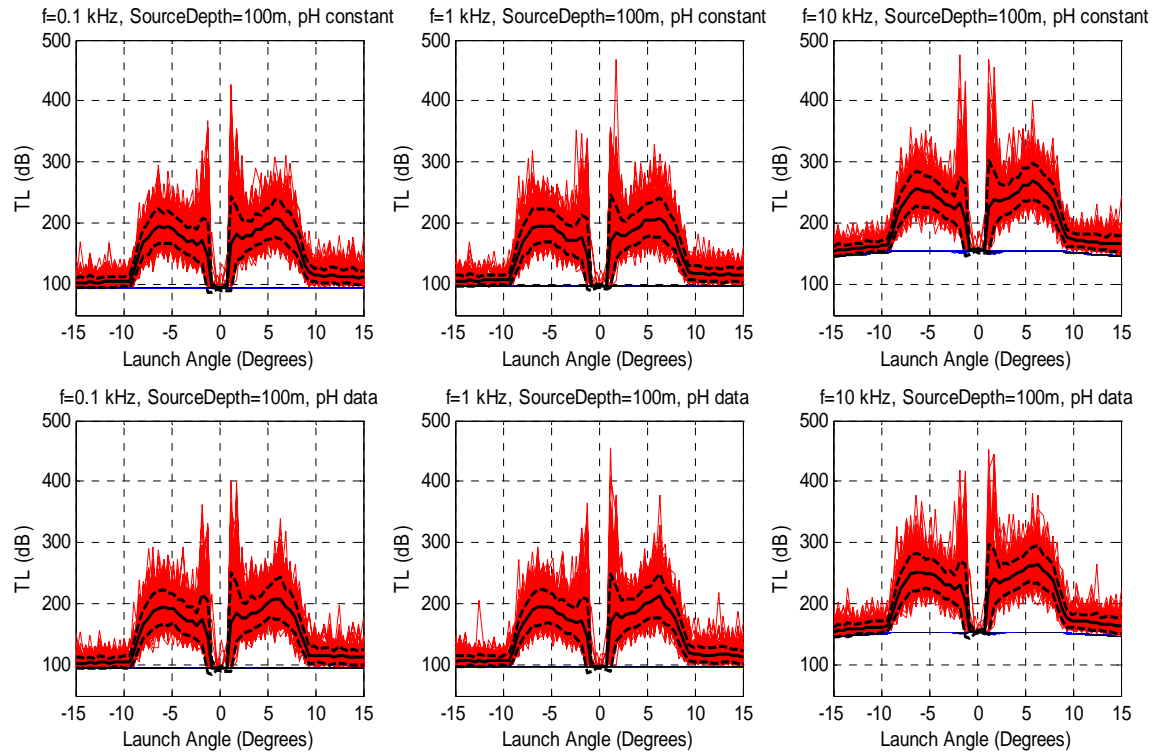


Figure 40. Transmission Loss vs. Launch Angle with ice scatter-absorption effects included. Source Depth = 100m. Note the scale on the vertical axis, compared to the previous figure, and the effects of rays getting confined to the sound channel.

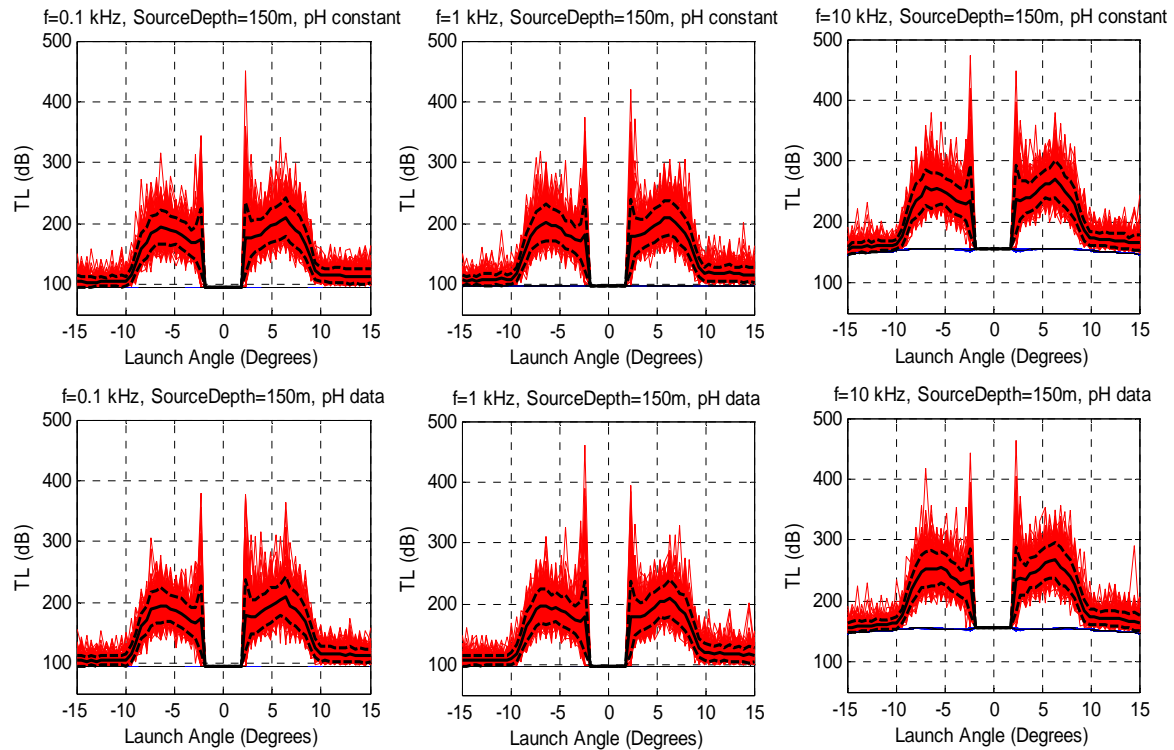


Figure 41. Transmission Loss vs. Launch Angle with ice scatter-absorption effects included. Source Depth = 150m.

As in subsection **two.** above, where histograms were used to illustrate the distribution of TL for the different cases, histograms of the TL data in Figures 39–41 are shown in Figures 42–44. These histograms show again that the predicted spread of TL for paths that involve ice interactions dominates what little variability was present due to pH considerations.

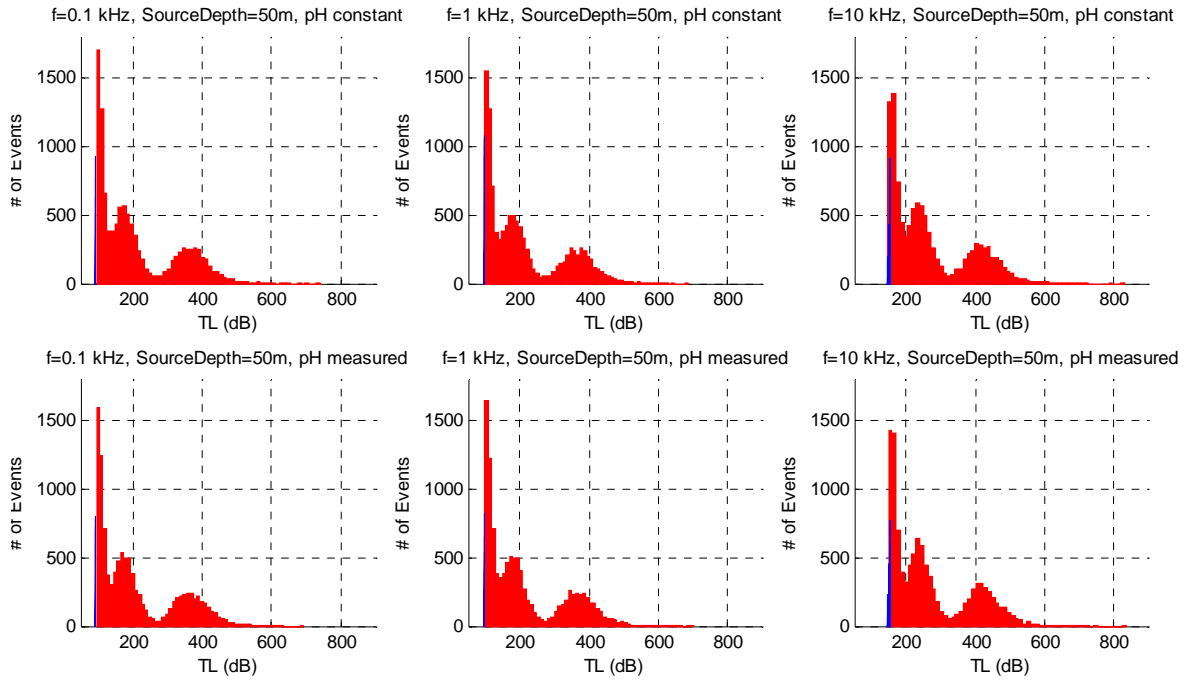


Figure 42. Histograms illustrating the spread of TL when ice scatter-absorption is included. Source Depth = 50m. These histograms correspond to the plots in Figure 39.

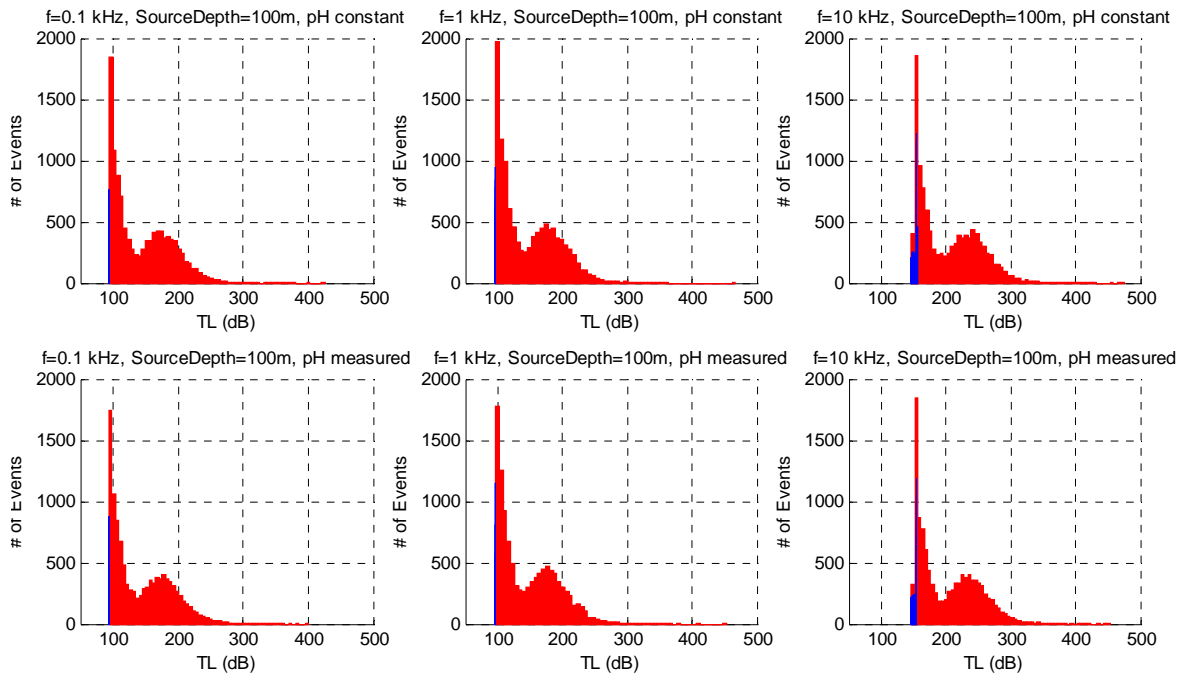


Figure 43. Histograms illustrating the spread of TL when ice scatter-absorption is included. Source Depth = 100m. These histograms correspond to the plots in Figure 40.

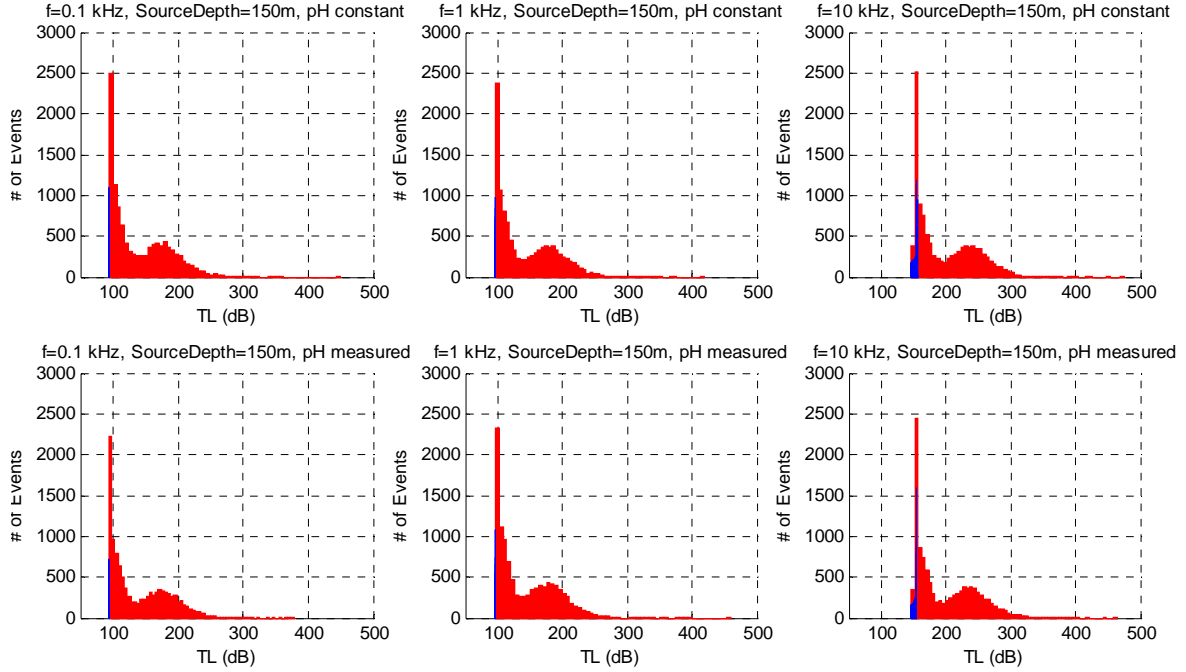


Figure 44. Histograms illustrating the spread of TL when ice scatter-absorption is included. Source Depth = 150m. These histograms correspond to the plots in Figure 41.

4. Relative Magnitude of Effects

When the surface was considered to be perfectly reflecting, the largest contribution to the magnitude of transmission loss, over the 50km studied and the frequencies considered, was the spherical geometrical spreading. It accounted for 94dB/50km. Being only dependent on range; the only variability was due to very small differences in ray path length. Over 50km, the maximum increase in path-length is about 500m, and occurs with the steepest launch angles. This results in an increase in TL of only 0.09dB, one of the smallest sources of variability. Of course, it is possible that a more sophisticated model for geometrical transmission loss would show higher variability. In particular, the variability due to uncertainty in the exact SSP would be interesting to quantify. For 1kHz and 10kHz, the next largest contribution to TL is the absorption in the water column. At 1kHz, this adds about 3dB to TL when a single depth-independent pH value is used, and adds 2-3dB when the measured pH structure is included. The variability in TL due to absorption at 1kHz is low, however, at ± 0.5 dB. At

10kHz, absorption contributes 50-62dB of TL, depending on launch angle/ray path. The pH effect at this frequency is up to 1 dB, but this is dominated by the variability due to launch angle. At 100Hz, the absorption contribution to TL is very small (0.1dB), and the variability is also very small (<0.1dB).

The TL due to interactions with the ice, using the Diachok model, is not frequency dependent. Therefore, the magnitude of the predicted TL contribution due to ice effects is the same for all frequencies. The largest variations are seen when comparing the TL due to ice for different source depths. For example, Figure 39 shows extremely high TL values due to high numbers of surface interactions. In Figures 40 and 41, the rays from narrow launch angles have reduced ice interactions due to the effects of the sound channel, or having no ice interactions as a result of being completely trapped in the sound channel.

Developed from a dB/bounce model that factors in the spatial frequency of ice keels and the distribution of keel drafts, the variability in under-ice structure is the largest contributor to the variability in transmission loss for all frequency and source depth cases. The loss due to the ice is also affected by the incident angle. In this upward refracting environment, small incident angles result from shallow source depths and/or narrow launch angles. The combination of keel distribution and incident angles plays heavily into the amount of loss due to the ice scatter-absorption, as shown in Figure 37.

An important point to remember is that despite the model output of hundreds of dB of TL due to ice effects, a ray that accumulates a very high TL is essentially attenuated beyond detection at that range. For a source of any frequency at 50m, TL due to ice interactions increases rapidly corresponding to many surface bounces. If a source is shallow and close to the ice, steep angles and relatively smooth ice are needed for meaningful amounts of energy to propagate.

For a 10kHz signal, the cumulative TL is very high regardless of source depth. Only the rays that are trapped in the sound channel have a realistic chance to contribute at 50km. The window is very narrow ($\pm 1.2^\circ$) for a source at 100m, but for a source at

150m, the range of angles that can be trapped is greater ($\pm 2.2^\circ$) and presumably the corresponding contribution at a range of 50km would be greater.

As the frequency of a signal goes down, the overall TL goes down as a function of the frequency-dependent absorption. For 1kHz and 100Hz sources, steep launch angles reduce the effects of ice scatter-absorption, but the lowest TL results from rays confined to the sound channel. In this narrow region where there is no loss due to ice interactions, the variability due to consideration of pH can be seen the center and left plots of Figure 31 and 32. In this case, a difference of up to 1 dB can be seen based on pH vertical structure and profile variability.

F. RADIAL SURVEY

It had been assumed that the sound speed profile (SSP) changes only slowly as a function of radial distance, and that the SSPs could be considered range-independent. The radial survey studied this hypothesis to test the validity of the assumption.

1. Data

For the radial survey, two profiles (one down, one up) were obtained at each of 5 locations over 50km to the northeast. Two additional profiles were obtained upon return to the camp (the 0th radial) to provide a maximum spatial separation with minimum temporal separation. Due to errors with the CTD, most probably freeze-up of the conductivity cell, three down-profiles were discarded. The temperature and salinity for these profiles were erroneous until halfway to 230m, where they correlated well with the corresponding up-profiles. Including the 0th radial, there were nine good profiles with which to investigate radial dependence on sound speed profile. The SSPs generated from these profiles are shown in Figure 45.

2. Range Dependence

While the general structure of the sound speed profiles is as expected, there is more variability than anticipated. Also shown in Figure 45 is the mean and standard deviation from the time series, which consisted of 124 profiles over 36 hours. During this time, the camp drifted south 122m. This figure illustrates that there was more variability

over 7.3 hours and 47km, than over 36 hours and 0.1km, suggesting that spatial variability at this scale dominates, and that the validity of the range-independence assumption should be investigated further.

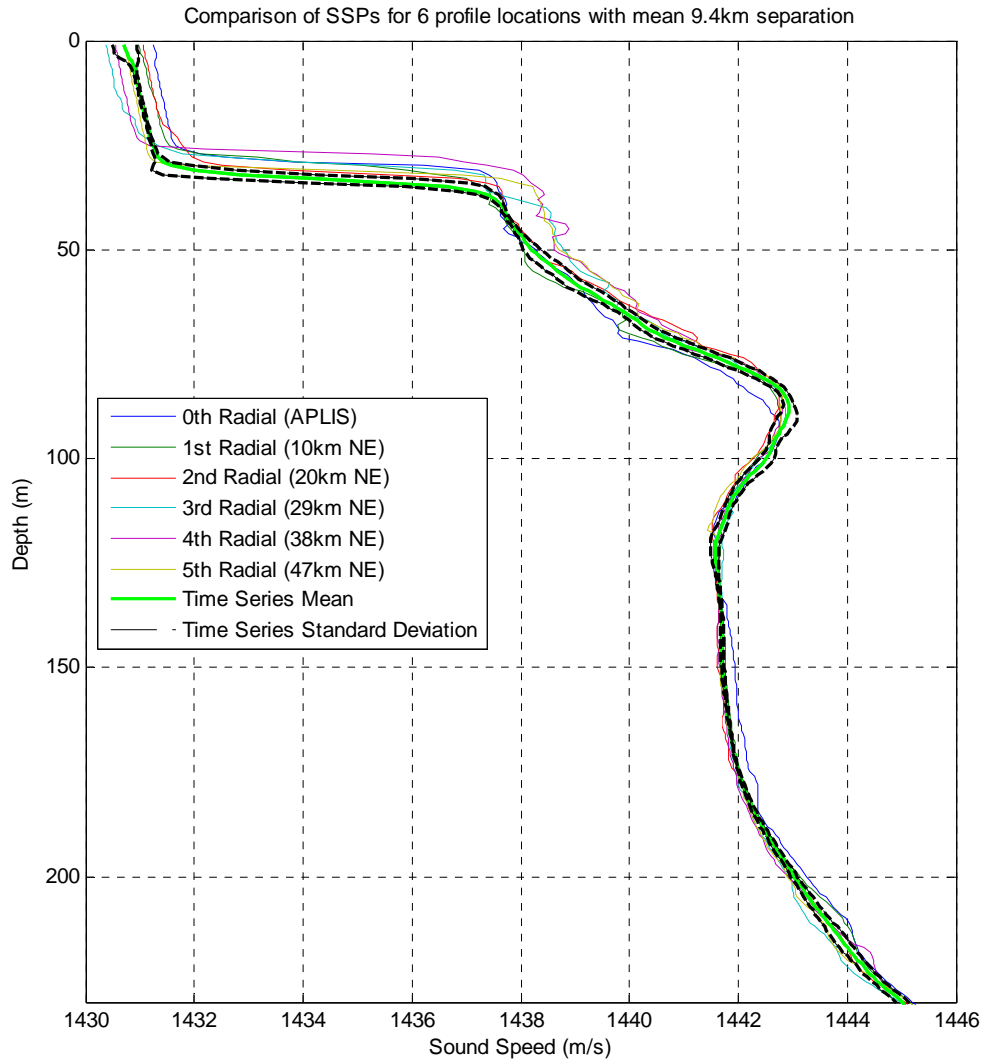


Figure 45. Sound speed profiles for the radial survey. The light green curve shows the mean of the SSPs from 124 profiles from the 36-hour time series. The black dashed curves show ± 1 standard deviation from the mean. This figure shows that the variability in sound speed profile in a few hours over 47km is greater than the variability in the SSP over 36 hours and drifting 0.1km.

THIS PAGE INTENTIONALLY LEFT BLANK

VI. CONCLUSIONS AND RECOMMENDATIONS

A. SUMMARY OF RESULTS

T, S, pH, and sound speed profiles were input to a ray model that was run for several scenarios, varying source depth and frequency. The effects of pH variability were investigated by running the model with a constant, depth independent pH for the whole water column and comparing that to model runs with the measured pH in the upper ocean. Another factor of variability considered was the effects of ice interactions. The relative smoothness or roughness of the ice depends on the frequency of sound in question. In the Diachok model, the reflectivity is considered to be independent of frequency, provided that the frequency and the mean keel draft are large enough ($kd > 1$). Diachok's model determined reflection losses as a function of incident angle, and mean keel draft and mean spatial distribution. For this thesis, a dataset of keel drafts and spacing was randomly sampled in order to provide increased accuracy of the Diachok model. These effects are accounted for with an equation giving a dB lost per bounce from the ice. The ray trace/absorption model was used to look at the fine-scale variability in the measured parameters and the effects on transmission loss for individual rays over a range of 50km. Due to model limitations, the geometrical transmission loss for each path was approximated as spherical spreading over the path length.

1. No Ice Effects / Perfectly Reflecting Surface

For a source of 100Hz, there was less than 0.1dB variability (0.05dB below the mean to 0.05dB above the mean) in TL over 50km, for all calculated sound speed profiles, regardless of pH effects or source depth of 50m, 100m, or 150m.

For a source at 1kHz, when pH is held constant, there is less than 0.1dB variability in TL regardless of source depth. When the variable pH from the data is considered, there is approximately 1dB of variability. Sound that leaves the source at steep angles has less interaction with this variable pH field and consequently lower variability. At shallower angles, and for a source depth above the sound channel (50m), there is much more variability.

For a source at 10kHz, there is up to 5dB of variability in TL resulting from the structure of the T, S, and sound speed profiles. The difference between considering pH effects or not yields less than 2dB of variability, and is seen primarily in narrow angles, as was the case for the 1kHz source.

2. Ice Scatter-Absorption Included

Considering acoustic energy along the ray path lost in each interaction with the ice, using Diachok's 1976 equation, there was the most significant effect when the source was at 50m. By a range of 50km, essentially all of the rays were attenuated beyond detection. This was expected in the strongly upward-refracting environment, and especially since the sound source above the sound channel has many more surface interactions than for the cases when the source is in the channel. Similarly, the effect of including ice scatter-absorption is strongest for small angles that generally have more surface interactions. The only rays expected to contribute significantly at 50km range are those from a narrow angle, for a source of frequency less than about 1kHz, located in the sound channel. As the frequency goes down below about 70Hz for the SCICEX keel draft data ($kd < 1$), Diachok's high-frequency equation no longer applies. Similarly, for a source at 100Hz, the mean keel draft would have to be shallower than 2.3m in order for Diachok's low-frequency equation to apply. This relation could become applicable because as the ice gets thinner, and the mean keel draft depth gets smaller. For a given frequency, smoother ice reflects sound with less loss, and so thinner ice and shallower ice ridges can lead to reduced contribution of ice scatter-absorption at increased frequencies.

B. RECOMMENDATIONS

1. pH and SSP

Arctic maritime activity will increase corresponding to the decline in sea ice coverage. Increased CO₂ in the atmosphere, combined with reduced ice cover, will lead to an increased uptake of CO₂ in the upper Arctic Ocean. This will contribute to a lowering of pH, primarily in the upper ocean. Absorption of acoustic energy will increase

with this change in pH, but the effect is small. Uncertainty in transmission loss due to sea ice scatter-absorption is expected to dominate the uncertainty due to the changing pH structure.

As a result of this study, continuous pH profiling is deemed unnecessary for acoustical applications given the small magnitude of pH fluctuations embedded in large sensor drifts and the operational complexity of maintaining accurate calibration of the sensors. Specifically the operational monitoring of pH by submarines is discouraged. Above 1kHz, the variability in TL due to SSP variability is expected to exceed that of pH effects, especially in the near-surface environment. Continued study of temperature and salinity variability in the upper Arctic Ocean is recommended.

As seen in Table 1. and Figures 30–35 and 39–44, the uncertainty in pH effects on absorption are small and dominated by the uncertainty due to ice effects. For frequencies around 1kHz, the effects could possibly be significant in ice-free environments where the variability in transmission loss due to the uncertainty in SSP is very small. Study of the effects of pH in realistic ice-free open-ocean scenarios could be beneficial if the uncertainty in transmission loss due to other factors is sufficiently low.

Since the pH effects have been shown to be small, and large-scale pH changes are projected to take place over decades, it would be more feasible, but nearly as beneficial, to incorporate data from only periodic pH profiling into transmission loss models. Because of the slow process of air-ocean gas exchange and the low vertical diffusivity, infrequent monitoring is possible, but due to the large differences in summer and winter surface boundary conditions, determination of the structure of the pH profile on a seasonal basis is recommended.

An unresolved issue is the pH scale in use by different groups. Since there is not a standard pH scale between acousticians and chemical oceanographers, there can be an offset between the pH in the absorption equations and the pH measured by chemists, even though this offset would not affect the structure of the pH profile.

Because of the issue with the temporal drift of the pH sensor, the manufacturer is assessing the sensor in order to determine possible corrections to the measured pH. Once this is completed, the model scenarios could be repeated and reevaluated.

2. Ice Scatter-Absorption

The magnitude and variability of transmission loss due to ice scatter-absorption were the most significant factors affecting the cumulative TL for the rays. This data set was from 1988, and the associated draft values are larger than would be representative for the Arctic Ocean today. As sea ice thins and the extent declines, it will be important to update acoustic propagation models and TL models in order to predict accurately how sound interacts with the surface/ice boundary. Along with this updating of models, it is important to verify them with empirical data. Thinner ice forms leads and ridges more easily, but the distribution of keel draft and spatial frequency can be expected to change from the thicker ice cover seen before the last 10 years. Continued efforts to monitor the extent, thickness and ice-keel draft of the Arctic sea ice, and to adapt predictive models to the changing environment are recommended.

3. Investigate Submarine Detection Ranges

To investigate the effects of the variability in T, S, pH, and ice roughness on submarine detection ranges, the model could be set up for given source noise levels, source and receiver depths, environmental noise, and receiver characteristics. Instead of calculating how much TL accumulates over a given range, and the factors that influence the different contributors, the model could determine the range limit at which a given ray would no longer be detectable. To increase the accuracy and applicability of this modeling effort, a model should be implemented that allows an accurate determination of total TL instead of an estimation along individual ray paths. Then, for a given received sound pressure level, and a known source level, an estimate of range to the contact could be improved by including the pH structure.

4. Model Validation

At APLIS, immediately following the radial survey, a group from the Woods Hole Oceanographic Institute conducted acoustic transmission loss measurements, with a source located at APLIS, and receivers suspended in the water column at each of the radial locations (every 9.4km). Further study and collaboration would be effective to compare the actual TL measurements with the predicted levels from the model.

THIS PAGE INTENTIONALLY LEFT BLANK

BIBLIOGRAPHY

- Ainslie, M. A., and J. G. McColm. "A simplified formula for viscous and chemical absorption in sea water." *J. Acoust. Soc. Am.* 103 (1998): 1671–1672.
- Anderson, Leif. University of Gothenburg, Sweden. "Arctic Ocean Chemistry." Monterey, CA: Personal communication with Stephen Col, March 1, 2010.
- Bates, N. R., J. T. Mathis, and L. W. Cooper. 2009. "Ocean acidification and biologically induced seasonality of carbonate mineral saturation states in the western Arctic Ocean." *J. Geophys. Res.* 114, no. C11007.
- Bates, N. R., S. B. Moran, D. A. Hansell, and J. T. Mathis. 2006. "An increasing CO₂ sink in the Arctic Ocean due to sea ice loss." *Geophys. Res. Lett.* 33, L23609 (doi:10.1029/2006GL027028): 1–7.
- Bates, R. G. "pH Scales for Sea Water. 1975." Edited by E. D. Goldberg. *Report of the Dahlem Workshop on The Nature of Seawater*. Berlin: S. Bernhard, Dahlem Konferenzen, 313–338.
- Beluga Group. *Successfully Mastered Northeast-Passage is Followed by Planning Start for 2010*. September 18, 2009. <http://www.beluga-group.com/en/?cHash=0bcb49d704ba9e09f896620a444162ef#Press-Archive-Archive> (accessed March 22, 2010).
- Bindoff, N. L., J. Willebrand, V. Artale, A. Cazenave, J. Gregory, S. Gulev, K. Hanawa, C. Le Quere, S. Levitus, Y. Nojiri, C. K. Shum, L. D. Talley, and A. Unnikrishnan. "2007: Observations: Oceanic Climate Change and Sea Level." In: *Climate Change 2007: The Physical Science Basis. Contribution of Working Group I to the Fourth Assessment Report of the Intergovernmental Panel on Climate Change*. Ed. S. Solomon, D. Qin, M. Manning, Z. Chen, M. Marquis, K. B. Averyt, M. Tignor, and H. L. Miller. 2007: 398–406.
- Boyer, T. P., Stephens, C., J. I. Antonov, M. E. Conkright, R. A. Locarnini, T. D. O'Brien, and H. E. Garcia. 2002. "World Ocean Atlas 2001, Volume 2: Salinity." *NOAA Atlas NESDIS 49*. E. S. Levitus. CD-ROMs. Wash D.C.: U.S. Government Printing Office.
- Caldeira, K., and M. E. Wickett. 2003. "Anthropogenic carbon and ocean pH." *Nature* 365.
- Chen, Chen-Tung, and Frank J. Millero. 1977. "Sound speed of seawater at high pressures." *J. Acoust. Soc. Am.* 62 : 1129–1135.

- Curry, J. A., J. L. Schramm, and E. E. Ebert. 1995. "Sea Ice-Albedo Climate Feedback Mechanism." *Journal of Climate* (American Meteorological Society) 8: 240–247.
- Dahl, P. H., J. W. Choi, N. J. Williams, and H. C. Graber. 2008. "Field measurements and modeling of attenuation from near-surface bubbles for frequencies 1-20 kHz." *J. Acoust. Soc. Am.* 124: EL163-EL169.
- Del Grasso, V. A. 1974. "New equation for the speed of sound in natural waters (with comparisons to other equations)." *J. Acoust. Soc. Am.* 56: 1084–1091.
- Del Grasso, V. A., and C. W. Mader. 1972. "Speed of Sound in Sea-Water Samples." *J. Acoust. Soc. Am.* 52: 961–974.
- Denman, K. L., G. Brasseur, A. Chidthaisong, P. Ciais, P. M. Cox, R. E. Dickinson, D. Hauglustaine, C. Heinze, E. Holland, D. Jacob, U. Lohmann, S. Ramachandran, P. L. da Silva Dias, S. C. Wofsy and X. Zhang. 2007. "Couplings between Changes in the Climate System and Biogeochemistry." *In: Climate Change 2007: The Physical Science Basis. Contribution of Working Group I to the Fourth Assessment Report of the Intergovernmental Panel on Climate Change.* Ed. S. Solomon, D. Qin, M. Manning, Z. Chen, M. Marquis, K. B. Averyt, M. Tignor, and H. L. Miller: 511–539.
- Diachok, O. I. 1976. "Effects of sea ice ridges on sound propagation in the Arctic Ocean." *J. Acoust. Soc. Am.* 59: 1110–1120.
- Doney, S. C. et al. 2007. "Impact of anthropogenic atmospheric nitrogen and sulfur decomposition on ocean acidification and the inorganic carbon system." Edited by M. L. Bender. *Proceedings of the National Academy of Sciences of the United States of America.* 14580–14585.
- Fisher, F. H., and V. P. Simmons. 1977. "Sound absorption in sea water." *J. Acoust. Soc. Am.* 62: 558–564.
- Fofonoff, N. P., and R. C., Jr. Millard. 1983. "Algorithms for computation of fundamental properties of seawater." *Unesco technical papers in marine science* 44: 5–9.
- Forster, P., V. Ramaswamy, P. Artaxo, T. Berntsen, R. Betts, D. W. Fahey, J. Haywood, J. Lean, D. C. Lowe, G. Myhre, J. Nganga, R. Prinn, G. Raga, M. Schulz, and R. Van Dorland. 2007. "Changes in Atmospheric Constituents and in Radiative Forcing." *In: Climate Change 2007: The Physical Science Basis. Contribution of Working Group I to the Fourth Assessment Report of the Intergovernmental Panel on Climate Change.* Ed. S. Solomon, D. Qin, M. Manning, Z. Chen, M. Marquis, K. B. Averyt, M. Tignor, and H. L. Miller: 132–186.

- Francois, R. E., and G. R. Garrison. 1982a. "Sound absorption based on ocean measurements: Part I: Pure water and magnesium sulfate contributions." *J. Acoust. Soc. Am.* 72: 896–907.
- Francois, R. E., and G. R. Garrison. 1982b. "Sound absorption based on ocean measurements. Part II: Boric acid contribution and equation for total absorption." *J. Acoust. Soc. Am.* 72: 1879–1890.
- Fricke, J. Robert. 1993. "Acoustic scattering from elemental Arctic ice features: Numerical modeling results." *J. Acoust. Soc. Am.* 93: 1784–1796.
- Hanson, K. J. 1961. "The Albedo of Sea ice and Ice Islands in the Arctic Ocean Basin." *Arctic* 14, no. 3: 188–196.
- Hester, K. C., E. T. Peltzer, W. J. Kirkwood, and P. G. Brewer. 2008. "Unanticipated consequences of ocean acidification: A noisier ocean at lower pH." *Geophys. Res. Lett.* 35, no. L19601 (doi: 10.1029/2008GL034913 2008): 1–5.
- Hunkins, K., G. Mathieu, S. Teeter, and A. Gill. 1970. "The Floor of the Arctic Ocean in Photographs." *Arctic*, no. 23: 175–189.
- Jakobsson, M., R. Macnab, L. Mayer, R. Anderson, M. Edwards, J. Hatzky, H. W. Schenke, and P. Johnson. 2008. "An improved bathymetric portrayal of the Arctic Ocean: Implications for ocean modeling and geological, geophysical and oceanographic analyses." *Geophys. Res. Lett.*, 10.1029/2008gl033520 2008.
- Kinsler, L. E., A. R. Frey, A. B. Coppens, and J. V. Sanders. 2000. *Fundamentals of Acoustics*. 4th Edition. Hoboken: John Wiley & Sons.
- Kraska, James, CDR, JAGC. 2008. "International Law in the Arctic." Brief to Joint Chiefs of Staff, May 1, 2008.
- Krynén, D. "COMNAVMETOCCOM INDEPENDENT MODEL REVIEW PANEL (CIMREP) FOR SHEN-MILLERO-LI SOUND SPEED ALGORITHM UPDATE, VERSION 1.1." Memorandum, Ocean Prediction Department, Naval Oceanographic Office, January 11, 2010.
- Lemke, P., J. Ren, R. B. Alley, I. Allison, J. Carrasco, G. Flato, Y. Fujii, G. Kaser, P. Mote, R. H. Thomas and T. Zhang. 2007: "Observations: Changes in Snow, Ice and Frozen Ground." *Climate Change 2007: The Physical Science Basis. Contribution of Working Group I to the Fourth Assessment Report of the Intergovernmental Panel on Climate Change*. Ed. S. Solomon, D. Qin, M. Manning, Z. Chen, M. Marquis, K. B. Averyt, M. Tignor, and H. L. Miller.
- Leroy, C. C., S. P. Robinson, and M. J. Goldsmith. 2008. "A new equation for the accurate calculation of sound speed in all oceans." *J. Acoust. Soc. Am.* 124, no. 5: 2774–2782.

- Lurton, Xavier. 2002. *An introduction to underwater acoustics: principles and applications*. Chichester, UK: Praxis Publishing Ltd.
- Mackenzie, K. V. 1960. "Formulas for the Computation of Sound Speed in Sea Water." *J. Acoust. Soc. Am.*: 100–104.
- McGeehan, T. 2008. *Investigation of 2-dimensional isotropy of under-ice roughness in the Beaufort Gyre and implications for mixed layer ocean turbulence*. Master's Thesis, Monterey: Naval Postgraduate School, 40.
- McPhee, M. G., and T. P. Stanton. 1996. "Turbulence in the statically unstable oceanic boundary layer under Arctic leads." *J. Geophys. Res.* 101: 6409–6428.
- Mellen, R. H., V. P. Simmons, and D. G. Browning. 1979. "Sound absorption in sea water: A third chemical relaxation." *J. Acoust. Soc. Am.* 65: 923–925.
- Millero, Frank J., and Xu Li. "Comments on "On equations for the speed of sound in seawater" [*J. Acoust. Soc. Am.* 93,255-275 (1993)]." *J. Acoust. Soc. Am.* 95, no. 5 (1994): 2757–2759.
- Moskal, Walt. 2010. "OAML News: OAML Approves Updated Underwater Sound Speed Equation." Electronic mail correspondence to Daphne Kapolka, February 4.
- National Oceanographic Data Center. 2007. *Data Sets & Products: World Ocean Atlas 2001*. September 12, 2007.
- National Snow and Ice Data Center. 2010. *Arctic Sea Ice News & Analysis*. February 24, 2010. <http://nsidc.org/arcticseaicenews/> (accessed February 25, 2010).
- . *State of the Cryosphere*. February 18, 2010. http://nsidc.org/sotc/sea_ice.html (accessed February 22, 2010).
- National Snow and Ice Data Center. *Submarine upward looking sonar ice draft profile data and statistics*. Digital Media. National Snow and Ice Data Center/World Data Center for Glaciology. Boulder, CO, 1998, updated 2006.
- Naval Oceanographic Office. "Software Design Description and Software Test Description for the Sound Speed Algorithm and Temperature Inversion Algorithm (U)." Systems Integration Division, Stennis Space Center, 2009, 18.
- Notz, Dirk, M. G. McPhee, M. G. Worster, G. A. Maykut, K. H. Schlunzen, and H. Eicken. "Impact of underwater-ice evolution on Arctic summer ice." *J. Geophys. Res.* 108, no. C7 (doi:10.1029/2001JC001173 2003): 3223.
- Roth, M. K. 2003. *Effects of Thermobaricity on Coupled Ice-Mixed Layer Thermodynamics*. Master's Thesis, Monterey: Naval Postgraduate School.

- Rothrock, D. A., Y. Yu, and G. A. Maykut. 1999. "Thinning of Arctic Sea ice Cover." *Geophys. Res. Lett.*: 3469–3472.
- Sabine, C. L., R. A. Feely, N. Gruber, R. M. Key, K. Lee, J. L. Bullister, R. Wanninkhof, C. S. Wong, D. W. R. Wallace, B. Tilbrook, F. J. Millero, T.-H. Peng, A. Kozyr, T. Ono, and Aida Rios. 2004. "The Oceanic Sink for Anthropogenic CO₂." *Science*, July 16, 2004: 367–371.
- Sea-Bird Electronics. "Application Note No. 18-2. SBE 18,22,27, and 30 pH sensor storage, maintenance, and calibration." *Sea-Bird Electronics, Inc.* Revised February 2010. http://www.seabird.com/application_notes/AN18_2.htm (accessed March 06, 2010).
- . "Application Note No. 2D. Instructions for Care and Cleaning of Conductivity Cells." *Sea-Bird Electronics, Inc.* Revised September 2008. http://seabird.com/application_notes/AN02d.htm (accessed 03 06, 2010).
- . "Frequently Asked Questions: General Oceanographic Questions." *Sea-Bird Electronics*. March 10, 2010. <http://www.seabird.com/FAQs/FAQsGeneralOceanographic.htm#PsuPpt> (accessed March 27, 2010).
- . "SBE 5M Mini Submersible Pump.2008. " Bellvue, WA.
- . "SBE Data Processing. 2008. " Sea-Bird Electronics, Inc.
- Semiletov, I., A. Makshtas, and S. -I. Akasofu. 2004. "Atmospheric CO₂ balance: The role of Arctic sea ice." *Geophys. Res. Lett.* 31, no. L05121.
- Siedler, G., and H. Peters. 1986. 3.1.2. *Salinity*. Vols. 3, *Oceanography*, chap. 3.1 in *Landolt Borstein: Numerical Data and Functional Relationships in Science and Technology*, edited by K. -H. Hellwege and O. Madelung, 235. Berlin, Germany: Springer-Verlag.
- Stanton, T. *Ocean Turbulence Laboratory*. February 2003. <http://www.oc.nps.edu/~stanton> (accessed March 2009).
- Stephens, C., J. I. Antonov, T. P. Boyer, M. E. Conkright, R. A. Locarnini, T. D. O'Brien, and H. E. Garcia. "2002. World Ocean Atlas 2001, Volume 1: Temperature." *NOAA Atlas NESDIS 49*. Ed. S. Levitus. CD-ROMs. Wash. D.C.: U.S. Government Printing Office.
- Stotts, S. A., R. A. Koch, and N. R. Bedford. 1994. "Development of an Arctic ray model." *J. Acoust. Soc. Am.* 95: 1281–298.

- Stroeve, J., M. M. Holland, W. Meier, T. Scambos, and M. Serreze. 2007. "Arctic sea ice decline: Faster than forecast." *Geophys. Res. Lett.* 34, no. L09501 (doi: 10.1029/2007GL029703 2007): 1–5.
- Submarine Force Museum. *USS Nautilus (SSN 571)*. 2009.
<http://www.ussnautilus.org/nautilus/index.shtml> (accessed February 22, 2010).
- Task Force Climate Change. 2009. "U.S. Navy Arctic Roadmap." Oceanographer of the Navy, United States Navy.
- Urick, R. J. *Principles of Underwater Sound*. 1983. 3rd Edition. Los Altos, CA: Peninsula Publishing.
- U.S. Department of Justice. *Mid- and Low-Frequency Sonar*. October 27, 2009.
<http://www.justice.gov/enrd/Anniversary/2387.htm> (accessed March 19, 2010).
- Wilson, W. D. 1960. "Speed of Sound in Sea Water as a Function of Temperature, Pressure, and Salinity." *J. Acoust. Soc. Am.* 32: 641–644.
- Woods Hole Oceanographic Institute. 2009. *Ice-Tethered Profiler Program*. Woods Hole, Massachusetts.
- Zeebe, R. E., and D. A. Wolf-Gladrow. 2001. *CO₂ in Seawater: Equilibrium, Kinetics, Isotopes*. The Netherlands: Elsevier Science B.V.

INITIAL DISTRIBUTION LIST

1. Defense Technical Information Center
Ft. Belvoir, VA
2. Dudley Knox Library
Naval Postgraduate School
Monterey, CA
3. Tim Stanton
Naval Postgraduate School
Monterey, CA
4. Daphne Kapolka
Naval Postgraduate School
Monterey, CA
5. Jeff Gossett
Arctic Submarine Laboratory
San Diego, CA
6. CAPT Doug Marble, USN
Office of Naval Research
Washington, DC
7. LT Stephen Col, USN
Naval Postgraduate School
Monterey, CA